UNIVERSITY OF COPENHAGEN
FACULTY OF SCIENCE

VNIVERSITATIS HAFNIENSIS
FACVLTATIS NATVRALIS

Genesis of Giants

Massive Galaxy Evolution over the Past 10 Billion Years

Dissertation submitted for the degree of

Philosophiæ Doctor

to the PhD School of The Faculty of Science, University of Copenhagen

on August 23 2019, by

Mikkel Stockmann

Supervisor: *Prof. Sune Toft*

Committee:

Prof. Rachel Bezanson, University of Pittsburgh, USA

Prof. Thorsten Naab, Max Planck Institute for Astrophysics, Germany

Prof. Johan P. U. Fynbo, University of Copenhagen, Denmark

Genesis of Giants

Massive Galaxy Evolution over the Past 10 Billion Years

What we have done for ourselves alone dies with us;
what we have done for others and the world remains and is immortal
– Albert Pike

All of this is for you,
Anette Stockmann 1956-2014

Abstract

The astonishing display of stars on a clear night sky has, since before the emergence of civilization as we know it, sparked curiosity and guided the principles of our early human ancestors. The shining cartels of light belong to the Milky Way galaxy, one among trillion starry islands in the visible Universe which constitute the gravitational nodes of the cosmic assembly. During 13.8 billion years of cosmic evolution, the genesis of matter perturbations gives rise to conglomerates of stars, the giant elliptical galaxies, a homogeneous population of dynamically hot massive galaxies, devoid of star formation and made up of old stars. These galaxies follow tight scaling relations that persist out to high redshift establishing their formation in the early Universe. The advent of near-infrared (NIR) observations and large cosmological surveys have revolutionized modern astronomy by allowing studies of these galaxies in the epoch of their formation, more than 10 billion years ago. In this thesis, we investigate the connection between a sample of compact red and dead galaxies, the so-called quiescent galaxies, at redshift $z > 2$ and their assumed descendant: the giant elliptical galaxies. We employ the study of scaling relations as a tool to understand the formation and evolution of massive galaxies over cosmic history.

Combining 10 years of international effort, we present the largest (homogeneously) selected sample of massive quiescent galaxies at $z > 2$ from the COSMOS survey with NIR X-Shooter spectroscopy and *HST* NIR imaging. The spectra contain information of the galaxies' distances, stellar masses, ages, and velocity dispersions that, combined with their morphology and sizes from imaging, allow for a detailed examination of their stellar and dynamical properties. The wealth of observations allow for the documentation of their compact structures, high-velocity dispersions and quiescent non-star-forming nature. We show that minor mergers can account for the size evolution for massive quiescent galaxies over the span of 10 billion years. Furthermore, we find that the evolution of the Fundamental Plane scaling relations, into present-day massive elliptical galaxies, can be characterized by passive evolution of the stellar population together with significant size growth by minor mergers with quenched stellar populations.

Resumé på Dansk

Den storslåede samling af stjerner på en klar nattehimmel har siden før vores civilisations opståen skabt nysgerrighed og styret grundprincipperne for vores tidlige menneskelige forfædre. De skinnende karteller af lys tilhører galaksen Mælkevejen, en blandt billioner af stjerneøer i det synlige univers, som udgør tyngdepunktsnoderne i den kosmiske komposition. I løbet af 13,8 milliarder år med kosmisk udvikling giver tilstedeværelsen af tyngde-perturbationer anledning til konglomerater af stjerner, de gigantiske elliptiske galakser, en homogen population af dynamisk varme, massive galakser, blottet for stjernedannelse og bestående af gamle stjerner. Disse galakser følger strikse relationer, der fortsætter ud til høj rødforskydning og etablerer deres tilblivelse i det tidlige univers. Fremkomsten af nær-infrarøde (NIR) observationer og store kosmologiske surveys har revolutioneret moderne astronomi ved at tillade studier af disse galakser i epoken ved deres dannelse for mere end 10 milliarder år siden. I denne afhandling undersøger vi forbindelsen af en samling af kompakte røde og døde galakser, de såkaldte quiescent galakser, ved rødforskydning $z > 2$ til deres antagede efterkommer: de gigantiske elliptiske galakser. Vi anvender studiet af strikse relationer som værktøj til at forstå tilblivelsen og udviklingen af massive galakser gennem den kosmiske historie.

Ved at kombinere 10 års international indsats præsenterer vi den største (homogent) udvalgte samling af massive, quiescent galakser ud til $z > 2$ fra COSMOS-kortlæggelsen med NIR X-Shooter-spektroskopi og *HST* NIR-billeder. Spektrene indeholder information om galaksernes afstande, stjernemasser, aldrer og hastighedsdispersioner, der kombineret med deres morfologi og størrelser fra billederne muliggør en detaljeret undersøgelse af deres stellære og dynamiske egenskaber. De rige observationer fører til dokumentation af deres formodede kompakte strukturer, høje hastighedsdispersioner og quiescent, ikke-stjernedannende karakter. Vi viser, at små galaksekollisioner kan forklare størrelsesudviklingen for massive, døde galakser gennem 10 milliarder år. Endvidere finder vi, at udviklingen af Fundamental Plan-relationerne fra høj rødforskydning til nutidens massive elliptiske galakser kan karakteriseres ved en passiv udvikling af de stellære populationer sammen med en betydelig størrelsestilvækst igennem kollisioner med små galakser, der har døde stellære populationer.

Acknowledgements

I would like to extend my sincere and deepest gratitude to my girlfriend Nina Voit. Your continuous support, love and understanding have contributed significantly to my sanity and well-being in the completion of this thesis and the research within it. I would also like to thank my Danish and Swiss family for their continued support, especially my sister Amanda, my dad Flemming and my stepmother Anne.

I would like to thank my supervisor Sune Toft. The first years of your mentorship and guidance were filled with patience, curiosity and high expectations which taught me appreciation for long nights of hard work when approaching telescope proposal deadlines. You kept me on my toes, even 5 min before telescope deadlines when you would share your last comments. I would like to thank you for later providing me with the opportunity to observe the early Universe using the Subaru telescope on top of Mauna Kea in Hawai'i, along with the suggestion to try the Kua' Aina burger in the north-shore hippie town Haleiwa on Oahu. Thank you for introducing me to the team of international scientists, especially Anna, Stefano and Inger. My appreciation goes to Anna and Stefano for hosting me in Arcetri, Florence, and for their great contribution to the research included in this thesis. I extend special thanks to Inger for the pivotal role in my work on the Fundamental Plane, for hosting me in Hilo, and for continually sharing news about your goats. To Johannes Zabl for sacrificing time in teaching me the secrets of X-Shooter reductions, thank you.

I would like to extend a special thanks to everyone at DARK and DAWN where I, over the last 10 years from infant Bachelor student to an administrative prodigy, treaded my first physics' steps leading into this dissertation. To my favorite administration trinity: Julie, Corinne and Michelle - thanks for making me family. I sincerely enjoyed the company of my DARK and DAWN colleagues who inspired great research and a priceless plethora of chats by the coffee machine, not forgetting the mad Christmas parties and post-coffee foosball games. Thank you all.

I would like to thank Carlos for spilling his great wizardry skills, in imaging presentation and analysis on to my research. For lodging us into the traditional Japanese ryokan and staying out at a bar until 4 in the morning despite having to give a talk the next day, thank you Carlos for your great friendship. I would also like to sincerely thank Francesco for your friendship and role in my mental well-being in the last year of my Ph.D studies. You were a great support. Moreover, thanks for showing me the beauty of imperfections and for putting my foosball skills to the test over and over and over again. Thanks to Isabella for always bringing good energy, being a badminton shark, and for indulging in the world of quiescent galaxies.

I would like to thank my friends outside of astronomy for providing the finest excuse for socializing and leaving unfinished work for the next day. An important thanks to the team of dedicated proofreaders who made a difference in clarifying and improving the presentation of this work; Nina, Julius and Amanda.

Finally, I would like to thank the Assessment Committee Members Prof. Rachel Bezanson, Prof. Thorsten Naab and Prof. Johan P. U. Fynbo for showing interest in my work and clearing their schedule to censor the dissertation and oral defense.

Contents

1

Introduction

1.1 Modern cosmology and the cosmic web of galaxies

The first recorded extra-galactic object was sighted by the Persian astronomer Abd al-Rahman al-Sufi in the year 964 and is today known as the Andromeda galaxy (M31, Messier 1781). This object, initially referred to as the “nebulaes smear" (Hafez 2010), was thought to be a nearby nebula until its extra-galactic discovery (Hubble 1926). This measurement confirmed that the spiral and elliptical nebulae, cataloged by Messier (1781) and Herschel (1789), were islands of stars, so-called galaxies, like our own Milky Way. These galaxies were discovered to recede from us with velocities proportional to their distance leading to the discovery of the expanding Universe (Lemaître 1927; Hubble 1929). The expansion implied that the Universe was smaller, denser and hotter at earlier times which became the cornerstone of the Hot Big Bang model. The origin of the most abundant elements and building blocks of galaxies, Hydrogen and Helium, could be explained by thermonuclear reactions in this hot state of the early Universe (Alpher et al. 1948). However, it was first widely accepted as the concordance model when the discovery of its afterglow, the Cosmic Microwave Background (CMB), was observed (Penzias & Wilson 1965; Dicke et al. 1965).

In recent times, the expansion of the Universe has been observed to accelerate by the study of Type Ia stellar explosions (Riess et al. 1998; Perlmutter et al. 1999). Their increased distance measurements were best fit by a slower expansion in the past and an accelerated expansion at present. In the framework of General Relativity (Einstein 1916) and the Friedmann equations (Friedmann 1922), this discovery gave rise to the concordance model of cosmology: Λ Cold Dark Matter (ΛCDM). This model describes a flat Universe with energy densities primarily of dark origin; with 68.9 % dark energy, 31.1 % matter where $\sim$ 85 % is dark matter and $\sim$ 15 % is baryonic (luminous) matter (Planck Collaboration et al. 2018).

The Universe went through an exponentially expanding inflationary phase from which the primordial quantum fluctuations were enhanced to cosmological scales (Guth 1981; Linde 1982; Albrecht & Steinhardt 1982). (Hawking 1982; Guth & Pi 1982; Starobinsky 1982). The initial density fluctuations collapsed as a result of gravitational instabilities (Jeans 1902) that grew over time into the cosmic web. Large low-density voids are surrounded by gravitational nodes and filaments in which groups and clusters of galaxies reside (Gamow & Teller 1939; Lifshitz 1946). An important

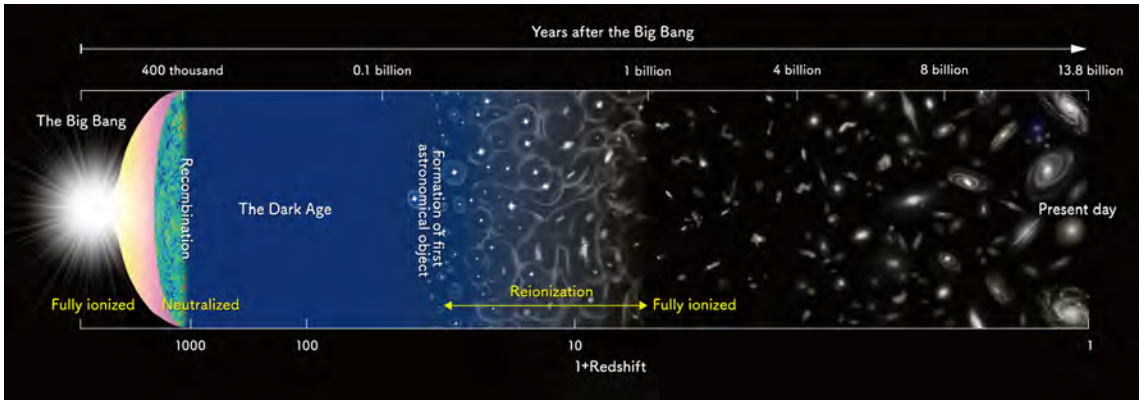

Figure 1.1: Schematic of the proposed evolution of the Universe from the Big Bang to the observed population of nearby galaxies. Credit: NAOJ

ingredient in the formation of structures is dark matter, which was first discovered by weighing nearby galaxy clusters (Zwicky 1933). Its invisible nature and collision-less characteristics were critical to accelerating the growth of over-densities in the early Universe. After the photon-matter decoupling, 380,000 years after the Big Bang following the cooling and expansion of the Universe, the baryons condensed into the already collapsed dark matter haloes. In these, the first stars that gave rise to the first galaxies were formed (White & Rees 1978). The collapse of collision-less structures like cold dark matter can be predicted from perturbation theory (Lifshitz 1946). However, the complex baryonic processes related to the formation and evolution of galaxies is, to this day, not fully understood.

1.2 The local galaxy zoo

The diverse morphology of galaxies has been known long before their extra-galactic discovery (Herschel 1789; Rosse 1844). The Hubble sequence classification scheme divided optically bright nearby galaxies into two broad categories: elliptical and spiral galaxies. Elliptical galaxies are red, dominated by the random motion of stars and have spheroidal shapes, in contrast to the disk-like rotation dominated structure of blue spiral galaxies (see Figure 1.2). The elliptical and spiral galaxies are commonly referred to as early-type and late-type, respectively, based on a misconception that spiral galaxies were mature states of elliptical galaxies (Hubble 1926). However, from the results of the early numerical simulations, elliptical galaxies were instead suggested to be merger remnants of the collision between galaxies (Toomre & Toomre 1972).

Up until the 21st century and at the start of the Sloan Digital Sky Survey (SDSS, York et al. 2000), most knowledge on galaxies was based on small studies. SDSS has today observed more than 800,000 galaxies in the nearby Universe with optical photometry and high-resolution spectra. Fundamental galaxy properties (e.g. stellar mass and age) can be obtained from the modeling of the spectral energy distribution (SED, see Figure 1.6). The pattern of the cosmic web was revealed

Figure 1.2: Stellar streams and shells of the massive elliptical galaxy NGC 474 (left), that spans ∼250,000 light years and lies about 100 million light years distant toward the constellation of the Fish (Pisces). At similar distance the spiral galaxy NGC 470 (right). Credit: CFHT, Coelum, MegaCam, J.-C. Cuillandre (CFHT) & G. A. Anselmi (Coelum)

by the precise determination of redshift, which, in comparison to simulations (Springel et al. 2005), established a scenario of bottom-up formation of structures. This wealth of information allows for statistical studies like the bimodality of the Hubble sequence (see Figure 1.3). The distribution of late-type and early-type galaxies are popularly known as the blue cloud and the red sequence referring to star-forming galaxies (SFGs) and quiescent galaxies (QGs), respectively. The photometric $u - r$ color difference, sampling the optical part of the SED, is considered an age indicator (tracing the 4000 Å break), shows that the elliptical (early-type) galaxies are the oldest, most massive and star-formation quenched galaxies. Moreover, they are found to dominate the central regions of massive galaxy clusters suggesting that they represent a mature state of galaxy evolution (Dressler 1980; Tanaka et al. 2005). The morphology of the massive elliptical galaxy, NCG 474, shows both a compact central core and a diffuse outskirt supporting a rich merger history (see Figure 1.2).

These massive quiescent elliptical galaxies are an exceptionally homogeneous population that form scaling relations like the Fundamental Plane (FP, Faber & Jackson 1976; Djorgovski & Davis 1987; Dressler et al. 1987; Bernardi et al. 2003) and the stellar mass-size relation (Shen et al.

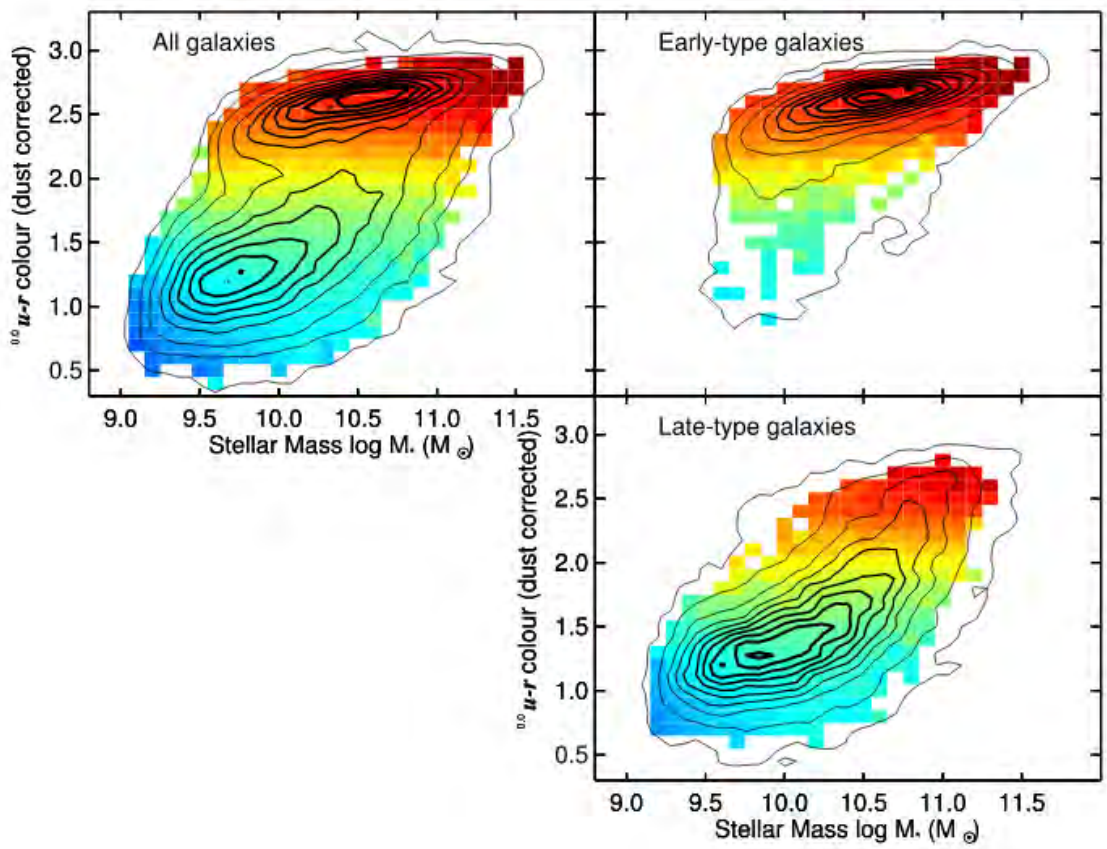

Figure 1.3: The bimodal distribution of nearby galaxies shown in rest-frame $u - r$ and stellar mass with colors representing the mean specific star formation rate (star formation rate per stellar mass). The red sequence of early-type galaxies is, on average, more quiescent, more massive and older than the late-type galaxies. Credit: Schawinski et al. (2014)

2003). Along with archaeological studies of their stellar populations, these relations reveal that the galaxies formed the majority of their stars in the early Universe. Studying the galaxies in their epoch of formation might shed light on the origin of these tight scaling relations and the physical mechanisms driving the bimodality of present-day galaxies.

1.3 The high redshift universe

The finite speed of light in an expanding Universe provides the opportunity for us to tie the distance of galaxies (redshift) together with the time at which they emitted their light. Observations at different redshifts present snapshots of the galaxies at different stages of their life. Pieced together, they can teach us about their formation and evolution until present-day. High-redshift observations are challenging as the optical light is shifted towards the NIR where the atmosphere becomes increasingly more opaque and the detectors are affected by thermal noise. However, over the last decades, the observations have been revolutionized by the advent of large telescopes (Very Large Telescope, W. M. Keck Observatory, Subaru Telescope), advanced ground-based

NIR instruments (X-Shooter, MOSFIRE) and space-based observatories (Hubble Space Telescope, Spitzer Space Telescope, Herschel Space Observatory).

The large cosmological fields, like the Cosmic Evolution Survey (COSMOS, Scoville et al. 2007), use multi-wavelength photometric coverage as an efficient and cheap method to image thousands of galaxies (Ilbert et al. 2009; Laigle et al. 2016). Stellar Population Synthesis (SPS) modeling of their photometric SEDs produces qualified redshift guesses and crude estimates of their galaxy properties. These statistical low-resolution assessments are used to select prime examples of, in the case of the present project, the rare massive QGs for detailed followed-up, as we will show in Chapter 2.

Galaxies at high redshift are fainter, harder to resolve and require time-expensive spectroscopic observations to obtain their accurate distances. Furthermore, they look intrinsically different, with clumpy and/or irregular morphology compared to the well defined local galaxy types. Yet, the combination of stellar population properties and morphology reveals the onset of the bi-modal distribution and the formation of the Hubble sequence more than 10 billion years ago at $1.5 < z < 2.5$ (see Figure 1.4).

The distribution of galaxies at high redshift have previously been distinguished by using spectroscopy to measure D_n4000 or the equivalent width of Hα (Kauffmann et al. 2003; Brinchmann et al. 2004). More recently, photometric color-color diagrams (*BzK*, *UVJ*, *NUVrK*) have been successful at characterizing SFGs and QGs, especially galaxies that are red by age from the ones that are red by dust (Daddi et al. 2005; Wuyts et al. 2007; Williams et al. 2009; Arnouts et al. 2013). When using UVJ classified SFGs and QGs, to study the stellar mass-size relation, it show that galaxies on average are smaller at high redshift compare to their local counterparts (see Figure 1.4, van der Wel et al. 2014). Observations of local SFGs present a strong relation between the star formation and stellar mass, referred to as the “galaxy main sequence" (see Figure 1.4, Brinchmann et al. 2004; Noeske et al. 2007; Elbaz et al. 2007). A common interpretation of its existence and tight relation is that the majority of SFGs evolve via self-similar processes and only a fraction of galaxies are above the relation in a starburst phase (Rodighiero et al. 2011). QGs are, with their low star-formation rates, found orders of magnitudes below the relation at similar stellar mass (see Figure 1.4, Wuyts et al. 2011; Whitaker et al. 2017). Furthermore, the galaxy main sequence evolves such that high redshift galaxies at a similar mass are more star-forming (Whitaker et al. 2012; Speagle et al. 2014; Schreiber et al. 2015; Barro et al. 2017). At $z \sim 2$, the star formation rate density (Madau & Dickinson 2014), the total quasar luminosity density (Hopkins et al. 2007) and the merger rate (Man et al. 2012) are observed to peak. Despite this fiery state of galaxy formation, half of the most massive galaxies were already devoid of star-formation at this epoch (Brammer et al. 2011, see Figure 1.7) suggesting that they formed at even earlier times.

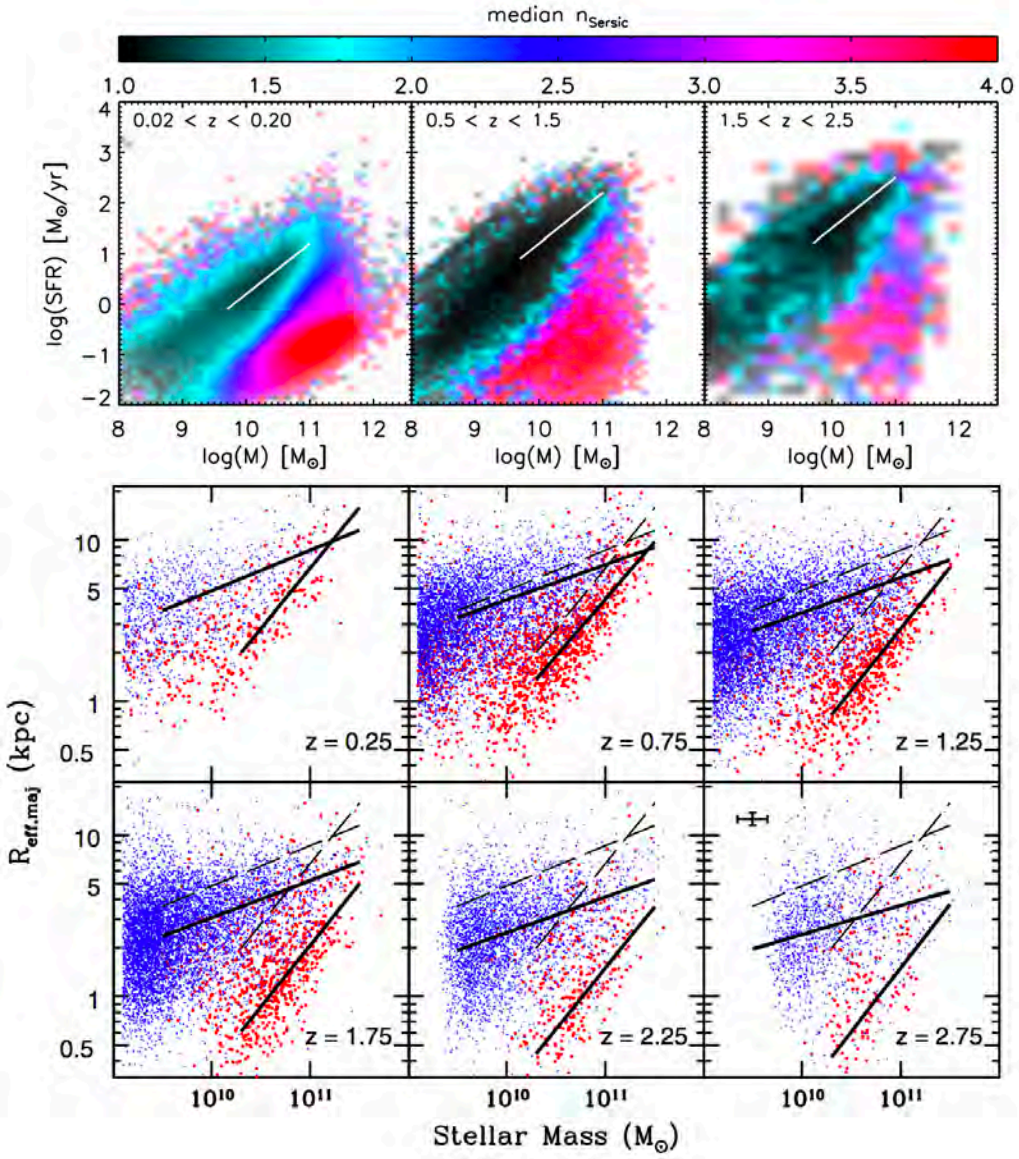

Figure 1.4: Top: The star formation rate with stellar mass for three redshift epochs (left to right). The figure is color-coded by Sérsic Index from black disk ($n = 1$) to red spheroidal ($n = 4$) galaxy. The average rise in star-formation with redshift is for disk galaxies indicated by the white line. Bottom: The stellar mass size relation for UVJ QGs and SFGs across from $z = 0.25 - 2.25$. The dashed line indicates the size of galaxies at $z = 0.25$. Credit: Wuyts et al. (2011) (top), van der Wel et al. (2014) (bottom).

1.4 Massive galaxies in the early universe

A population of red galaxies at $z \sim 2$ was discovered in the Hubble Deep Field – South (Franx et al. 2003; Daddi et al. 2004; Toft et al. 2005). The galaxies were selected from the Faint InfraRed Extragalactic Survey (FIRES; Franx et al. 2000) to mimic the optical colors and the 4000 Å Balmer break of nearby elliptical galaxies. The Hubble Deep Fields had, at this time, only been observing with optical filters which explains why these galaxies with optical faint colors and lack of emission

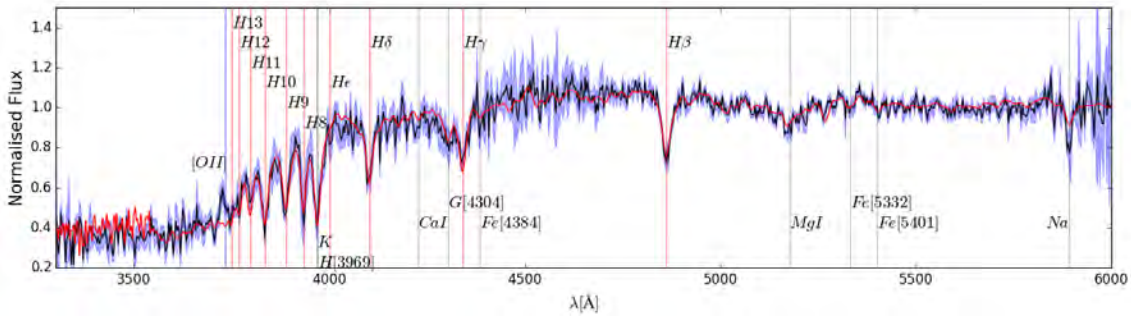

Figure 1.5: The rest-frame optical composite spectrum of 15 massive QGs (black line, presented in Chapter 2) together with the best fit stellar population model (red). The 1σ uncertainty are shown in blue shading. The spectrum reveals deep Balmer absorption lines to high excitation (vertical red lines), for evolved stellar populations with ages of $1-3$ Gyrs. The analysis of this spectrum, the metal lines (vertical gray) and [OII] emission (vertical blue) will be addressed in Stockmann et al. in prep.

lines had not previously been discovered. The lack of young blue stellar light together with their strong Balmer breaks indicated evolved stellar populations with ~ 1 Gyr old ages confirming their quiescent nature (Cimatti et al. 2004; Daddi et al. 2005; Labbé et al. 2005; Kriek et al. 2006a; Toft et al. 2007; Williams et al. 2009).

With the addition of a NIR imaging instrument on *HST* the red and dead galaxies, that before had been unresolved in ground-based images, were discovered to be remarkably compact (Toft et al. 2005; Daddi et al. 2005; Papovich et al. 2005; Trujillo et al. 2006, 2007; Toft et al. 2007; Zirm et al. 2007; Buitrago et al. 2008). Their compact sizes resulted in extremely high stellar densities (van Dokkum et al. 2008), unlike local elliptical galaxies. More accurate size measurement, following the improved resolution of *HST*/WFC3, led to the conclusion that compact quiescent galaxies (cQGs) were common among massive galaxies at high redshift (Szomoru et al. 2012; Newman et al. 2012; van der Wel et al. 2014). In the nearby Universe, only a few examples of such compact massive galaxies had been found with ages (2-4 Gyr) indicating formation much later than the observed cQGs at $z > 2$ (Trujillo et al. 2009; Taylor et al. 2010a; Shih & Stockton 2011). The majority of cQGs must, as a result, undergo rapid size growth by a factor of ~ 4 and is incompatible with passive evolution to the local Universe (Kriek et al. 2008; Toft et al. 2009).

High-resolution spectroscopy of $z > 2$ massive QGs confirmed their quiescent nature with little or no star formation (traced by optical and mid-infrared emission lines), evolved stellar populations with 1-3 Gyr old ages and high stellar masses, $\log_{10}(\mathrm{M}/\mathrm{M}_{\odot}) > 11$ (Kriek et al. 2009b; Toft et al. 2012; van de Sande et al. 2013; Belli et al. 2014b; Kriek et al. 2016; Belli et al. 2017; Kado-Fong et al. 2017; Morishita et al. 2019; Marsan et al. 2019). The spectra of massive QGs at $z > 2$ exhibit deep Balmer absorption lines and faint ultra-violet light (see Figure 1.5). Pristine S/N spectra of massive QGs at $z \sim 2$ display high velocity dispersion measurements (from absorption line broadening) of $\sigma = 250 - 500$ km/s (van Dokkum et al. 2009; Toft et al. 2012; Bezanson et al. 2013; van de Sande et al. 2013; Belli et al. 2014b; Kriek et al. 2016; Belli et al. 2017). Spectroscopic

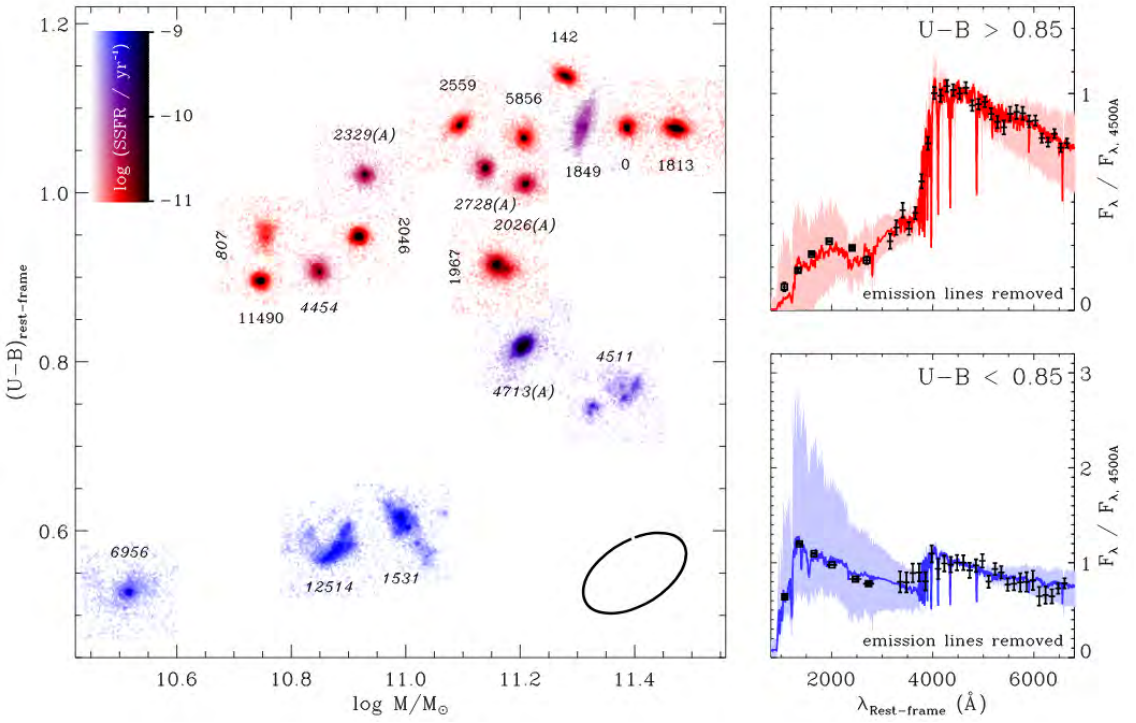

Figure 1.6: The rest-frame $U-B$ colors with stellar mass for QGs and SFGs at $z \sim 2.3$ (as traces by star formation rate per unit mass, left). The red/blue spectrum represents the typical QG/SFG at $z > 2$ (top/bottom right). The red sequence at $z > 2$ (left, see Figure 1.3) is shown by the compact structure of the QGs in the red image cutouts. Credit: Kriek et al. (2009a)

confirmation of young (~ 0.5 Gyr) massive QGs (Glazebrook et al. 2017; Schreiber et al. 2018) out to $z = 3.7$ with continually smaller sizes < 0.5 kpc (Straatman et al. 2015; Kubo et al. 2018) have, despite the initial skepticism on their quiescent nature (Simpson et al. 2017; Schreiber et al. 2018), been confirmed. Valentino and Stockmann et al. (in prep.), have, with deep MOSFIRE observations, discovered a massive QG at the exceptional distance of $z > 4$ which is only 1.5 Gyr after the Big Bang.

The velocity dispersion and size measurements are important to study the dynamics and scaling relations like the FP that reveal clues to the puzzle of how the homogeneous population of nearby elliptical galaxies formed. The FP, tracing the interplay between the stellar and dynamical components, has been securely established out to $z < 2$ (van der Marel & van Dokkum 2007; Bezanson et al. 2013; Jørgensen & Chiboucas 2013; van der Wel et al. 2014; Bezanson et al. 2015; Beifiori et al. 2017), however, its existence at higher redshift would imply formation at even earlier times. In Figure 1.7, the FP evolution is shown for a sample of four galaxy clusters out to redshift $z \sim 1$. In Chapter 3, a sample of massive QGs at $z > 2$ (presented in Chapter 2) is studied in the FP and mass-to-light ratio scaling relations. Contrary to lower redshift studies (e.g. Jørgensen & Chiboucas 2013), the structural evolution is found to be playing an important role in shaping the tight scaling relations galaxies in the nearby Universe (see Chapter 3). The

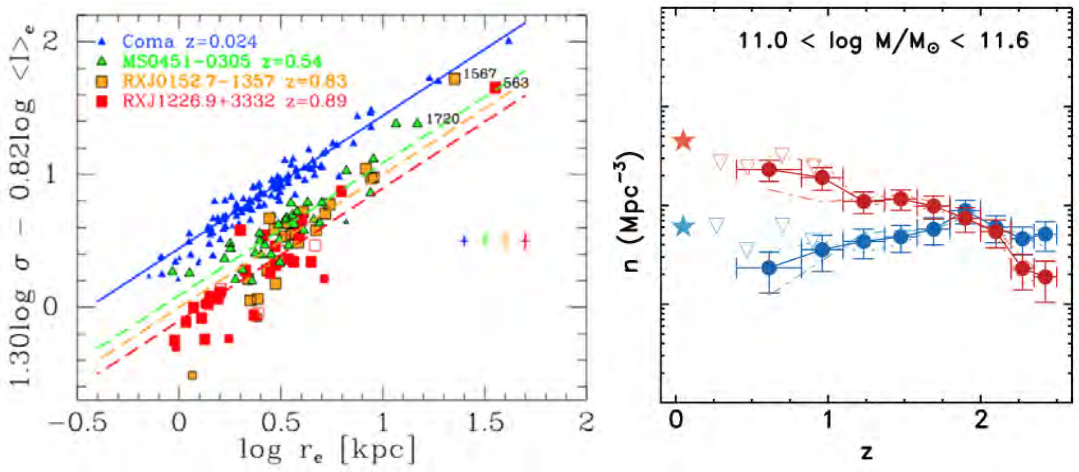

Figure 1.7: Left: The Fundamental Plane projection of the best-fit Coma galaxy cluster relations (blue) alongside three galaxy clusters at $z = 0.54, 0.83, 0.89$ (see legend). The figure shows the redshift evolution of the FP scaling relation with redshift. Right: The evolution of the number density for massive, $11 < \log_{10}(\mathrm{M}/\mathrm{M}_{\odot}) < 11.6$, UVJ classified QGs and SFGs. Only 3 Gyrs after the Big Bang at $z = 2$ half of the most massive galaxies have already ceased their star formation to become red and dead. Credit: Jørgensen & Chiboucas (2013) (left), Brammer et al. (2011) (right).

morphology of QGs is shown to be more disk-like at high redshift (van der Wel et al. 2011; Chang et al. 2013; Bezanson et al. 2018), suggesting that their kinematic structure could deviate from the simple dispersion dominated nearby elliptical galaxies. This directly affects the assessment of their dynamics and the scaling relations (see e.g. Belli et al. 2017). Spatially resolved spectroscopy, needed to address this issue, is inaccessible from ground-based facilities due to the galaxies compact sizes and faint magnitudes. Massive foreground clusters work as lenses to the distant Universe and are used to study the internal dynamics of a spatially resolved gravitationally lensed QG (Newman et al. 2015). Recent studies have found a rapidly rotating massive QG at $z > 2$ with disk-like morphology (Toft et al. 2017; Newman et al. 2018). This discovery could suggest that quenching of the stellar population occurs before the morphological transformation, from a rotation dominated disk into a dispersion dominated spheroidal. The discovery of rare lensed QGs requires well-observed foreground lensing clusters. Two lensed QGs were, with high S/N X-Shooter observations (Principal Investigator: Stockmann), found to be at $z = 1.6$ and $z = 3.2$ (see Figure 1.8).

1.5 The evolution of massive galaxies

Number density studies show that the fraction of UVJ QGs is increasing compared to the SFGs (see Figure 1.7). A similar evolution exists for galaxies traced by morphology (Buitrago et al. 2013), suggesting that the colors of galaxy SEDs are still coupled to the morphology out to $z \sim 2.5$. The continuous transition of galaxies from disk to spheroidal morphology requires a potent gravitational mechanism, like mergers (Man et al. 2016a), to redistribute the stellar components.

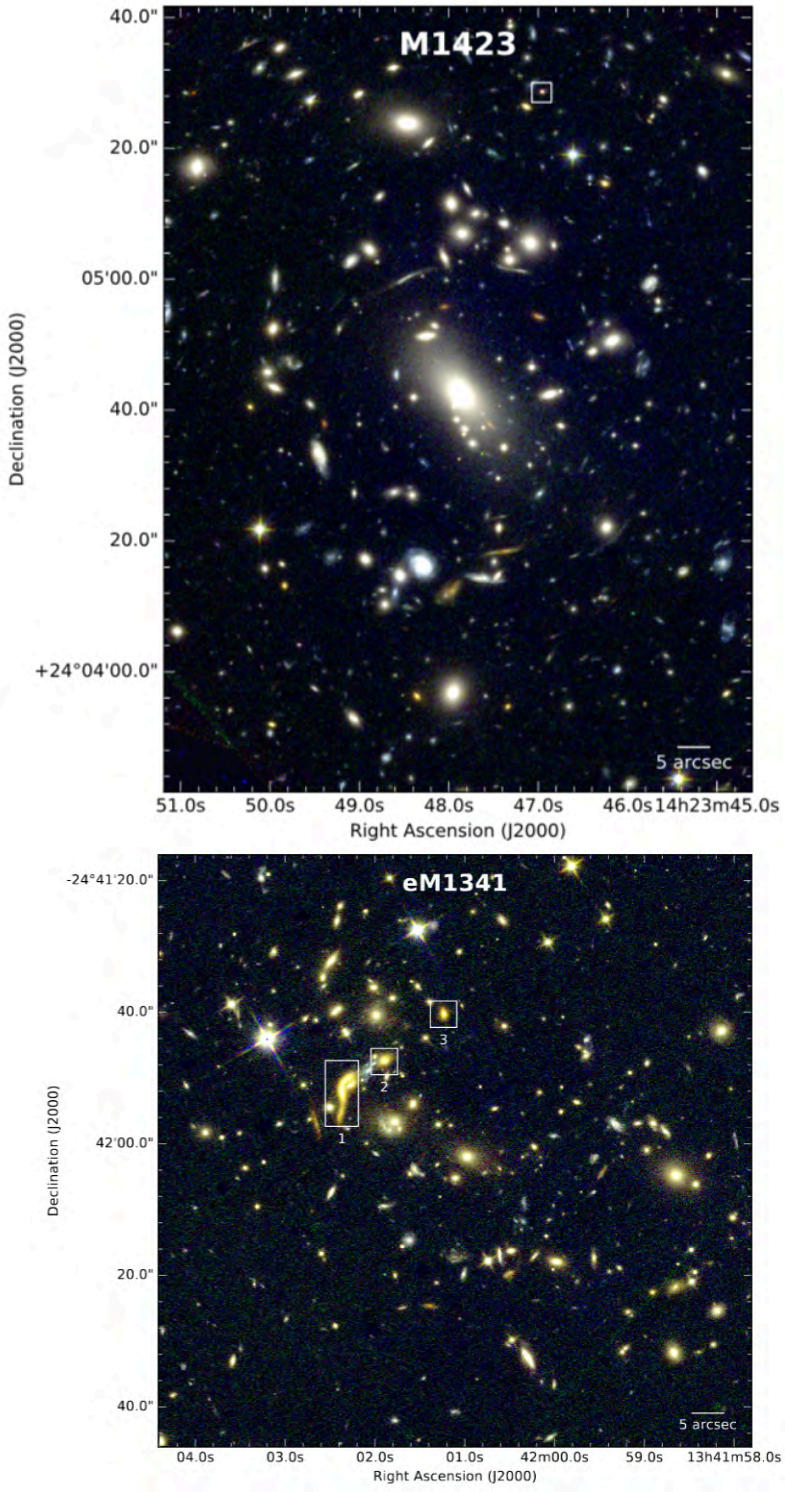

Figure 1.8: Top: MACS1423 galaxy cluster with the lensed massive QG MACS1423-1 at $z = 3.20$. Bottom: A thirty fold lensed QG (1) from the eMACS141 cluster at $z = 1.6$, with two confirmed counter images (2,3) (Ebeling et al. 2018). Credit: Man et al. 2019 in prep.

Numerical studies have shown that gas-poor minor mergers, with mass ratios of 1:5-20, are efficient at explaining the observed size growth in QGs (Khochfar & Silk 2006; Hopkins et al. 2009; Bezanson et al. 2009; Naab et al. 2009; Nipoti et al. 2009; Oser et al. 2012; Hilz et al. 2012, 2013). Evolution, primarily via major merger also increases the size, however, on the expense of making the elliptical galaxy remnants too massive compared to nearby elliptical galaxies. Simulated in-situ feedback processes from AGN have been shown to reproduce size growth of massive galaxies (Fan et al. 2008, 2010; Ragone-Figueroa & Granato 2011; Choi et al. 2018). The observed build-up of stellar mass in the outskirts of massive elliptical galaxies (Bezanson et al. 2009; Szomoru et al. 2012) are well described by the minor merger inside-out growth found in simulations (Hilz et al. 2013). This inside-out growth scenario could explain the stellar tidal streams and shells structures observed in nearby massive elliptical galaxies, like the one shown in Figure 1.2. Studies have shown that structural evolution cannot fully account for the observed size evolution size out to $z = 3$ (Newman et al. 2012; Man et al. 2012, 2016a, see Bluck et al. (2012) for another view). Part of this size evolution can be explained by the addition of larger QGs over time by effectively diluting the high-redshift population (Carollo et al. 2013; Krogager et al. 2014).

The mechanism responsible for the quenching of the star-formation in galaxies is a widely debated topic. In Man & Belli (2018), they define quenching as the interruption of the necessary conditions for star-formation. Amongst many of them, they include cosmological starvation of gas, gas heating by in-situ stellar or AGN feedback processes and morphological quenching preventing cold gas from forming stars. The discovery of low molecular gas fraction in a high redshift compact QG shows that a mechanism that either consumes or removes the cold gas could be responsible for the quenching of massive QGs (Bezanson et al. 2019). The suppression of star-formation, via the ejection or heating of cold gas by feedback from AGN, has recently gained interest. It is thus intriguing that AGN signatures, like excess x-ray and radio emission, have been observed in massive galaxies (Olsen et al. 2013; Man et al. 2016b). In Chapter 2, we find radio emission in some of our massive quiescent galaxies that could shed light on the connection between AGN and massive QGs at high redshift (Cortzen and Stockmann et al. in prep.).

A two-phase assembly of massive galaxies is emerging from numerical works (De Lucia & Blaizot 2007; Oser et al. 2010; Hirschmann et al. 2012; Oser et al. 2012; Gabor & Davé 2012; Naab 2013, e.g.) where their early formation is dominated by dissipative processes and in-situ star-formation, resulting in a quenched compact stellar component followed by late formation of ex-situ accretion of minor mergers (Oser et al. 2012; Gabor & Davé 2012). The progenitors of massive elliptical galaxies grew, in this picture according to simulations, very massive in a short period of time after their formation at $z \sim 6$ (Khochfar & Silk 2006; De Lucia et al. 2006; Naab et al. 2007, 2009; Dekel et al. 2009; Oser et al. 2010, 2012; Wellons et al. 2015). The compact nature of the $z = 2$ QGs suggests that they must have formed in concentrated starburst-like environment. A sample of submillimeter galaxies (SMGs) at $z > 3$ was suggested to be the

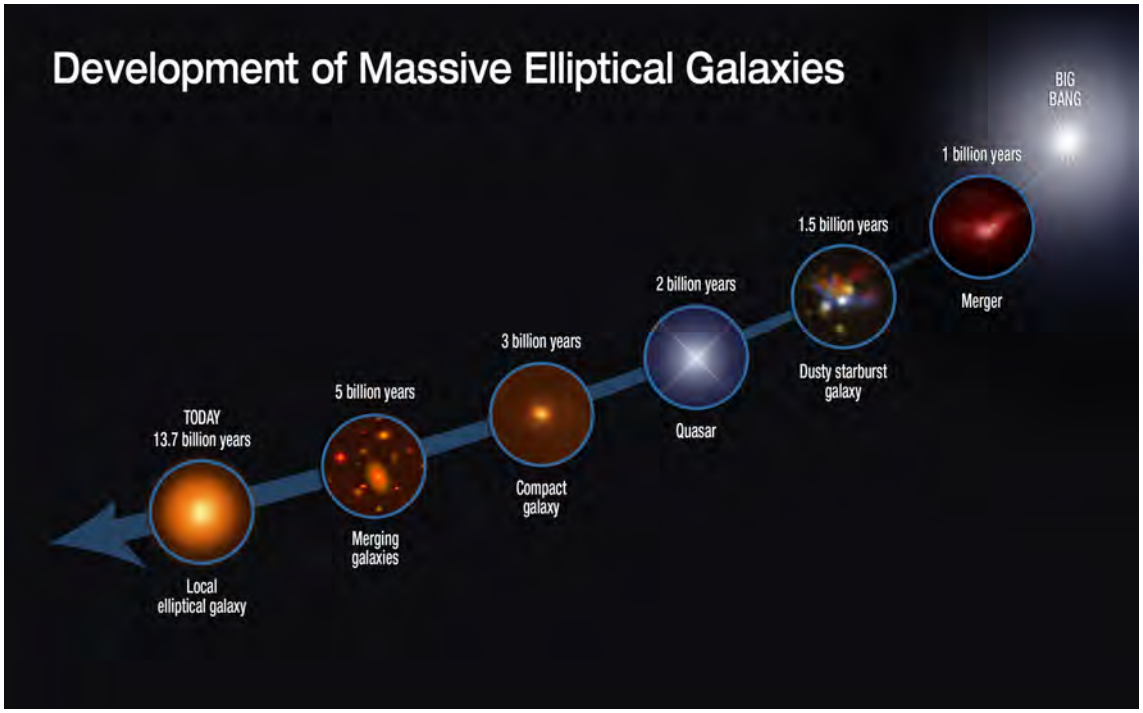

Figure 1.9: Schematic evolution of massive elliptical galaxies. Credit: NASA, European Space Agency, S. Toft and A. Feild

progenitors of $z = 2$ cQGs based on matching of their number density, formation redshift and galaxy properties (Ricciardelli et al. 2010; Toft et al. 2014). SMGs were, due to their extreme dust temperatures, believed to be dust-obscured starbursts. As suggested in Toft et al. (2014), a multi-wavelength study of $z \sim 4$ SMGs finds that their compact structure and minor merger companions are consistent with the connection to cQGs at $z = 2$ (Gómez-Guijarro et al. 2018). A sample of compact SFGs found at $z < 3$ (Barro et al. 2013, 2017) was suggested to be good candidates for transition-objects between the $z > 3$ SMGs and the $z = 2$ massive cQGs, matching both their stellar and structural properties.

1.5.1 Connecting the extremes

A conceptually simple picture of massive galaxy evolution from $z = 6$ to present-day is advocated in Toft et al. (2014) (see Figure 1.9). Here, bright $3 < z < 6$ SMGs form in gas-rich mergers that drive nuclear dusty starbursts in the central regions. The dust is heated by the intense star formation generating bright SMGs. Shortly thereafter (~ 50 Myrs), the star formation ceases either by gas depletion or due to the heating of their cold gas reservoirs, preventing star formation via feedback from a Super Massive Black Hole (SMBH). The latter can be observed as quasars, which become plentiful at $z < 4$. These compact and star-formation quenched galaxies passively evolve to $z = 2$, where they are observed with ages of ~ 1 Gyrs. They gradually grow in size and mass over the next 10 billion years to become the most massive elliptical galaxies in the nearby

Universe. This evolution scenario might be too simplistic (see e.g. Naab et al. 2014) but serves as a model that can be statistically validated with the launch of the next-generation space telescopes.

1.6 Scientific objectives and thesis structure

The main focus of this thesis is the extreme lives of massive galaxies and their rich evolution from the time of their anticipated progenitors, the massive cQGs, and until present-day giant elliptical galaxies. Specifically, the evolution of the structural and dynamical properties over the last 10 billion years is addressed. This work is completed using X-Shooter spectroscopy and *HST* NIR imaging to derive galaxy properties similar to nearby galaxies allowing for a direct comparison. The thesis addresses the following questions related to the phenomenological scenario of the formation of massive elliptical galaxies (see Figure 1.9): How much star-formation exist in the cQGs at $z = 2$ close to their formation epoch? When did the massive cQGs at $z = 2$ form? What is the physical mechanism responsible for shaping the tight scaling relations of nearby massive elliptical galaxies? What is the relative contribution of the different mechanisms responsible for the observed size growth? In Chapter 2, the largest spectroscopically confirmed sample of 15 massive QGs at $z > 2$ with high stellar masses, $\log_{10}(\mathrm{M}/\mathrm{M}_{\odot}) > 11$, high velocity dispersions, $\sigma = 250 - 350$ km/s, and semi-major axis sizes, $1.5 - 5.5$ kpc, is presented. These galaxies are confirmed to be quiescent, just 1.5 Gyr after their formation, with optical and mid-IR star formation rates, orders of magnitudes lower than SFGs of similar mass. Their small sizes and large masses verify their compact nature in the mass-size relation at similar redshift. If the considered sample of cQGs is the progenitors (as per a fixed number density) of massive elliptical galaxies, they must quadruple their sizes and double their stellar mass from $z = 2$ to present-day. The dynamical mass evolves faster than the stellar mass within the effective radius, suggesting that dark matter haloes, in these galaxies, play an important role in their evolution.

In Chapter 3, the existence of the Fundamental Plane and the mass-to-light ratio scaling relations for 10 massive QGs at $z = 2$ are explored. A FP is established at $1.5 < z < 2.5$ by combining COSMOS galaxies from Belli et al. (2017) and Stockmann et al. (2019). The FP zero-point suggests strong dynamical M/L evolution from $z = 2$ to present-day. The formation redshift, based on the stellar population modeled ages, suggests a formation at $z > 3.5$. The evolution of the scaling relation to present-day massive elliptical galaxies can not be explained by passive evolution of the stellar population without the advent of structural growth via dry minor mergers.

In Chapter 4, this thesis is concluded by summarizing the results and discussing future research.

2

A Sample of Ultra Massive Quiescent Galaxies at High-Redshift

This chapter contains the following article:

"X-Shooter Spectroscopy and *HST* Imaging of 15 Ultra Massive Quiescent Galaxies at $z \gtrsim 2$"

Submitted to *The Astrophysical Journal*, 30 July 2019

M. Stockmann, S. Toft, A. Gallazzi, S. Zibetti, C. J. Conselice, B. Margalef-Bentabol, J. Zabl, I. Jørgensen, G. E. Magdis, C. Gomez-Guijarro, F. M. Valentino, G. B. Brammer, D. Ceverino, I. Cortzen, I. Davidzon, R. Demarco, A. Faisst, M. Hirschmann, J.-K. Krogager, C. D. Lagos, A. W. S. Man, C. J. Mundy, Y. Peng, J. Selsing, C. L. Steinhardt, & K. E. Whitaker

We present a detailed analysis of a large sample of spectroscopically confirmed ultra-massive quiescent galaxies ($\log(M_*/M_\odot) \sim 11.5$) at $z \gtrsim 2$. This sample comprises 15 galaxies homogeneously selected in the COSMOS and UDS fields by their bright K-band magnitudes and followed up with VLT/X-Shooter spectroscopy and *HST*/WFC3 H_{F160W} imaging. These observations allow us to unambiguously confirm their redshifts ascertain their quiescent nature and stellar ages, and to reliably assess their internal kinematics and effective radii. We find that these galaxies are compact, consistent with the high mass end of the mass-size relation for quiescent galaxies at $z = 2$. Moreover, the distribution of the measured stellar velocity dispersions of the sample is consistent with the most massive local early-type galaxies from the MASSIVE Survey showing that evolution in these galaxies, is dominated by changes in size. The *HST* images reveal, as surprisingly high, that $40\ \%$ of the sample have tidal features suggestive of mergers and companions in close proximity, including three galaxies experiencing ongoing major mergers. The absence of significant kinematic evolution from $z = 2$ to 0, coupled with a doubling of the stellar mass, with a factor of four size increase and the observed disturbed stellar morphologies support dry minor mergers as the primary drivers of the evolution of the massive quiescent galaxies over the last 10 billion years.

2.1 Introduction

Local galaxies follow a bimodal distribution in color represented by blue star-forming spirals and red dormant elliptical galaxies. The most massive galaxies, primarily located in cluster environments, are the giant Elliptical galaxies with stellar population ages suggesting a formation more than 10 billion years ago (Ma et al. 2014; Greene et al. 2015).

A population of red massive galaxies are discovered to exist at $z \sim 2$ (Franx et al. 2003; Daddi et al. 2004) and subsequently confirmed to have quiescent stellar population (Cimatti et al. 2004; Daddi et al. 2005; Labbé et al. 2005; Kriek et al. 2006a; Toft et al. 2007; Williams et al. 2009). At this epoch the star formation rate density peaked (Madau & Dickinson 2014) alongside substantial nuclear activity (AGN) (Hopkins et al. 2007). At this time, half of the most massive ($\log_{10}(M_*/M_\odot) > 11$) galaxies are already devoid of star formation (SF), and have old stellar ages suggesting that they quenched their star formation at even earlier times ($z > 3$), when the Universe are only a few Gyr old (e.g. van Dokkum et al. 2006; Kriek et al. 2006b; Franx et al. 2008; van Dokkum et al. 2008; Toft et al. 2009; McCracken et al. 2010; Williams et al. 2010; Wuyts et al. 2011; Brammer et al. 2011; Whitaker et al. 2011; Kado-Fong et al. 2017; Morishita et al. 2019). Nowadays quiescent galaxies are popularly defined by the UVJ color-color relations (see e.g. Muzzin et al. 2013a).

These massive quiescent galaxies are found to be remarkably compact with extremely high stellar densities when compared to local galaxies with similar stellar mass (Papovich et al. 2005; Trujillo et al. 2006, 2007; Buitrago et al. 2008; van Dokkum et al. 2008; Cimatti et al. 2008; Bezanson et al. 2009; Conselice et al. 2011; Szomoru et al. 2012; van der Wel et al. 2014; Mowla et al. 2019). A small number of elliptical galaxies this compact are found in the local Universe (Trujillo et al. 2009; Taylor et al. 2010b; Shih & Stockton 2011; Ferré-Mateu et al. 2012), but these are too young (ages $\sim 2-4$ Gyr) to be the descendants of $z = 2$ compact quiescent galaxies. This suggests that the vast majority of the $z = 2$ population must undergo a substantial increase in size to evolve into local elliptical galaxies (Bell et al. 2012).

Bluck et al. (2012) found that the expected size evolution between $z = 2.5$ and present day can be described primarily by minor mergers. However Newman et al. (2012); Man et al. (2016a) found that minor mergers can account for the evolution at $z < 1$ and that additional mechanisms of growth is required at higher redshift. The minor merger scenario is supported by the continuous size evolution found in compilation of spectroscopic (Damjanov et al. 2011; Belli et al. 2014b; Matharu et al. 2019) and photometric (van der Wel et al. 2014; Faisst et al. 2017; Mowla et al. 2019) studies as well as the expected theoretical predictions of the galaxy properties during merger evolution (e.g. Khochfar & Silk 2006; Naab et al. 2009; Lagos et al. 2018).

To study the dynamics of massive quiescent galaxies at $z > 2$, it is important to obtain both reliable kinematic and morphological measurements using deep spectroscopic observations and

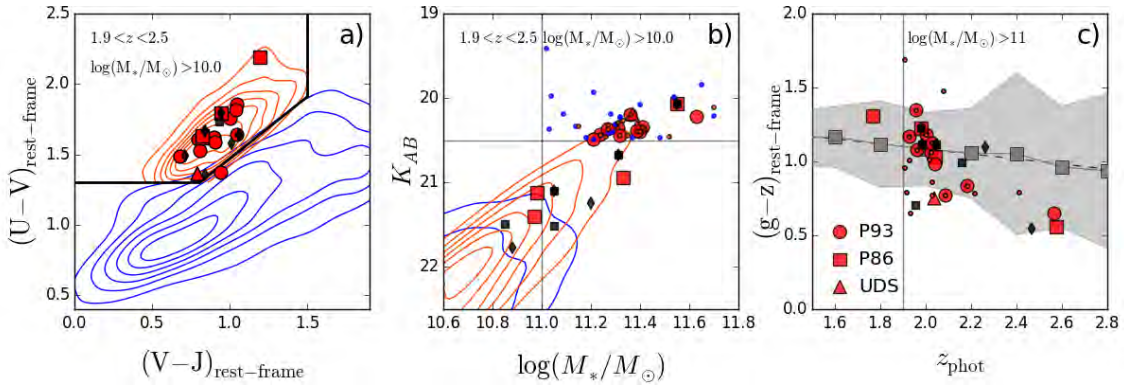

Figure 2.1: Photometric properties of the galaxy sample (red symbols - see legend on right) in the *UVJ* (a), the K_{AB}-$\log(M_*/M_\odot)$ (b), and z_{phot}- rest-frame $(g-z)$ planes from the Muzzin et al. (2013a) catalog. Note that for UDS19627 we use the Toft et al. (2012) K-band, stellar mass, z_{phot} and rest-frame colors estimated from the observed photometry with EAZY (Brammer et al. 2011). The *UVJ* quiescent (red) and star-forming (blue) galaxies are shown in contours in the range $1.9 < z_{phot} < 2.5$ and $\log(M_*/M_\odot) > 10$ (Muzzin et al. 2013a). The spectroscopically confirmed $z > 2$ MQGs from COSMOS are shown with black symbols (square: Krogager et al. (2014), diamond: Belli et al. (2017)). The small red/blue points in (b) are the galaxies that satisfy the criteria $K < 20.5$ and $\log(M_*/M_\odot) > 11$. The gray squares in panel (c) represent the running mean of the rest-frame $(g-z)$ color of the massive, $\log_{10}(M_*/M_\odot) > 11$, *UVJ*-selected quiescent galaxies with the 1σ standard deviation in gray.

high resolution (adaptive optics or space-based) imaging (Kriek et al. 2009b; Toft et al. 2012; van de Sande et al. 2013; Belli et al. 2017). Quiescent galaxies beyond $z > 2$ are more disk-like with higher ellipticities than local ellipticals (Toft et al. 2005, 2007; van der Wel et al. 2011; Wuyts et al. 2011), which may cause heightened dispersion measurements from the contribution of unresolved rotation. In Toft et al. (2017) and Newman et al. (2018), the first spatially resolved gravitationally lensed $z > 2$ massive quiesecent galaxy are observed.

Massive quiescent galaxies at $z \sim 2$ are rare (Arcila-Osejo et al. 2019) and their quiescent nature implies faint rest-frame UV continua with no strong emission lines. Due to their rarity, large survey fields are essential to locate these galaxies. So far only a small samples of massive quiescent galaxies have been spectroscopically confirmed at $z > 2$, in existing surveys like CANDELS+GOODS, and few of those have robust velocity dispersion measurements (van de Sande et al. 2013; Belli et al. 2014b; Kriek et al. 2016; Belli et al. 2017; Morishita et al. 2019).

In this paper, the structural and dynamical properties of 15 *UVJ* massive quiescent galaxies (MQGs), $\log_{10}(M_*/M_\odot) > 11$, at $z > 2$ are studied, doubling the spectroscopically confirmed and absorption-line detected sample at this epoch using the 2 sq. deg. COSMOS and UDS field. These MQGs are examined in detail through their evolution to local galaxies and how they likely formed in minor and major merger processes. In a follow-up paper, the Fundamental Plane relation and its evolution to $z = 0$ is studied (Djorgovski & Davis 1987; Dressler et al. 1987).

In Section 2.2, we present the sample selection of the $z = 2$ galaxies and a corresponding local reference sample. The X-Shooter spectroscopic and *HST* imaging data reduction, alongside the photometry used throughout the paper, are presented in Section 2. In Section 2.4 we present the methods used to extract the X-Shooter absorption-line kinematics and the *HST* structural

properties from the data, together with a multi-wavelength comparison of different star formation tracers. We address the issue of progenitor bias using our local reference sample in Section 2.5.1. We present the stellar population, kinematic and structural results in Section 2.5.2 and 2.5.3, and the dynamical properties in Section 2.5.4. The results and the evolution of these galaxies to $z = 0$ are discussed and summarised in Section 2.6 and 5, respectively. Throughout the manuscript, magnitudes are quoted in the AB system (Oke & Gunn 1983; Fukugita et al. 1996), and the following cosmological parameters are used: $\Omega_m = 0.3$, $\Omega_\Lambda = 0.7$, with $H_0 = 70$ km/s/Mpc. All stellar masses are presented using the Chabrier (2003) Initial Mass Function (IMF).

Table 2.1: Sample Summary

Target ID	RA [degree]	Dec [degree]	$z_{\rm phot}$	Exp. time	K	$S/N_{H_{AB}}$	ESO Program	$(U-V)$	$(V-J)$
UV-108899	150.17661	2.0608871	2.19	5.0	20.35	5.69	093.B-0627(A)	1.60	0.80
UV-250513	149.82227	2.6531196	2.03	5.0	20.37	4.12	093.B-0627(A)	1.58	0.90
CP-561356	150.20888	1.8502616	2.58	5.6	20.94	2.16	086.B-0955(A)	1.63	0.82
UV-105842	150.26265	2.0177791	1.93	4.0	20.20	4.28	093.B-0627(A)	1.75	1.01
UV-171687	149.88702	2.3506956	2.04	5.0	20.49	3.08	093.B-0627(A)	1.37	0.94
UV-90676[b]	150.48750	2.2700379	2.57	5.0	20.22	5.34	093.B-0627(A)	1.53	0.81
CP-1291751	149.86954	2.3167057	1.77	7.2	21.40	1.80	086.B-0955(A)	2.19	1.19
UV-155853	149.55630	2.1672480	1.96	5.0	20.36	4.65	093.B-0627(A)	1.85	1.05
UV-171060[a]	149.78951	2.3413286	2.02	5.0	20.45	3.89	093.B-0627(A)	1.62	0.90
UV-230929	150.20842	2.7721019	2.09	6.0	20.44	6.46	093.B-0627(A)	1.48	0.68
UV-239220	149.43275	2.5106428	2.00	4.5	20.40	2.86	093.B-0627(A)	1.64	1.05
UV-773654	150.74574	2.0104926	1.96	5.0	20.40	2.97	093.B-0627(A)	1.81	1.04
CP-1243752[c]	150.07394	2.2979755	1.98	4.5	20.07	5.25	086.B-0955(A)	1.80	0.94
CP-540713	150.32512	1.8185385	2.04	4.8	21.11	2.98	086.B-0955(A)	1.61	0.82
UDS19627[d]	34.57125	-5.3607778	2.02	5.0	20.19	4.40	X-Shooter GTO	1.36	0.79

Target ID, right ascension (RA), declination (Dec), photometric redshift, X-Shooter near-IR arm exposure time in hours, Total K magnitude, median S/N (9 Å/pixel bins) in H-band ($15000 < \lambda[\text{Å}] < 18000$), ESO program ID, rest-frame $(U-V)$ and $(V-J)$. The RA, Dec, photometric redshift, K-band, and UVJ colors are from Muzzin et al. (2013a) (except UDS19627[d]).

[a]Previously published in Mowla et al. (2019)

[b]Previously published in Kado-Fong et al. (2017); Marsan et al. (2019); Mowla et al. (2019)

[c]Previously published in van de Sande et al. (2013); Krogager et al. (2014); Belli et al. (2014b); Allen et al. (2015); Kriek et al. (2016); Belli et al. (2017); Mowla et al. (2019)

[d]Previously published in Toft et al. (2012) (all values in table taken from there)

2.2 Sample selection

The sample studied here consists of 15 MQGs from the COSMOS and UDS (Williams et al. 2009) fields for spectroscopic follow-up and is selected based on the modeling of their optical to far-infrared broadband SEDs. Three samples, from three periods of observation, are presented below. In the first program, galaxies were identified to be at $z_{\rm phot} > 1.6$ and with old ($>$ 1Gyr), quiescent stellar populations (specific star formation rates $\log({\rm sSFR/yr}) < -11$) in the updated version of the Ilbert et al. (2009) catalog of the COSMOS field described in Man et al. (2012). The four K band brightest ($K < 21.5$) sources covered by parallel *HST*/NICMOS observations where selected for follow-up to enable study of their morphology. These galaxies are referred to as the *P86* sample, named after the period of VLT/X-Shooter observations (P86, 2010-2011).

In a second program, 10 of the K band brightest ($K < 20.5$) galaxies in the COSMOS field with photometric redshifts[1] $z_{\rm phot} > 1.9$, specific starformation rates $\log({\rm sSFR/yr}) < -10$, and stellar masses $\log_{10}(M_*/M_\odot) > 11$ from the Muzzin et al. (2013a) catalog were selected for follow-up. Based on visual inspection, the sources with nearby bright objects in the K band images are excluded to avoid photometric contamination. Objects with *Spitzer*/MIPS 24 μm detections are also excluded to avoid either dusty star-forming galaxies or AGN (Le Floc'h et al. 2009). Their SEDs were visually inspected and galaxies with noisy photometry or bad fits were excluded. This pool of galaxies are dubbed the *P93* sample, observed 3 years after P86.

Finally, in the analysis presented here, the massive quiescent galaxy UDS19627, from Toft et al. (2012), is included. This object are selected as part of early VLT/X-Shooter GTO observations to be quiescent ($\log({\rm sSFR/yr}) < -10$), at a high redshift ($z_{phot} = 2.02^{+0.07}_{-0.08}$) and a bright source ($K = 20.19$) in the UKIRT Ultra Deep Survey (Williams et al. 2009). New *HST*/WFC3 H_{F160W} imaging of this galaxy is presented, allowing us to measure resolved morphology. UDS19627 is minimally gravitationally lensed, but Toft et al. (2012) showed that, after taking this effect into account, the systematic change in magnification factor of $10 - 20$ % correspond to a 0.07 and 0.03 dex resulting lower stellar and dynamical mass.

Our full sample is compiled from the three presented subgroups selected with variations in criteria on stellar mass, sSFR, and K-band brightness. In Figure 2.1a, we show that despite the variation in selection criteria, this sample populates the quiescent galaxy region of the *UVJ* rest-frame color-color diagram (Muzzin et al. 2013b). For the sake of homogeneity the full sample (except for UDS19627) is shown using the Muzzin et al. (2013a) catalog. Our galaxies are consistent with the UVJ selection for massive ($\log(M_*/M_\odot) > 10$) quenched objects at $1.9 < z < 2.5$.

Figure 2.1b shows the position of our sample in the K-band magnitude - stellar mass plane. The $K < 20.5$ and $\log(M_*/M_\odot) > 11$ selection of the P93 sample results in significantly larger stellar masses than the average for the P86 sample (selected as massive quiescent galaxies with

[1] using redshift quality parameter with odds=1

NICMOS coverage) with only 1 galaxy from the latter fully satisfying the criteria of P93 (previously presented in, among others, van de Sande et al. 2013; Kriek et al. 2016; Belli et al. 2017). The power of adding a minimum K-band threshold to the stellar mass criterion to select the most extreme massive quiescent galaxies is evident when comparing our sample with previous studies (van de Sande et al. 2013; Krogager et al. 2014; Belli et al. 2017), identifying on average massive quiescent galaxies with lower stellar masses. Our sample represents 60% of the total number of *UVJ*-MQGs (29% of all galaxies) at $1.9 < z < 2.5$, $\log(M_*/M_\odot) > 11$ and $K < 20.5$ from Muzzin et al. (2013a) (upper right corner of Figure 2.1b). The Anderson-Darling test for k-samples (Scholz & Stephens 1987)[2] confirms that our selection of *UVJ* quiescent galaxies can be considered representative of the massive and K-band brightest galaxies at $1.9 < z < 2.5$.

One concern addressed by van de Sande et al. (2014) is that the selection of the K-band brightest galaxies introduces a bias towards the bluest galaxies in the rest-frame color $(g-z)_{rf}$. To address this issue the rest-frame colors $(g-z)_{rf}$, as a function of redshift between our sample and the *UVJ* selected massive ($\log(M_*/M_\odot) > 11$) quiescent galaxies from Muzzin et al. (2013a), are compared in Figure 2.1c. Contrary to the sample of van de Sande et al. (2014), 13/15 of our galaxies have $(g-z)_{rf}$ colors consistent within the standard deviation of the average massive quiescent galaxies at a matching epoch. The Anderson-Darling test for k-samples confirms that the $(g-z)_{rf}$ colors for our MQGs are representative of the ($\log(M_*/M_\odot) > 11$) *UVJ* massive quiescent galaxies at $1.9 < z < 2.5$. This suggests that, our K-band selected sample is on average not biased towards galaxies with bluer colors. However, the highest redshift sources have systematic lower $(g-z)_{rf}$ colors and could be subjected to this selection bias.

In summary, our sample is selected to be the most massive K-band bright *UVJ* quiescent galaxies at $z > 2$. The selection is not subjected to a bias in $(g-z)_{rf}$ and can be considered a 60 % stellar mass and K-band complete sample of the quiescent galaxies at $z > 2$.

2.2.1 A suitable reference sample of local galaxies

The MASSIVE Survey samples the most massive K-band selected early-type galaxies within the local 108 Mpc northern hemisphere (Ma et al. 2014). These galaxies have central stellar ages suggesting a formation epoch at $z > 2$ (Greene et al. 2015). Given the similar selection for our MQGs at $z > 2$, stellar masses and inferred formation epoch, this sample is adopted as the local reference sample. This sample is further motivated in Section 2.5.1.

The stellar masses and the structural and dynamical parameters were compiled analogously to our $z = 2$ MQGs. The extinction-corrected absolute K-band magnitudes listed in Table 3 of Ma et al. (2014) are converted into stellar masses using Equation (1) in van de Sande et al. (2019). The NASA-Sloan Atlas semi-major axis optical effective radii, also listed in Table 3 of Ma et al.

[2] https://docs.scipy.org/doc/scipy/reference/generated/scipy.stats.anderson_ksamp.html

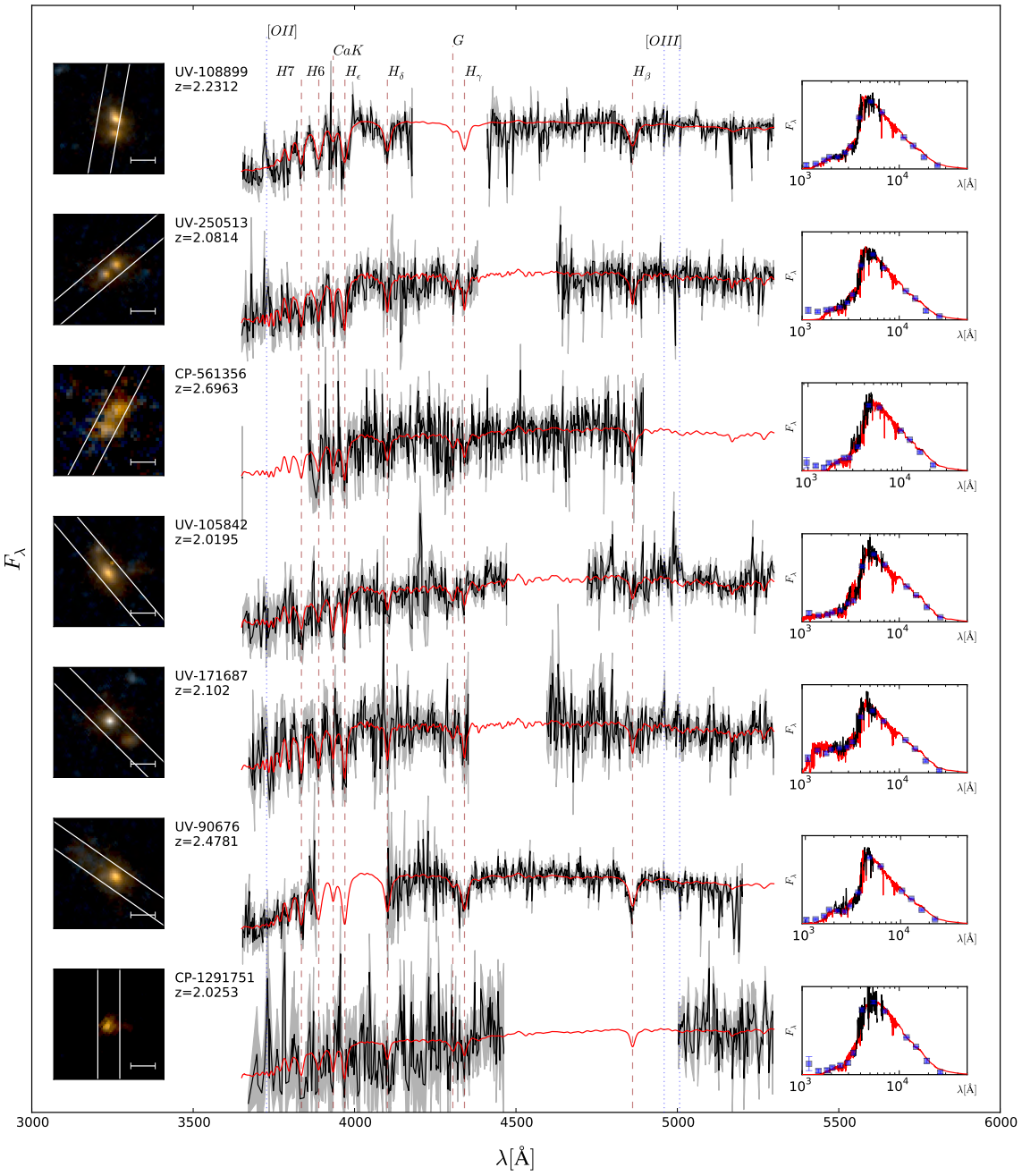

Figure 2.2: VLT/X-Shooter spectra, of our sample, covering the rest-frame wavelength range $3650 < \lambda < 5300$ Å with corresponding HST RB images, in the left column. To the right, the full SED displayed by multi-wavelength photometry (blue squares) and in center the UV-to-optical X-Shooter spectra (black line) and the best-fit stellar population model (red line, Section 2.4.3). Spectra are shown with an optimal adaptive binning and 1σ rms noise in gray shading. The two-color $4.5" \times 4.5"$ North-East orientated RB images, with X-Shooter slit overlay, are made from *HST*/ACS I_{F814W} and WFC3 H_{F160W}. A 1" white bar is shown (~ 8.5 kpc at $z = 2$). The G, Ca K, and Balmer absorption features are indicated with dark red dashed lines. The $\sim 2\sigma$ [OII]3727Å emission in UV-108899 and UV-239220 (see Table 2.2) are indicated alongside the [OIII]4959, 5007Å with blue dotted lines. Listed below the galaxy ID, the absorption-line determined spectroscopic redshifts (determined in Section 2.4.1) is shown.

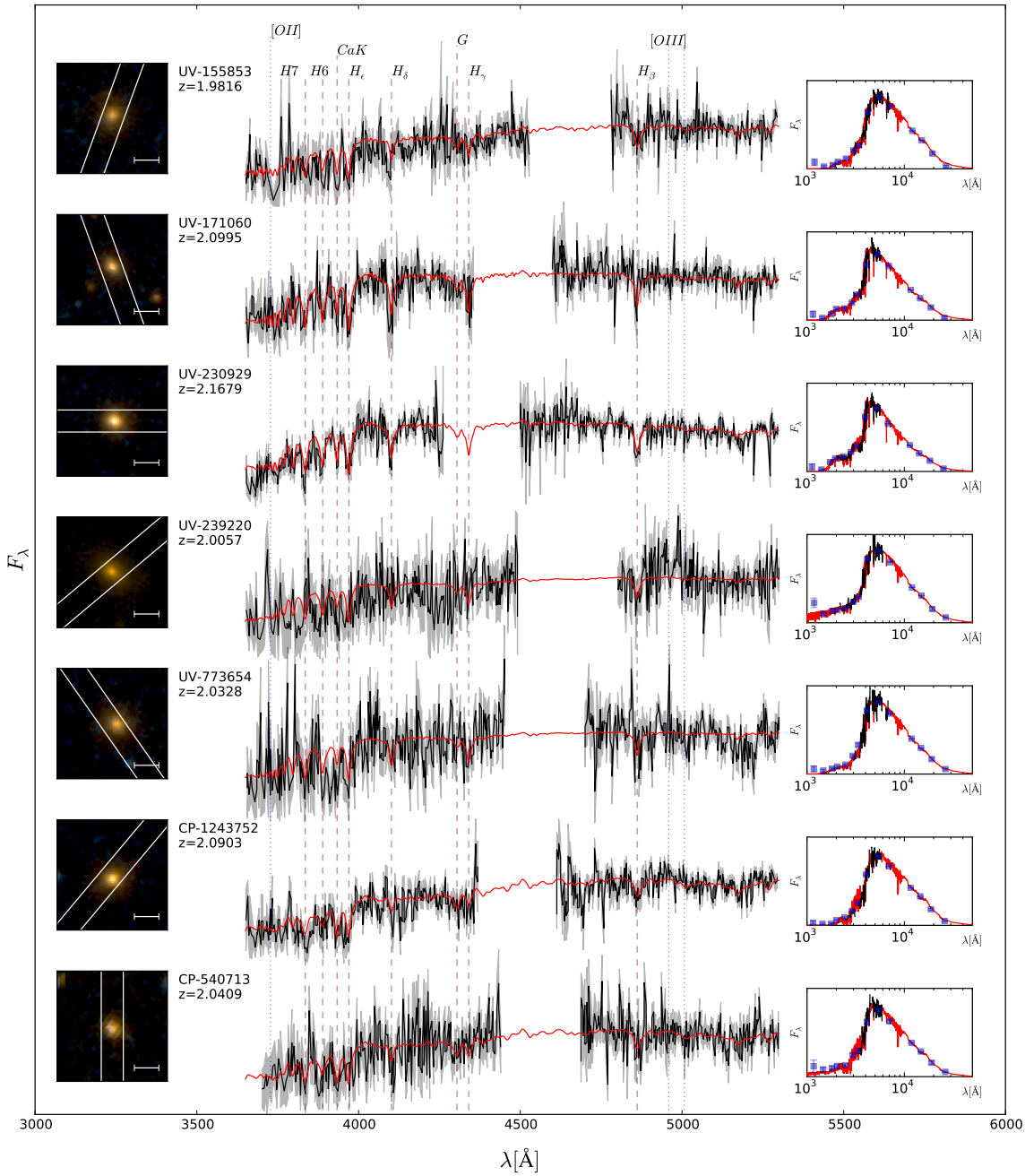

Figure 2.3: Similar to Figure 2.2, with isolated spheroidal type morphology (again following the order of Table 2.3). The spectra show the 4000 Å break, strong Balmer absorption lines and a lack of emission lines. Furthermore, the H_{F160W} images and full photometric SED reveal bright sources with old stellar populations and low rest-frame UV light.

(2014), are used. These were derived from two-dimensional Sérsic (Sersic 1968) fits with Sérsic parameters varying between $n = 2 - 6$. For the galaxies where this is not available, the infrared 2MASS measurements were used to convert these to semi-major axis optical effective radii using Equation (4) in Ma et al. (2014). These sizes were derived from single Sérsic and de Vaucouleurs profile fits ($n = 4$). The effective velocity dispersion measurements used are reported in Veale et al. (2018). They were estimated using the MILES stellar library (Falcón-Barroso et al. 2011) together with pPXF (Cappellari & Emsellem 2004). Finally, the average luminosity-weighted stellar velocity dispersion within the effective radius is adopted.

2.3 Data

Here, we describe the spectroscopic observations with the VLT/X-Shooter spectrograph (D'Odorico et al. 2006; Vernet et al. 2011) and the *HST*/WFC3 follow-up of our MQGs. These spectroscopic and photometric campaigns spanned an interval of more than 10 years, spread over several programs that are summarized in Table 2.1. Finally, the ancillary data used in the analysis are presented.

2.3.1 VLT/X-Shooter spectroscopy

X-shooter is a single object Echelle spectrograph mounted on the VLT and covers $3,000-25,000$ Å with three arms: UVB ($2936 - 5930$ Å), VIS ($5,253 - 10,489$ Å), and NIR ($9,827 - 24,807$ Å). We are granted 35 and 57 service mode hours in P86 and P93, respectively (PI: Toft). The latter carried over and finished in period 96. The observations are completed using default nodding mode to ensure a robust sky subtraction of the NIR band, probing the rest-frame optical part of the spectra for the $z \sim 2$ quiescent galaxies. The majority of the P86/P93 observations ($89/96\%$) are completed with an average air-mass corrected DIMM seeing of $0\farcs8$ in the NIR arm. The telluric standard stars are observed close to the science observations, both in airmass and time to mimic the conditions of the sky and optimize the atmospheric absorption correction. The P86/P93 observations for the NIR (VIS) frames are executed with 480s/900s (314s/863s) exposures, $0.9" \times 11"$ slit configuration and – for the P93 sample only – including the K-band blocking filter. We aligned the slit along the galaxy's major axis in the UltraVISTA K-band images avoiding bright nearby sources.

The data are reduced using a wrapper of the ESO X-shooter pipeline (Modigliani et al. 2010; Sparre 2015), along with customized modifications (Zabl et al. 2015). Beyond the standard pipeline processing steps for the NIR arm in nodding mode, we account for the spatial variations of the background level outside of the orders in each raw science frame by removing the median level obtained from the illuminated areas from each row of pixels in the detector. The 2-D VIS and NIR individual science frames are corrected for telluric absorption with a customized and publicly

available wrapper[3] (Selsing et al. 2016) of the Penalized Pixel-Fitting algorithm (Cappellari & Emsellem 2004, pPXF), based on the PHOENIX stellar atmosphere library (Husser et al. 2013). A response function is constructed modeling the atmosphere during the science exposures and each individual observation block (OB) are corrected.

Finally, individual OBs are combined into an optimally weighted 2-D spectrum removing flux outliers using a 3 and 5σ median clipping for the VIS and NIR, respectively. Bad pixels automatically flagged during the reduction are also excluded. Furthermore, off-trace emission is flagged and excluded in the construction of the OBs from UV-105842, UV-171687, and UV-155853 to minimize the contamination from surrounding sources. The 1-D spectrum is optimally extracted (Horne 1986). Flux corrections are made anchoring the synthetic photometry to the total magnitudes from the latest COSMOS15 catalog (Laigle et al. 2016) (Section 2.3.3), accounting for PSF matching in different bands and for the Galactic extinction. The H-band and I-band magnitudes are used to compute independent aperture correction factors for the NIR and VIS spectra, respectively.

2.3.2 HST/WFC3 H_{F160W} imaging

11 orbits of *HST*/WFC3 with HST-GO-14721 (PI: Conselice) are allocated to observe the rest-frame optical images, H_{F160W}, for UDS19627 and the 10 galaxies in the *P93* sample. The *P86* sample are covered by the following programs: CP-1243752 (HST-GO-12440, PI: Faber) and CP-561356 (HST-HLA-14114, PI: van Dokkum) with WFC3; CP-1291751 and CP-540713 with HST/NICMOS (HST-HLA-9999, PI: Scoville).

The WFC3/H_{F160W} data is reduced using the "Grism redshift and line" analysis software, Grizli[4], which is an end-to-end processing code for WFC3/IR data using ASTRODRIZZLE[5]. The starting point is the standard calibrated images downloaded from the MAST archive (FLT extension images). The calibrated images are 1014×1014 pixels with $0''.13/\mathrm{pixel}$. For each visit, there are four dithered exposures that are combined using Grizli. The resulting products for each visit are aligned, background subtracted and drizzled images with $0''.06/\mathrm{pixel}$. The NICMOS data for CP-1291751 and CP-540713 are reduced in a similar manner with ASTRODRIZZLE.

2.3.3 Ancillary data: multi-wavelength photometry and *HST* I_{F814W} images

We make ample use of the 14 broadband COSMOS photometry from the Laigle et al. (2016) catalog, covering the full UV-to-NIR wavelength range to model our stellar populations in Section 2.4.3. The total magnitudes are adopted using the method described in Appendix A.2 by the same authors. Complementary to the UV-to-NIR photometry, we check the available deep X-ray

[3] https://github.com/jselsing/QuasarComposite/blob/master/py/telluric.py
[4] https://github.com/gbrammer/grizli/
[5] A Python implementation of Multidrizzle: https://drizzlepac.readthedocs.io/en/latest/astrodrizzle.html

Chandra imaging (Marchesi et al. 2016) and the "super-deblended" far-infrared (FIR) catalog (Jin et al. 2018), superseding the previous 24 μm catalog (Le Floc'h et al. 2009) used in the selection of *P93*. This new implementation adopts active priors from the *Spitzer*/MIPS 24 μm and radio observations to deblend the low resolution imaging from *Herschel*/PACS and SPIRE, SCUBA2, AzTEC, and MAMBO. The sources are cross-check with the GALEX far-UV and near-UV data from Zamojski et al. (2007) and Capak et al. (2007). This search for UV or X-ray counterparts results in no detections for any of our galaxies. On the other hand, we do find hints of mid-infrared (MIR) and radio emission from part of the sample, as detailed in Section 2.4.4.2 and discussed in Section 2.6.3. UDS19627 has similar UV-to-NIR multi-wavelength coverage. For an in-depth discussion of the available photometric data for this object, see Toft et al. (2012).

$13/15$ galaxies have *HST* I_{F814W} imaging that are part of the COSMOS public released data (Scoville et al. 2007; Koekemoer et al. 2007). It covers $\sim$ 2 sq degrees of the sky with the Advanced Camera for Surveys (ACS) in the I-band and comprises 81 tiles. Each tile is observed in 4 dithered exposures that are combined to produce a pixel scale of $0\farcs03$/pixel and a Point Spread Function (PSF) of $0\farcs095$ at full width at half maximum (FWHM). COSMOS images reach a point source limiting depth of $AB(F814W) = 27.2$ (5σ).

2.4 Analysis

We present in this section the analysis of our X-Shooter spectra and our *HST*/WFC3 H_{F160W} images. The spectroscopic redshift, the velocity dispersion and stellar population of our galaxies are measured by modeling the absorption features in the stellar continuum together with the broadband photometry. As we find no significant emission line detections in the spectra, we derive optical SFR upper limits (Section 2.4.4) which we compare with the estimates from the MIR photometry. The majority of the spatially offset sources caught in the spectra are foreground and background galaxies. Finally, the *HST* images probing the rest-frame optical structure are modeled to obtain their morphological parameters. The major merger candidates (UV-108899, UV-250513, and CP-561356 - see Figure 2.2) are confirmed to be within redshift proximity such that their stellar masses reliably can be flux corrected.

The *HST* Red-Blue (RB) color images, rest-frame optical X-Shooter spectra with (Laigle et al. 2016) photometry and our best fitting stellar population model is shown in Figure 2.2 and 2.3. For UDS19627, the HST/WFC3 H_{F160W} image is presented in Section 2.4.5 and its spectrum is shown in Toft et al. (2012).

2.4.1 Spectroscopic redshifts and stellar velocity dispersion

All spectra of targeted sources (*P86* and *P93*) show prominent hydrogen absorption features, which are typical of evolved stellar populations (see Figure 2.2 and 2.3). The stellar absorption

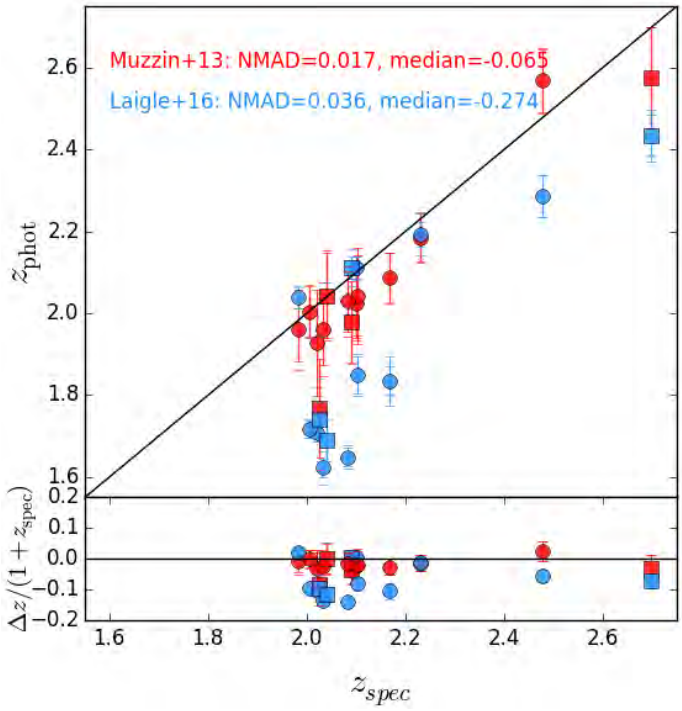

Figure 2.4: Comparison of spectroscopic and photometric redshifts for our sample of massive quiescent galaxies using the Muzzin et al. (2013a) (red) and Laigle et al. (2016) (blue) catalogs. The Muzzin et al. (2013a) catalog provides better photometric redshift estimates for massive quiescent galaxies at $z > 2$ compared to Laigle et al. (2016). Note that UDS19627 is not in the same area of the sky covered by the catalogs compare here.

features are modeled using pPXF, and both the line of sight velocity centroid (i.e., the spectroscopic redshift) and the line of sight stellar velocity dispersion (LOSVD, hereafter "velocity dispersion") are measured.

The initial redshift and velocity dispersion guess is obtained from running pPXF with the (Bruzual & Charlot 2003) stellar population library (hereafter BC03). The stellar population analysis is performed with complex star formation histories (SFHs) fitting of the spectra and SED (see Section 2.4.3) adopting this initial estimate. The resulting best fit model is confirmed to be stable against perturbations of $\Delta\sigma = \pm 100$ km/s. The velocity dispersion measurement is refined, by rerunning pPXF with a non-velocity broadened best-fit stellar population model.

The spectra and best-fit model are convolved to the same resolution ($FWHM = 3.2$ Å) and rebinned to a constant velocity scale without additional interpolation. Low order additive (a=2) and multiplicative (m=2) correction polynomials are fit over the rest-frame range $3750 - 5950$ Å. The JH band gap and the regions, where emission lines might be expected[6], are excluded while also masking out bad pixels.

The associated systematic and statistical errors are quantified by varying the wavelength range, correction polynomials, and stellar libraries (see details in Appendix C), similar to the

[6]Excluded emission lines (wavelengths in Å): [OII] (3726.03, 3728.82), [OIII] (4958.92, 5006.84), [OI] (6300.30), [NII] (6548.03, 6583.41), Hα (6563), and [SII] (6716.47, 6730.85)

method used in Toft et al. (2017). In all cases (*P86* and *P93*), we determine secure redshifts and for $10/14$ galaxies we estimate robust velocity dispersions. These estimates are reported in Table 2.3 along with the combined systematic and statistical errors (Appendix C). In the same table, we also list the velocity dispersion for UDS19627 derived in Toft et al. (2012). In Figure 2.4, the derived spectroscopic redshift are compared with the photometric estimates from Muzzin et al. (2013a) and Laigle et al. (2016). Using the Normalised Median Absolute Deviation (σ_{NMAD}) from Brammer et al. (2008), no catastrophic outliers are found except for photometric redshifts being systematically below the spectroscopic redshifts for both catalogs, finding a better agreement for Muzzin et al. (2013a).

Table 2.2: The Stellar Population Model Parameters

Target ID	$z_{\rm spec}$	$\log(M_*/M_\odot)$	$\log(\mathrm{Age/yr})$	A(g)	$\mathrm{SFR_{SSP}[M_\odot/yr]}$	$\mathrm{SFR_{opt}[M_\odot/yr]}$	$\mathrm{SFR_{24}[M_\odot/yr]}$[a]
UV-108899	2.2301	$11.62^{+0.16}_{-0.18}$	$9.15^{+0.27}_{-0.30}$	$0.38^{+1.00}_{-0.38}$	< 6	6 ± 4 ([OII])	< 15
UV-250513	2.0814	$11.51^{+0.18}_{-0.19}$	$9.16^{+0.27}_{-0.31}$	$0.38^{+1.02}_{-0.38}$	< 6	< 3 (Hα)	< 13
CP-561356	2.6963	$11.62^{+0.21}_{-0.20}$	$9.14^{+0.28}_{-0.32}$	$0.62^{+1.17}_{-0.62}$	< 74	< 19 ([OII])	$< 90^{\oplus}$
UV-105842	2.0195	$11.68^{+0.16}_{-0.17}$	$9.19^{+0.26}_{-0.33}$	$0.81^{+1.04}_{-0.81}$	< 9	< 2 (Hα)	19 ± 5
UV-171687	2.1020	$11.51^{+0.18}_{-0.19}$	$9.13^{+0.28}_{-0.32}$	$0.64^{+1.13}_{-0.64}$	< 16	< 3 (Hα)	$26 \pm 6^{\diamond\oplus}$
UV-90676	2.4781	$11.78^{+0.17}_{-0.18}$	$9.09^{+0.29}_{-0.29}$	$0.41^{+0.99}_{-0.41}$	< 64	< 6 ([OII])	$< 92^{\diamond\oplus}$
CP-1291751	2.0253	$11.24^{+0.23}_{-0.22}$	$9.17^{+0.27}_{-0.33}$	$0.82^{+1.26}_{-0.82}$	< 10	< 2 (Hα)	18 ± 4
UV-155853	1.9816	$11.62^{+0.18}_{-0.17}$	$9.23^{+0.24}_{-0.33}$	$0.88^{+1.04}_{-0.86}$	< 6	< 4 (Hα)	< 15
UV-171060	2.0995	$11.48^{+0.16}_{-0.17}$	$9.16^{+0.27}_{-0.31}$	$0.41^{+1.03}_{-0.41}$	< 6	< 2 (Hα)	$< 15^{\diamond}$
UV-230929	2.1679	$11.48^{+0.16}_{-0.16}$	$9.10^{+0.28}_{-0.28}$	$0.22^{+0.89}_{-0.22}$	< 3	< 4 ([OII])	< 7
UV-239220	2.0057	$11.57^{+0.20}_{-0.20}$	$9.18^{+0.26}_{-0.33}$	$0.66^{+1.14}_{-0.66}$	< 9	35 ± 15 (Hα)	$21 \pm 4^{\diamond\oplus}$
UV-773654	2.0328	$11.59^{+0.19}_{-0.20}$	$9.20^{+0.26}_{-0.33}$	$0.68^{+1.13}_{-0.68}$	< 5	< 2 (Hα)	$13 \pm 3^{\diamond\oplus}$
CP-1243752	2.0903	$11.79^{+0.17}_{-0.17}$	$9.23^{+0.24}_{-0.32}$	$0.76^{+1.06}_{-0.76}$	< 5	< 2 (Hα)	< 12
CP-540713	2.0409	$11.26^{+0.22}_{-0.23}$	$9.16^{+0.27}_{-0.32}$	$0.57^{+1.19}_{-0.57}$	< 6	< 2 (Hα)	< 12
UDS-19627[†]	2.0389	$11.37^{+0.13}_{-0.10}$	$9.08^{+0.11}_{-0.10}$	$0.77^{+0.36}_{-0.32}$	...	< 6 (Hα)	< 40[b]

Column 1: Target ID, Column 2: Spectroscopic redshift, Column 3: Stellar mass, Column 4: mass-weighted stellar age, Column 5: Extinction in g-band, Column 6: 2σ upper limit percentiles of the stellar population modeled SFR/100 Myr distribution, Column 7: 3σ SFR upper limits based on Hα or [OII]λ3727 (Section 2.4.4.1), Column 8: 24 μm estimated SFR (see Section 2.4.4.2).

[†]The values listed for UDS19627 is from Toft et al. (2012). From this study the $A(v)$ extinction instead of the listed $A(g)$ is quoted.

[a]Galaxies with detections in 1.4 GHz ($^{\diamond}$) and 3 GHz ($^{\oplus}$) are indicated with matching symbols.

[b]2σ 24 μm SFR upper limit using method from Franx et al. (2008)

2.4.2 Emission lines

No on-source nebular line emission is detected at 3σ for any objects in the sample. For UV-108899, UV-239220 and UV-90676 we find indications of emission ($\sim 2\sigma$) from [OII]$3726.2, 3728.9$ and Hα6563. In Appendix B, we discuss the specifics of the fitting method and list, in Table 2.2, the SFR and uncertainties from the [OII] and Hα (Kennicutt 1998). Furthermore, spatially offset line emission is observed in four (UV-155853, UV-171687, UV-171060, UV-105842) 2-D spectra coinciding with close proximity sources. In 3/4 cases, this emission arises from foreground or background sources (Appendix A.2). The latter source north-east of UV-105842 shows significant [OII]$3726.2, 3728.9$ Å, [OIII]$4959, 5007$Å, and Hα emission with a matching redshift of $z = 2.0124$. This corresponds to a velocity offset of 2130 ± 120 km/s from UV-105842. If purely due to galaxy motion, such an offset suggests that the two sources are not gravitationally bound at the time of observation. Another explanation of the asymmetric morphology might be a high redshift analog of the locally observed offset AGN (Comerford & Greene 2014), likely caused by recent merger event.

2.4.3 Stellar population modeling of continuum emission

In order to put constraints on the physical parameters of the stellar populations, the VIS+NIR X-Shooter spectra and the broadband photometry are fit with the Bayesian approach, from Gallazzi et al. (2005) (recently revised in Zibetti et al. (2017)), using the derived spectroscopic redshift. Spectral regions of poor atmospheric transitions are not included in the calculation. Before fitting, the models are convolved by the initial velocity dispersion estimated in Section 2.4.1.

Models are obtained by convolving the latest revision of BC03 Simple Stellar Population (SSP) models using the MILES stellar libraries (Sánchez-Blázquez et al. 2006; Falcón-Barroso et al. 2011) with a large Monte Carlo library of star formation histories, metal enrichment histories and dust attenuations. The prior distribution of models is the one described in Zibetti et al. (2017), but here limited to 50,000 models with formation ages younger than 5 Gyr to be consistent with the high redshift of our galaxies. A full description of the model library is given in Zibetti et al. (2017), however the most relevant information are summarized here.

SFHs are modeled with a continuous component parametrized à la Sandage (1986)[7], thus allowing for both an increasing and a decreasing SFH phase, on top of which random bursts of star formation are added. Stellar metallicity evolves according to the SFH (see Zibetti et al. (2019)), with initial and final values randomly generated in the range $1/50 - 2.5Z_{\odot}$. Finally, for 75% of the models, the effect of dust attenuation is included following the model of Charlot & Fall (2000) that separates the contribution of the birth clouds affecting stars younger than 10^7 yr and the contribution of the ISM affecting stars of all ages.

[7] $SFR(t) = t/\tau \times exp(-t^2/(2\tau^2))$, see e.g. Section 3.1 in Zibetti et al. (2019)

The Bayesian modeling approach assumes the likelihood of each model to be $\propto exp(-\chi^2/2)$. The probability distribution function (PDF) of each physical parameter of interest are computed by weighing the prior distribution of the models in a given parameter by their likelihood, marginalizing over all the other parameters. We additionally used the information from the mid-IR flux limit to restrict the sample of acceptable models to those that have a SFR consistent with the $24\ \mu m$-based upper limits and detections (see Section 2.4.4.2). The median and the 16^{th} and 84^{th} percentiles of the PDFs are adopted as the fiducial estimates and their uncertainties for each parameter. Note that this approach allows the derivation of realistic uncertainties on the key physical parameters, accounting for both the observational errors and the intrinsic degeneracies among different parameters.

The stellar mass, mass-weighted mean stellar age, effective dust attenuation ($A(g)$) and SFR, averaged over the last 100 Myr for our sample, are reported in Table 2.2. In this table, the SFR limits from nebular line and $24\ \mu m$ emission (see Sections 2.4.4.1 and 2.4.4.2) are also listed. Stellar masses are within the range of $\log_{10}(M_*/M_\odot) = 11.23 - 11.79$, with a median of 11.57. Compared to Belli et al. (2017), this sample is on average more massive, which is reflected by the brighter K-band magnitudes (see Figure 2.1). Such massive quiescent galaxies have also been found over a larger area in Arcila-Osejo et al. (2019). The SFR limits and dust-corrected stellar masses, together with the mean stellar mass weighted ages of ~ 1.4 Gyr, confirm the expectations from the selection that this is, in fact, a sample of massive recently quenched galaxies. Three of the galaxies are double sources and the stellar masses are corrected in Section 2.4.6.

2.4.4 Star formation and quiescence

2.4.4.1 Rest-frame optical emission lines

In order to confirm the quiescence nature of our galaxies upper limits on [OII]λ3727 and Hα emission are measured. These are converted into upper limits of the unobscured SFRs following Equation (2) and (3) in Kennicutt (1998), under the assumptions of solar abundance ratio and that all massive star formation is traced by ionized gas. A 3σ flux upper limit is determined by summing up the flux error density squared over a region of $\Delta\lambda = 1000$ km/s (similar to $300 - 500$ km/s line dispersions)

$$F_{3\sigma\ limit} = 3\sqrt{\sum \sigma_{flux}^2 \delta\lambda^2}. \tag{2.1}$$

Here σ_{flux} and $\delta\lambda^2$ are the flux uncertainty and bin size, respectively. Note that we do not introduce any dust extinction in this conversion, as this is largely unconstrained (see Section 2.4.4.3 for an estimated upper limit on the dust extinction). We find unobscured SFR upper limits that are consistent with the expectation that these galaxies are quiescent ($-10 < \log_{10}(\mathrm{sSFR/yr}) < -11.5$). The values are listed in Table 2.2.

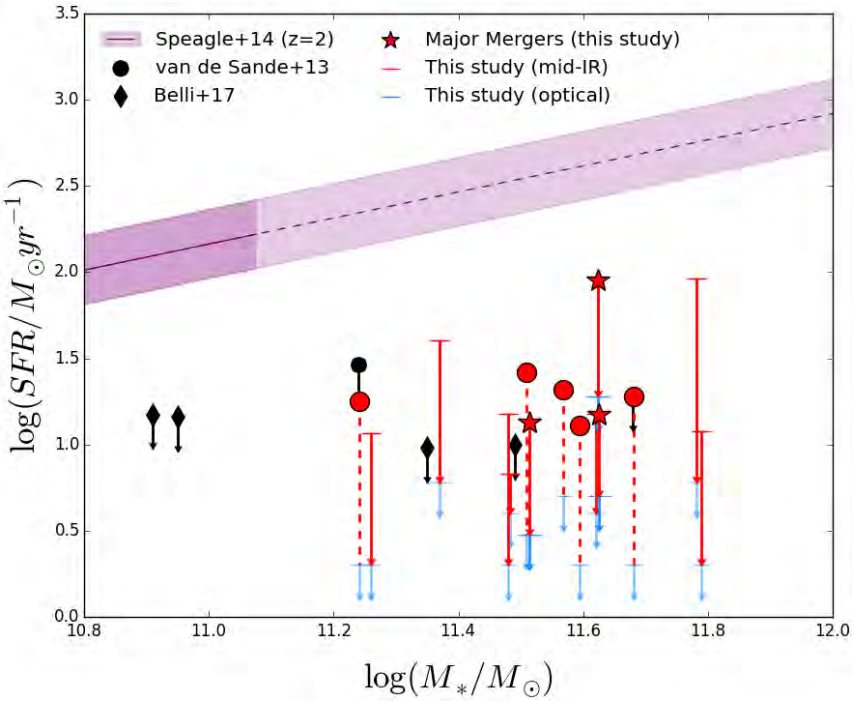

Figure 2.5: SFR – M_* plane for massive quiescent galaxies at $z > 2$ with 24 μm coverage. The SFR main-sequence at $z = 2$ from Speagle et al. (2014) is shown in dark purple, with its 0.2 dex (1σ) scatter. The light purple region extending beyond $\log(M_*/M_\odot) > 11.1$ is an extrapolation of the best-fit relation. The 24 μm MIPS SFR detections (red circles)/upper limits (red arrows) are shown, with the major mergers (composite measurement of the SFR) in red stars. We show our rest-frame optical $\mathrm{SFR}_{3\sigma}$ (based on [OII] and Hα) in blue upper limits. We show 24 μm SFR upper limits for the 2 objects from van de Sande et al. (2013) (circles), together with 4 dust-corrected Hα upper limits from Belli et al. (2019) (diamonds) in black upper limits. Our sample of galaxies have suppressed SFR compared to the main-sequence at $z = 2$ and can be considered truly quiescent galaxies.

2.4.4.2 Mid-infrared emission

The SFR, derived from rest-frame optical emission lines, represents a lower limit to the total star formation in the presence of strong dust attenuation. Therefore, the SFR from the *Spitzer*/MIPS 24 μm emission (Wu et al. 2005; Zhu et al. 2008; Rieke et al. 2009; Kennicutt et al. 2009) are estimated under the assumption of zero or subdominant AGN emission. Here, the 24 μm flux densities (or 3σ upper limits for sources undetected at 24 μm), from the most recent "super deblended" FIR COSMOS catalog (Jin et al. 2018), are adopted. To derive SFR estimates, the $z = 2$ main-sequence SED template of Magdis et al. (2012) is rescaled to the measured 24 μm flux densities (or the 3σ upper limits) of our targets. The emerging total infrared luminosity (L_{IR}) of the templates are converted to SFR through the L_{IR}-SFR relation of Kennicutt (1998), tuned to the adopted Chabrier IMF of this study. Detections corresponding to a median SFR $\sim 20\ M_\odot \mathrm{yr}^{-1}$ are found for 5 of the galaxies that are undetected in the 24 μm catalog (Le Floc'h et al. 2009). The remaining galaxies are not individually detected and we thus fix them to their 3σ upper limit. UV-90676 and CP-561356 that have upper limits of $\lesssim 90\ M_\odot \mathrm{yr}^{-1}$. Both galaxies show strong merger signatures (see Figure 2.7). The derived 24 μm SFR are listed in Table 2.2.

2.4.4.3 Comparison of different star formation tracers

Figure 2.5 shows the position of the sample of MQGs in the $\log(\mathrm{SFR}) - \log(\mathrm{M}_*)$ main-sequence at $z = 2$. For reference, the SFR main-sequence at matching redshift from Speagle et al. (2014) is shown, extrapolated to the stellar mass range $\log_{10}(M_*/M_\odot) > 11.1$ covered by our galaxies.

The rest-frame optical SFR limits are systematically lower than the mid-IR estimates (both probing $10 - 100$ Myrs timescales). This suggests either that the star-forming regions are strongly obscured and/or AGN dust heating (Fumagalli et al. 2014). Under the assumption of no AGN contribution to the heating that produces the mid-IR emission (see also Section 2.6.3), the dust extinction is estimated by comparing the obscured and un-obscured SFR estimates, resulting in a mean extinction of $A(v) < 1 - 2$ consistent with our SED fit derived $A(g)$ (g-band) extinction. In order to judge if a significant contribution to the mid-IR heating arises from AGN, we check if there are any radio counterparts detected in Jin et al. (2018). Radio emission is detected in 5 sources at 1.4 GHz and in 5 sources at 3 GHz (indicated with symbols in Table 2.2), showing that AGN heating could be responsible for the elevated mid-IR SFR estimates. Further treatment of the radio detections will be part of a future paper (Cortzen at al. in prep).

The SFRs derived from our stellar population analysis (Section 2.4.3) are consistent with $\mathrm{SFR} \sim 0\ \mathrm{M}_*\mathrm{yr}^{-1}$ for all galaxies in our sample. In Table 2.1, we list the 2σ upper limits on these SFRs. However, even considering the most conservative upper limits on the SFR from the 24 μm emission, our sample of MQGs lies ~ 2 dex below the SFR main-sequence at their redshifts, confirming their quiescent nature.

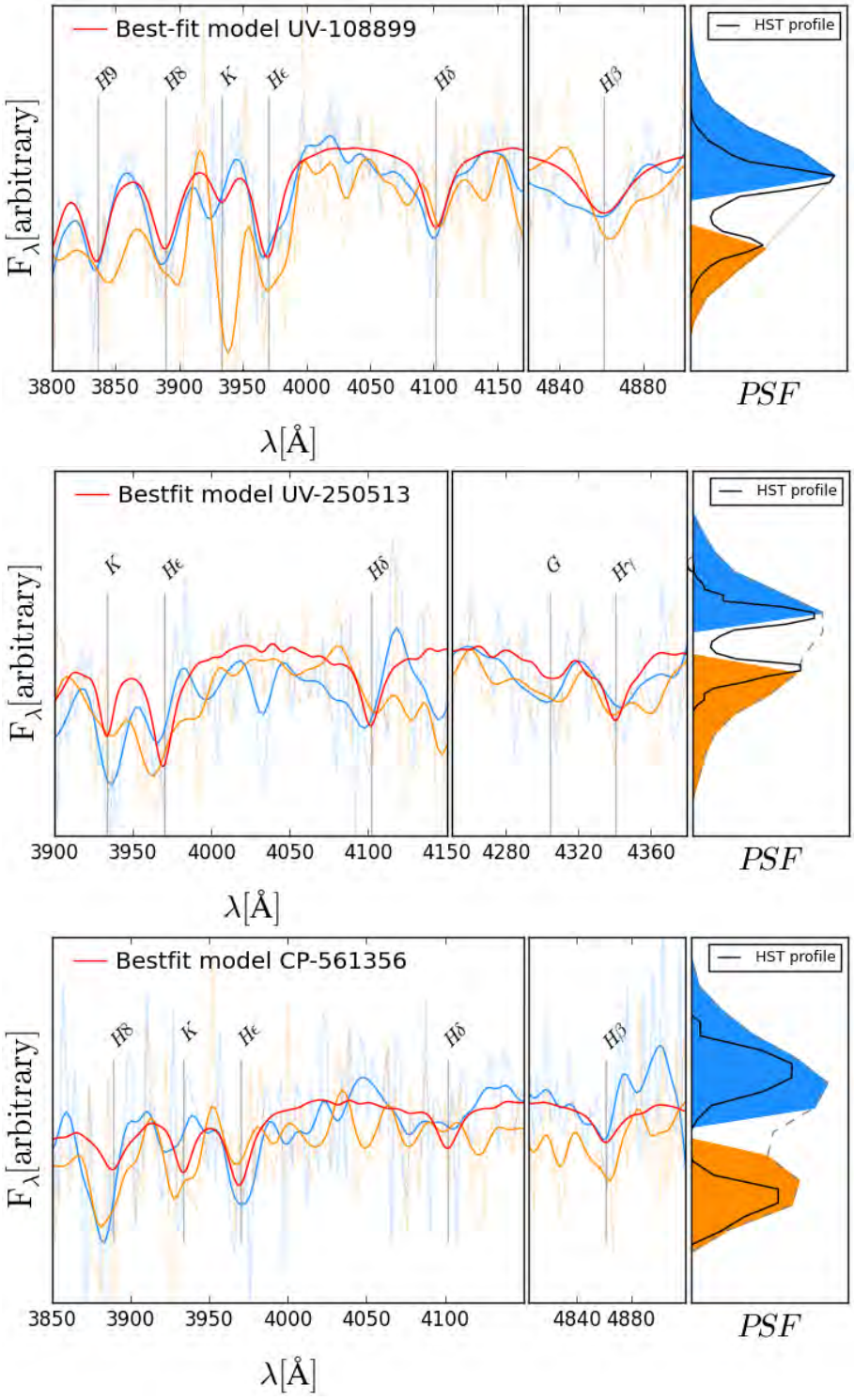

Figure 2.6: Individual flux extractions (blue, orange) from spatially divided 2-D spectra of the major merger candidate sources UV-108899, UV-250513, CP-561356 (top to bottom). The right panel shows the wavelength collapsed 2-D spectrum (grey line) color coded to match the individual extracted 1-D spectra (left, center panel). For reference the 1-D resolved *HST* H_{F160W} profile is shown in thin black line. The best fit model of the composite spectrum is shown in red and the visible Balmer absorption lines are indicated. For each galaxy we confirm the spectroscopic redshift proximity by the matching of absorption lines and conclude that these sources are ongoing major mergers.

Table 2.3: Summary of Structural Properties

Target ID	$z_{\rm phot}$	$z_{\rm spec}$	σ [km/s]	R_{maj} [kpc]	n	q	$R^{\rm b}_{\rm Flux}$	$\log_{10}(M_{*,c}/M_{\odot})$	$\log_{10}(M_{\rm dyn}/M_{\odot})$	Class[c]
UV-108899-1[a]	2.19	2.2301	470 ± 82	1.36 ± 0.14	2.51	0.44	0.56	$11.38^{+0.16}_{-0.18}$	...	P†
UV-108899-2[a]	...	...	...	3.38 ± 0.34	7.15	0.56	0.44	$11.26^{+0.17}_{-0.17}$	...	P†
UV-250513-1[a]	2.03	2.0814	174 ± 44	3.84 ± 0.38	4.00	0.59	0.55	$11.26^{+0.17}_{-0.19}$	...	P†
UV-250513-2[a]	...	...	...	1.60 ± 0.16	4.00	0.63	0.45	$11.16^{+0.17}_{-0.18}$	...	P†
CP-561356-1[a]	2.43	2.6963	280 ± 128	4.14 ± 0.41	1.45	0.62	0.71	$11.47^{+0.21}_{-0.20}$	...	P†
CP-561356-2[a]	...	...	...	2.78 ± 0.28	0.90	0.39	0.29	$11.09^{+0.21}_{-0.21}$	...	P†
UV-105842-1	1.93	2.0195	263 ± 57	4.07 ± 0.41	3.51	0.51	1.00	$11.68^{+0.16}_{-0.17}$	11.61 ± 0.19	P
UV-171687-1	2.04	2.1020	182 ± 50	5.12 ± 0.51	4.00	0.77	1.00	$11.51^{+0.18}_{-0.19}$	11.37 ± 0.24	P
UV-90676	2.57	2.4781	347 ± 82	5.22 ± 0.51	4.98	0.61	1.00	$11.78^{+0.17}_{-0.18}$	11.89 ± 0.21	P
CP-1291751	2.06	2.0253	...	3.47 ± 0.35	3.59	0.67	1.00	$11.24^{+0.23}_{-0.22}$	...	P
UV-155853	1.96	1.9816	247 ± 30	4.55 ± 0.46	3.62	0.85	1.00	$11.62^{+0.18}_{-0.17}$	11.60 ± 0.11	E
UV-171060	2.02	2.0995	...	1.73 ± 0.17	4.00	0.54	1.00	$11.48^{+0.16}_{-0.17}$	...	E
UV-230929	2.09	2.1679	252 ± 21	1.74 ± 0.17	3.01	0.73	1.00	$11.48^{+0.16}_{-0.15}$	11.23 ± 0.08	E
UV-239220	2.00	2.0057	...	5.35 ± 0.54	4.21	0.62	1.00	$11.57^{+0.20}_{-0.20}$	...	E
UV-773654	1.96	2.0328	...	3.77 ± 0.38	3.34	0.84	1.00	$11.59^{+0.19}_{-0.19}$	...	E
CP-1243752	2.01	2.0903	350 ± 53	2.85 ± 0.29	4.50	0.79	1.00	$11.79^{+0.17}_{-0.17}$	11.66 ± 0.14	E
CP-540713	1.98	2.0409	353 ± 97	1.65 ± 0.17	0.96	0.79	1.00	$11.26^{+0.22}_{-0.23}$	11.59 ± 0.24	E
UDS-19627	2.02	2.0389	318 ± 53	2.00 ± 0.20	3.32	0.51	1.00	$11.37^{+0.13}_{-0.10}$	11.48 ± 0.15	E

Column 1: Target ID, Column 2: Photometric redshift from Muzzin et al. (2013a), Column 3: Spectroscopic redshift (Section 2.4.1), Column 4: Stellar velocity dispersion measurement (Section 2.4.1), Column 5: Effective semi-major axis (Section 2.4.5), Column 6: Sérsic index (Sersic 1968), Column 7: Axis ratio $q = b/a$ (defined by the ratio between the semi minor and major axis), Column 8: Flux scaling used to estimate the corrected stellar mass, $\log_{10} M_{*,c}$ (Section 2.4.6), Column 9: Corrected stellar mass (Section 2.4.6), Column 10: Dynamical mass (Section 2.5.4), Column 11: Morphological classification (P:Peculiar, E:Elliptical) from Conselice et al. (2005). † Galaxies classified as Major Mergers in Section 2.4.6

[a] Double sources have similar photometric and spectroscopic redshift as well as the stellar velocity dispersion estimated from their composite spectrum

[b] Relative Flux Ratio = $F_i/(F_i + F_j)$

[c] Galaxies marked with (†) are classified as major mergers in Section 2.4.6

2.4.5 Galaxy structure and sizes

The 2-D stellar light distribution traced by *HST*/WFC3 H_{F160W} imaging are modeled with the χ^2-minimization fitting code *GALFIT* (Peng et al. 2002) in order to retrieve the structural parameters of our sample of MQGs. A first run of *SExtractor* (Bertin & Arnouts 1996) allows us to detect the objects in each field and to obtain an initial guess for the structural parameters. Postage stamp for each target is constructed such that it encloses an ellipse with a major axis 2.5 times the Kron radius obtained by *SExtractor*. The local sky level in each stamp is calculated using Galapagos (Barden et al. 2012). This sky level is passed to *GALFIT* and kept fixed during the fitting. For the WFC3 data, a combination of the TINYTIM[8]-simulated point spread function (PSF) and an empirical stacked star PSF are used. For the NICMOS data, an empirical stacked PSF are used.

Finally, *GALFIT* is run on each postage stamp, adopting a flexible Sérsic profile for every source (Sersic 1968)

$$\Sigma(R) = \Sigma_e \exp\left\{-\kappa_n \left[\left(\frac{R}{R_e}\right)^{1/n} - 1\right]\right\}. \tag{2.2}$$

The parameter R_e is the effective radius enclosing half of the flux from the model light profile, $\Sigma(R_e)$ is the surface brightness at the effective radius and n is the Sérsic index. The quantity κ_n is a function of the Sérsic index, which defines the global curvature of the light profile, and is obtained by solving the equation $\Gamma(2n) = 2\gamma(2n, \kappa_n)$, where Γ and γ are, respectively, the gamma function and the incomplete gamma function.

GALFIT is run several times to ensure that the solutions correspond to a global minimum in the minimization algorithm for each image, by varying the initial guesses of the total magnitude, effective radius and Sérsic index. The parameters are constrained so to avoid any unphysical solutions (effective radius > 0.2 pixels, $q > 0.1$, $0.5 < n < 8$). Initially, all targets are fit with n as a free parameter. In unstable cases where the maximum or minimum n are reached, the images fixing the Sérsic index at either $n = 1$ or $n = 4$ are re-fit, choosing the model providing the smallest χ^2 as the best-fit solution. These two choices represent realistic descriptions of an early-type galaxy dominated by either a disk or a bulge. Throughout the whole fitting procedure, neighboring objects are either modeled or masked, depending on their proximity to the main target. A 10% measurement uncertainty on the size is (van der Wel et al. 2008; Newman et al. 2012) shown to be a fair representation. This conservative error estimate is thus adopted. The semi-major axis, $R_{\rm e,maj}$, is adopted as the effective radius in the following sections. The best-fit parameters and their uncertainties are reported in Table 2.3.

In Figure 2.7, we present the rest-frame UV (I_{F814W}) and optical (H_{F160W}) images along with the *GALFIT* model and residual. The morphologies of these galaxies are classified in the H_{F160W} image according to Conselice et al. (2005) and they fall into the two categories for quiescent systems: Ellipticals (E) and Peculiars (P). When available, the spectroscopic observations are used

[8] http://www.stsci.edu/hst/observatory/focus/TinyTim

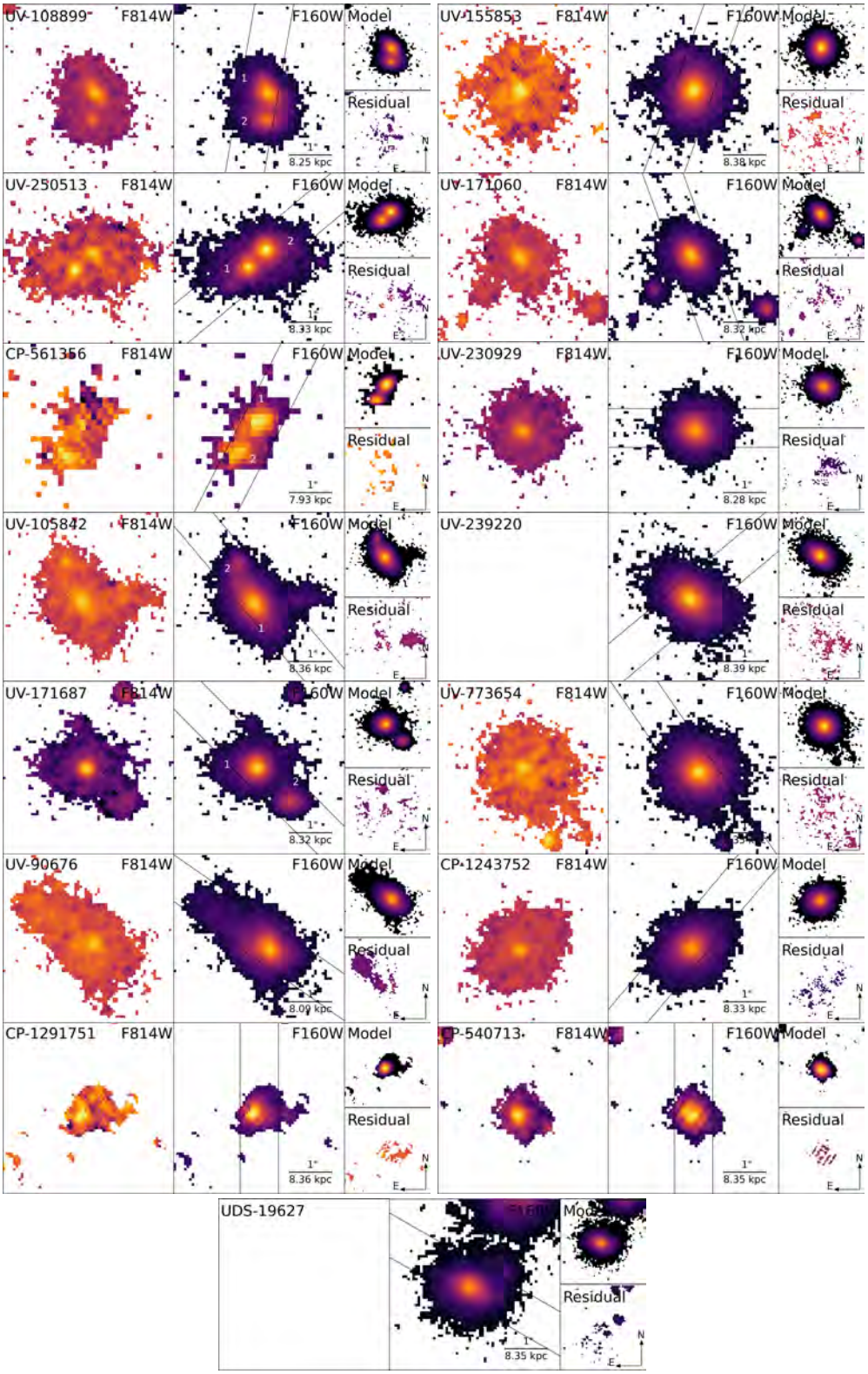

Figure 2.7: I_{F814W}, H_{F160W}, *GALFIT* model, and *GALFIT* residual for our sample of massive quiescent galaxies at $z > 2$ in $4x4$" cutouts. Pixels, with a 3σ confidence (w.r.t. background), are indicated with a logarithmic color scale to showcase the structure and morphology of the sample. H_{F160W} significant pixels are used as a mask for all the images. In the residual image, the pixels, one standard deviation above the background, are shown within this mask. The X-Shooter slit is overlaid at the orientation of the spectroscopic observations. A scale of $1\farcs0$ is shown in kpc for size reference.

to determine the distance in redshift space to objects that fall in the X-Shooter slit (see Section 2.4.2). The majority of sources turn out not to be associated with the central galaxy. $9/15$ galaxies are categorized as Elliptical galaxies while the remaining are categorized as Peculiar galaxies with major mergers (UV-108899, UV-250513, CP-561356), minor mergers (UV-105842, CP-1291751) and/or strong tidal/post-merger features (UV-105842, UV-90676). The galaxies UV-108899, UV-250513 and CP-561356 are confirmed as ongoing major mergers in the following section. The classifications and the morphological parameters are listed in Table 2.3.

2.4.6 Spectroscopic confirmation and stellar mass correction of ongoing major mergers

The RB color images, in Figure 2.2, reveal that three galaxies (UV-108899, UV-250513, CP-561356) appear to be double systems. The spectra, shown in the same figure, are the total extraction of the combined light from the two galaxies. These objects are within close proximity and the light in the reduced 2-D frames are blended to an unknown extent (due to limited seeing). At the expense of drastically decreasing the S/N, an attempt to separate the sources and determine if their individual redshift measurements can confirm their proximity are made.

For each system, the resolved 1-D *HST* H_{F160W} light profile (extracted parallel to the X-Shooter slit) is overlaid on top of the wavelength collapsed 2-D spectrum trace. A double Gaussian profile fit allowed us to gauge the amount of blending and to make a conservative extraction of each individual galaxy, minimizing cross-source contamination. In Figure 2.6, the individual extractions and the best-fit to the composite spectrum from Section 2.4.3 are shown. Because of the low S/N of the individual conservative flux extractions, the estimation of the velocity offset are refrained, since it would be dominated by large uncertainties. However, the galaxies are within close physical proximity due to the matching absorption lines shown in the figure and can be considered ongoing quiescent (dry) major-mergers. This confirmation is important as, in the following section, it can be used to correct their stellar masses, prior to presenting them in the mass-size plane (see Section 2.5.3). Spectroscopic confirmation allows us to deblend the composite stellar mass of each system using the H_{F160W} magnitude as a proxy for tracing the bulk of the stars in the galaxies. The *GALFIT* modeled H_{F160W} flux ratio supports the fact that these galaxies are major mergers with mass ratios of $1:1-3$. We used the flux ratio to correct the stellar masses as

$$M_{*,i} = M_{*,tot}\frac{F_i}{F_i + F_j} = M_{*,tot}R_{\rm Flux}, \tag{2.3}$$

where i and j refer to the two merging galaxies and F is the total flux from *GALFIT*. The corrected stellar masses ($M_{*,c}$) and the relative flux ratio scaling, $R_{\rm Flux}$, are listed in Table 2.3, with sources names matching the numbering in Figure 2.7. Following this correction, the galaxies still classify as MQGs with stellar masses, $\log_{10}(M_*/M_\odot) > 11$.

2.5 Results

2.5.1 Minimal progenitor bias

A major issue preventing us from deriving a consistent evolutionary picture connecting galaxy populations across time is the "progenitor bias" problem (e.g. van Dokkum & Franx 1996; Carollo et al. 2013). When comparing galaxies across time, the implicit assumption is that the high redshift sample contains all progenitors of the low redshift reference sample. However, the fraction of quenched galaxies has been found to grow over time (Buitrago et al. 2013) introducing an unknown bias when comparing samples of galaxies across different epochs.

One approach, that has been suggested to minimize the progenitor bias, is comparing the evolution of galaxies at fixed velocity dispersion (see e.g. Belli et al. 2014a). Archaeological studies (van der Wel et al. 2009; Graves et al. 2009; Bezanson et al. 2012) find evidence suggesting that the velocity dispersion in quiescent galaxies remains approximately unchanged across cosmic time ($z < 1.5$). In such a scenario the velocity dispersion must be weakly affected by the average merger history, which according to the numerical study by Hilz et al. (2012) occurs for minor merger-driven evolution. A detailed discussion on fixed velocity dispersion evolution is given in Belli et al. (2014a, 2017). Another way to minimize the progenitor bias has been to study galaxy populations at constant cumulative number density (CND) instead of fixed velocity dispersion or stellar mass (see e.g. Mundy et al. 2015). This approach are introduced in van Dokkum et al. (2010) and refined further in Behroozi et al. (2013); Leja et al. (2013). In Section 2.2.1, a sample of massive galaxies with central stellar population ages suggesting formation at $z > 2$ are introduced. This sample is volume limited and represents the most massive early-type systems observed in the local Universe. In order to draw a meaningful comparison, a subgroup of the most massive galaxies at $z = 0$ are selected and matched with the CND at $z = 2$. This will now be referred to as the "fixed" CND. This approach is based on the assumption that the rank of galaxies, within the stellar mass function, is not strongly affected across cosmic time. This occurs if the stellar mass continuously grows from $z = 2 - 0$, implying the availability of surrounding material to accrete (or events that trigger secondary SF, although this is not expected for the massive quiescent galaxies at $z > 2$) (Brammer et al. 2011; Behroozi et al. 2013; Muzzin et al. 2013b; Marchesini et al. 2014).

First, the CND of massive ($\log(M_*/M_\odot) > 11.2$) *UVJ* quiescent galaxies in the redshift range $1.9 < z < 2.5$ is estimated using the Muzzin et al. (2013a) catalog. The stellar-mass limit represents the lower limit on the standard deviation of the mean stellar mass from the sample of galaxies studied in this paper. Our sample is 22 % stellar mass complete using these selection criteria. We count 58 galaxies inside a comoving volume spanned by this redshift range giving a $n(\log(M_*/M_\odot) > 11.2) = 9.7 \times 10^{-6}\ Mpc^{-3}$.

The MASSIVE galaxy sample is trimmed starting from the most massive object of the survey and including progressively less massive systems until we reach the fixed CND of the massive

UVJ quiescent galaxies at $z \sim 2$. The final fixed CND-matched MASSIVE sample consists of the 25 most massive local elliptical galaxies with stellar masses of $\log(M_*/M_\odot) > 11.70$. The fixed CND-matched MASSIVE sample is referred to as "MASSIVE(n)" hereafter. The MASSIVE(n) sample is considered a minimal progenitor biased sample and used as our local reference sample in Section 2.5.2, 2.5.3, and 2.5.4.

The CND evolution suffers from large uncertainties from individual merger histories causing scatter in the mass rank which is the main uncertainty for the highest stellar masses (Behroozi et al. 2013; Torrey et al. 2017). In Torrey et al. (2017), they estimate the mass rank scatter for $\log_{10}(M_*/M_\odot) > 11$ in Illustris (Genel et al. 2014; Nelson et al. 2015) and find a CND mass rank scatter of a factor of 2 compared to the mean CND enclosing 80 % of the galaxy fraction from $z = 2$. In Behroozi et al. (2013), they find a similar uncertainty for the fixed CND evolution. The effect of the mass rank scatter on the fixed CND evolution is shown in Figure 2.8, 2.9, and 2.10 under the assumption that it is representative for our stellar mass selection.

As an alternative approach to the fixed CND matching, the probabilistic approach from Wellons & Torrey (2017) is used to estimate the CND at $z = 0$. In Figure 2.11, the results for both a fixed and probabilistic CND matching approach is shown. The choice of CND-matching method does not affect the qualitative results of this paper.

2.5.2 Kinematic evolution of massive quiescent galaxies from $z = 2$ to 0

In Figure 2.8, the stellar velocity dispersion-size plane which allows us to study the kinematic evolution of massive quiescent galaxies from $z = 2 - 0$, is presented. The ongoing major merger galaxies are included to show that their incorrect composite dispersion measurement increase the scatter if not properly accounted for. The mean velocity dispersion of the sample studied in this paper is 289 ± 58 km/s (without major mergers). This is consistent with previous $z > 2$ massive quiescent galaxy literature (see studies shown in Figure 2.8) with a mean dispersion of 272 ± 31 km/s. Our velocity dispersion and size measurements (including other structural parameters) for CP-1242752 (indicated by blue square in Figure 2.8) are consistent with previously published values (van de Sande et al. 2013; Belli et al. 2014b; Kriek et al. 2016; Belli et al. 2017). Comparing the median dispersion of our study to that of the local MASSIVE(n) sample, a shallow or no kinematic evolution from $z = 2 - 0$ is found. In Figure 2.8, significant effective size evolution consistent with earlier findings are observed (Newman et al. 2012; van der Wel et al. 2014).

Half of the morphologies of compact massive galaxies at $z \sim 2$ have been suggested to be disk-dominated (van der Wel et al. 2011). So far only one spatially resolved study of a rotating disk quiescent galaxy at this epoch has been discovered (Toft et al. 2017; Newman et al. 2018). The line of sight measured velocity broadening of the absorption lines could be a combination of both rotation and dispersion in the presence of a disk-dominated system (see an analytical prescription in Belli et al. 2017). Care must therefore be taken when comparing $z > 2$ spatially

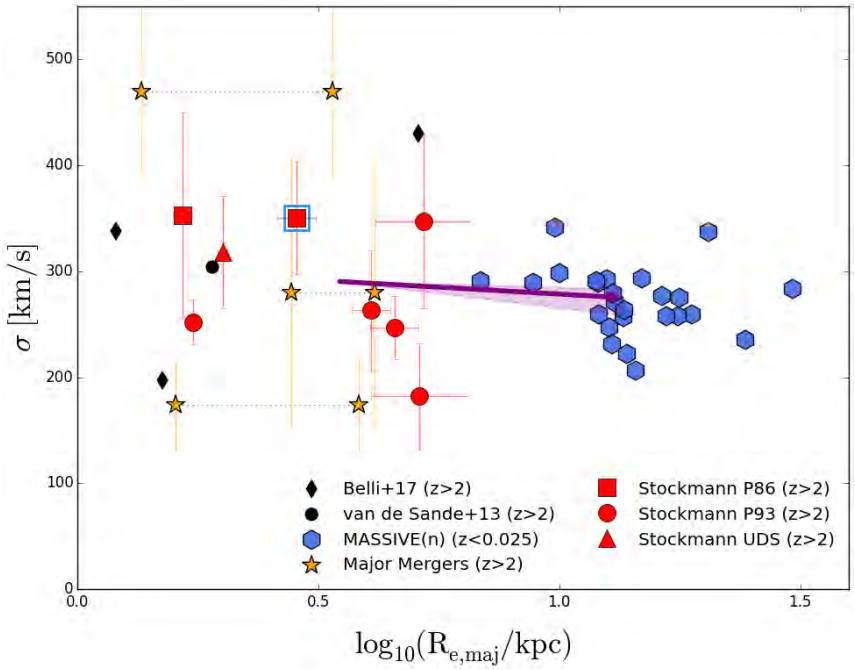

Figure 2.8: The velocity dispersions are plotted with effective radii for three samples; 1) Our sample (red symbols like Figure 2.1), 2) massive, $\log_{10}(M_*/M_\odot) > 11$, other quiescent galaxies at $z_{\rm spec} > 2$ (van de Sande et al. 2013; Belli et al. 2017), 3) the MASSIVE(n) sample in blue hexagons. The composite dispersion measurements of the major-merger galaxies are shown in orange stars connecting their individual size measurements with a horizontal dotted line. The blue square indicates our source CP-1243752 (recently published in van de Sande et al. 2013; Kriek et al. 2016; Belli et al. 2017). The purple arrow shows the median evolution between our study and the MASSIVE(n) sample. The uncertainty from the mass rank scatter on the fixed CND is shown in purple shading. The median evolution between the our study and the MASSIVE(n) sample show evidence for shallow or no kinematic evolution from $z = 2$ to 0.

unresolved dispersion with resolved local measurements. Wuyts et al. (2011) shows that the stellar light distribution of galaxies, measured by the Sérsic index, traces well the $\log(\mathrm{SFR}) - \log(\mathrm{M}_*)$ relation, separating disk and spheroidal galaxies by $n = 2.5$ at $z < 1.5$. Under the assumption that this is valid at $z = 2$, we classify our galaxies by Sérsic index and find that 92% of our galaxies have spheroidal ($n > 2.5$) morphologies (when excluding the ongoing major mergers). If Sérsic index $n > 2.5$ is a good tracer of dispersion-dominated systems at $z > 2$, it suggests that our sample of galaxy dispersion measurements are not strongly contaminated by rotation. A recent study by Veale et al. (2018) presents the spatially resolved velocity dispersion measurements for the MASSIVE Survey sample. Here, $\log_{10}(M_*/M_\odot) > 11.7$ galaxies (similar to our stellar mass cut of the MASSIVE(n) sample) all have velocity dispersions in the range $200 < \sigma < 350$ km/s at all radii ($< 15 - 30$ kpc). This rules out the possibility that the shallow dispersion evolution comparison is driven by spatial resolution. A comparison to the fixed CND-matched MASSIVE(n) sample establish that the dispersion remains nearly unchanged.

Negligible median dispersion evolution of our MQGs across the last 10 billion years ($z = 2 - 0$) is found in Figure 2.8. In the absence of spatially resolved spectroscopy, we make use of the morphological classification which suggest that our kinematics are unlikely to be strongly

contaminated by rotation. Studying the evolution of galaxies at fixed dispersion has been suggested as a method to minimise progenitor bias (e.g. Belli et al. 2014b).

2.5.3 Stellar mass-size plane for massive quiescent galaxies

In Figure 2.9, the stellar mass-size plane ($\log_{10}M_* - R_{\rm e,maj}$) is presented which allows us to study the structural and stellar mass evolution of massive quiescent galaxies since $z \sim 2$. The three ongoing major-merger galaxies with resolved sizes of the individual galaxies (Section 2.4.5) and their flux corrected stellar masses (Section 2.4.6) are shown in the figure. The post-merger stellar masses and sizes of these are predicted using the argument of virialization from Bezanson et al. (2009). The resulting position of post-merger galaxies is consistent with the average locus of the most massive ($\log_{10}(M_*/M_\odot) > 11.5$) individual galaxies in our sample, showing that a way to form the most massive quiescent galaxies in our sample could be major quiescent-to-quiescent dry galaxy mergers (Naab et al. 2006).

A best fit relation to the galaxies in this study, including the major merger separated galaxies, reveal a shallower slope than what are found in van der Wel et al. (2014) $z = 2.25$ mass-size relation, but in a better agreement with Mowla et al. (2019). The best fit parameters, using a similar parametrization ($r/\mathrm{kpc} = \mathrm{A}(\mathrm{M}_*/(5 \cdot 10^{10}))^{\alpha}$), are $\log(A) = 0.19$ and $\alpha = 0.42$. The stellar mass for CP-1243752 (blue square in Figure 2.9) is consistent within 1σ standard deviation with van de Sande et al. (2013) and Belli et al. (2017) and within 1.1σ for the stellar mass published in Kriek et al. (2016).

The distribution of our sample shows that $z > 2$ MQGs are ~ 2 times more compact than objects with the same stellar mass in the local Universe (Shen et al. 2003), which is a well-established result in previous works (van de Sande et al. 2013; Belli et al. 2017). The median stellar mass and size for our (MASSIVE(n)) sample $\log(M_*/M_\odot) = 11.48$ (11.77) and $R_{\rm e,maj}/\mathrm{kpc} = 3.42$ (13.55) show that a doubling (~ 0.3 dex) in stellar mass and a factor of 4 in size evolution are required to bring the two samples into qualitative agreement. Using the method from Bezanson et al. (2009) for predicting stellar mass and size growth, minor and major merger tracks are shown in the mass-size plane. The median mass-size evolution between our $z > 2$ MQGs and the local MASSIVE(n) sample could be explained by minor merger-predicted size and stellar mass growth. The tracks start at the median size and stellar mass of our sample (only red symbols). The qualitative conclusions remain the same when using a mean instead of a median or changing the choice of reference (with/without the major merger galaxies). The median logarithmic mass-size slope is $\alpha = 1.78^{+0.37}_{-0.29}$ ($r \propto M_*^{\alpha}$). The uncertainties are determined based on the CND mass rank scatter shown as the purple shaded area in Figure 2.9. This confirms the suggestion that minor mergers ($\alpha = 2$), compared to major mergers ($\alpha = 1$), are the preferred evolutionary path in the mass-size plane.

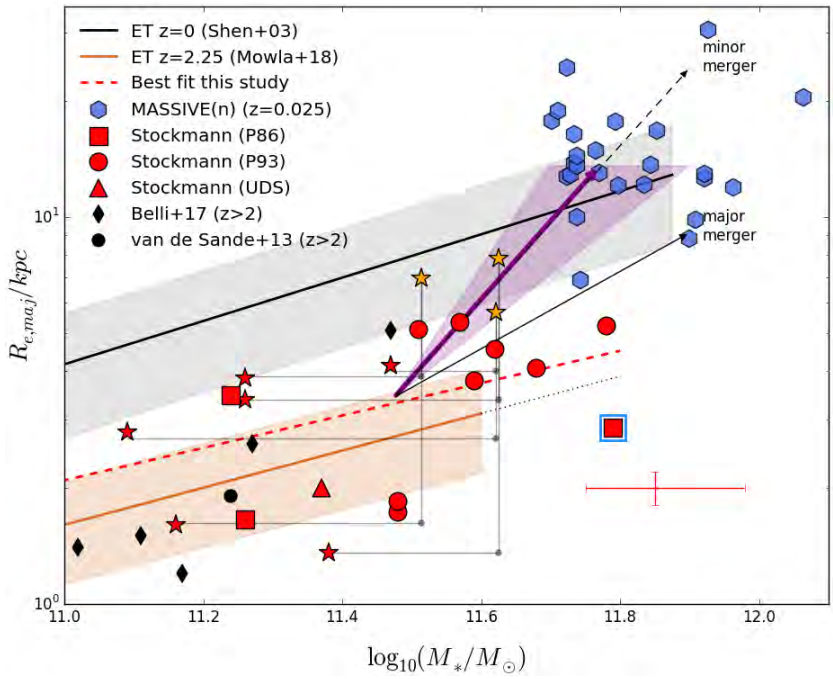

Figure 2.9: The stellar mass-size plane for massive, $\log_{10}(M_*/M_\odot) > 11.0$, quiescent galaxies: our sample (red symbols), other massive quiescent galaxies at $z > 2$ (black symbols, van de Sande et al. 2013; Belli et al. 2017) and the MASSIVE(n) sample (blue hexagons). The representative error bar of our sample is shown in red. The source CP-1243752 is indicated with a blue square. The ongoing major merger-corrected stellar masses (red stars) are connected (gray lines) to their post-merger positions (orange stars), following the Bezanson et al. (2009) prescription. The minor (dashed) and major (solid) merger-predicted evolutions from Bezanson et al. (2009) are shown with black arrows. The best fit relations at $z = 0$ (Shen et al. 2003) and 2.25 (Mowla et al. 2019), with their 1σ uncertainty, are shown in black and brown, respectively. The best-fit relation to the galaxies of this study is shown in dashed red. The purple arrow shows the median evolution between our study and the MASSIVE(n) sample. The shaded purple area represents the uncertainty on the median of the MASSIVE(n) sample when the mass rank scatter from Behroozi et al. (2013) is taken into account. The median mass-size evolution of MQGs from $z = 2 - 0$ can be explained primarily by minor mergers.

In line with earlier studies (van de Sande et al. 2013; Belli et al. 2017; van der Wel et al. 2014; Mowla et al. 2019), we find that our sample of $z > 2$ MQGs is compact in the stellar mass-size plane and further suggests that minor merger-driven size evolution (Bluck et al. 2012; Newman et al. 2012; Hilz et al. 2012, 2013; Oogi & Habe 2013; Fagioli et al. 2016) is preferred when comparing to the fixed CND-matched MASSIVE(n) sample.

2.5.4 Stellar-dynamical mass plane for massive quiescent galaxies

In Figure 2.10, the dynamical-to-stellar mass relation for massive quiescent galaxies is plotted in order to study the interplay between the stellar and total (dynamical) mass potential over time. The dynamical mass derived from the Jeans equation (Jeans 1902) for symmetrical systems is as follows

$$M(r) = \beta \frac{R_{\mathrm{e,maj}} \sigma^2}{G}. \tag{2.4}$$

Here, $R_{\mathrm{e,maj}}$ is the effective semi-major axis, σ is the stellar velocity dispersion, G is the gravitational constant and β is a parameter incorporating the full complexity of a collisionless systems

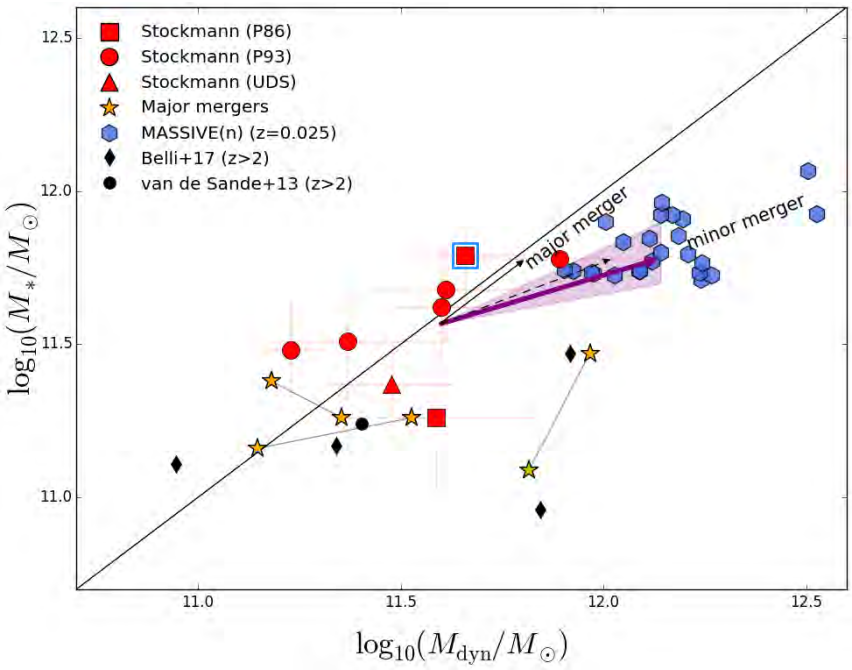

Figure 2.10: The dynamical-stellar mass plane for this study (red squares: *P86*, circles: *P93*, triangle: UDS19627), other $z_{\rm spec} > 2$ massive quiescent galaxies (in black symbols van de Sande et al. 2013; Belli et al. 2017), and the MASSIVE(n) sample (blue hexagons). The purple arrow connects the median relation between this study and the MASSIVE(n) sample. The purple shaded area represents the uncertainty on the median values of the MASSIVE(n) sample from the CND mass rank scatter. The solid black line is the $M_* = M_{\rm dyn}$ relation. The dashed/solid black arrow represents the predicted constant dispersion stellar-to-dynamical mass evolution for minor/major mergers (Bezanson et al. 2009). The blue square indicates the source CP-1243752 (previously published in van de Sande et al. 2013; Kriek et al. 2016; Belli et al. 2017). The calculated dynamical-to-stellar mass ratio doubles from $z = 2$ to 0 when comparing to the fixed CND-matched MASSIVE(n) sample.

with radial dependent parameters of density, dispersion, and velocity anisotropy. Following Cappellari et al. (2006a), $\beta(n) = 8.87 - 0.831n + 0.0241n^2$ is adopted where n is the Sérsic index (Sersic 1968). The representation of β is a good approximation for symmetric systems such as an elliptical galaxy that is well represented by a de Vaucouleurs profile. Taylor et al. (2010a) and Cappellari et al. (2013) show that using such a parametrization of β yields dynamical masses in better agreement with the stellar masses when the sizes, are estimated using a 2-dimensional Sérsic fitting method, rather than a fixed value of β. The galaxies of this study are consistent with the stellar-to-dynamical mass ratio, $M_*/M_{\rm dyn} < 1$, within the large uncertainties. A ratio > 1 is referred to as a non-physical (forbidden) region where the total mass is smaller than the mass of the stars. The galaxy, UV-230929, is located in this region at 1.1σ standard deviation from the $M_*/M_{\rm dyn} = 1$ relation. Unfortunately, our large uncertainties prohibit trustworthy estimates of the total dust+gas mass for our sample. In Belli et al. (2017), it is suggested that dispersion dominated systems with $n > 2.5$ lie closer to the $M_*/M_{\rm dyn} = 1$ relation at $z \sim 2$. Compared to previous $z > 2$ massive quiescent galaxy studies (see legend in Figure 2.10), our sample occupies a similar dynamical mass range but has larger stellar masses. This is further discussed in Section 2.6.2. The dynamical mass for CP-1243752 (indicated by a blue square) is consistent with the

previous measurements in van de Sande et al. (2013) and Belli et al. (2017).

A comparison between our study with the MASSIVE(n) sample is made to learn about the fixed CND evolution in the dynamical-stellar mass plane. The median evolution in Figure 2.10 illustrates that the dynamical mass evolves $2\times$ faster than stellar mass within the effective radii. This means that the galaxies evolve such that the $M_*/M_{\rm dyn}$ ratio decreases from $z = 2$ to 0. The minor and major merger evolution are shown for constant velocity dispersion evolution ($\Delta r \propto M_*^{\alpha}$), with $\alpha = 1$ for major merger and 2 for minor merger evolution. This is motivated by the shallow/constant dispersion evolution found in Section 2.5.2, when also comparing to the MASSIVE(n) sample. The median evolution from $z = 2$ to present day prefers the minor merger predicted evolution when comparing our study to the MASSIVE(n) sample in the dynamical-stellar mass plane.

The median evolution from our study to the MASSIVE(n) sample at present day, in the dynamical-stellar mass plane, is consistent with minor merger evolution that is similar to what is found in Figure 2.8 and 2.9.

2.6 Discussion

The structural and kinematic evolution for massive galaxies from $z = 2$ to present is explored by assuming that the galaxies, in this study, are the progenitors of the MASSIVE(n) sample. Such a claim has been motivated by a fixed CND-matching between the two samples of galaxies. This suggests that these galaxies undergo significant size growth together with shallow velocity dispersion evolution, driving up the dynamical-to-stellar mass ratio from $z = 2$ to 0. The results are interpreted using idealized and cosmological simulations. Furthermore, the origin of the dust heating, observed in the MIR and FIR emission, is discussed. Finally, the caveats are presented.

2.6.1 Minor-merger size evolution at constant dispersion

In Figure 2.9, a slope of $\alpha = 1.78^{+0.37}_{-0.29}$ is found for the mass-size evolution of our MQG from $z = 2$ to 0. Such an evolution can be interpreted using the analytical framework from Bezanson et al. (2009) and Naab et al. (2009) which find that minor merger-driven growth is needed to produce a mass-size slope of $\alpha = 2$. An extended numerical treatment from Hilz et al. (2012) finds that when including the effect of escaping particles (a process arising from virialization following merger interaction), they recover a steeper mass-size slope ($\alpha = 2.4$) alongside a constant dispersion evolution for minor merger-driven growth. Such a scenario could explain the observed size growth and shallow dispersion evolution observed. The scenario presented in Hilz et al. (2012) occurs for two-component (stellar+halo) systems when they undergo 1:10 minor merger evolution. They reproduce the structural evolution found in Bezanson et al. (2009) and Naab et al. (2009) when simulating minor-merger evolution of stellar-only systems. This

suggests that the growth of the dark matter halo is an important ingredient necessary to cause the shallow dispersion evolution together with the expected size growth evolution we find in this study. Moreover, Hilz et al. (2012) shows that major mergers increase the dispersion and size proportional to the stellar mass. This is not what is found when comparing the size and dispersion evolution with the MASSIVE(n) sample (see Figure 2.8 and 2.9). In the minor merger scenario, the velocity dispersion would be maintained in the inner region of the galaxy, as additional stellar mass is accreted in the outer parts from tidally stripped satellite systems. Over time, this would change the stellar light distribution on the outskirts of the galaxy, causing a continuous growth of the half-light radius (van Dokkum et al. 2010; Hill et al. 2017).

In UV-105842, we may be observing a direct example of the minor merger-driven size increase. A small satellite system within close (spectroscopically confirmed) proximity of the central galaxy is found. Based on the flux-ratio estimated from the *GALFIT* modeling we estimate a stellar mass ratio of $1{:}12^{+6}_{-3}$ for this minor merger, consistent with the average 1:16 ratio estimated by Newman et al. (2012). To double its stellar mass (as suggested by the median ~ 0.3 dex increase derived for our sample), the galaxy would need to go through ~ 12 such minor mergers between z=2 and 0. Other minor merger stellar mass ratios of 1:5, 1:10 and 1:20 suggested by Hilz et al. (2013) and Bédorf & Portegies Zwart (2013), would correspond to 5, 10, and 20 minor mergers between z=2 and 0 for a similar stellar mass increase. In Man et al. (2016a) issues related to the translation of the H-band flux ratio to a stellar mass ratio (e.g. due to M/L ratio variation in galaxies), directly affecting the above argument, are discussed.

Many observational (Bluck et al. 2012; McLure et al. 2013; Fagioli et al. 2016; Matharu et al. 2019; Zahid et al. 2019) and numerical (Naab et al. 2009; Oser et al. 2012; Oogi & Habe 2013; Tapia et al. 2014; Naab et al. 2014; Remus et al. 2017) studies find that minor mergers could be a dominant process for the size growth of massive galaxies, but it may not be able to explain the the full size evolution (Cimatti et al. 2012; Newman et al. 2012). Feedback processes have been shown to also affect the size growth (e.g. Lackner et al. 2012; Hirschmann et al. 2013). Specifically AGN feedback is shown, by modern simulations, to be necessary to reproduce the observed size evolution (see Dubois et al. 2013; Choi et al. 2018).

2.6.2 Stellar-to-dynamical mass evolution

We found that the dynamical-to-stellar mass ratio shown in Figure 2.10 increases by a factor of two within MQGs from $z = 2$ to 0. This could be attributed to either IMF changes of the stellar population (Cappellari et al. 2012) affecting the stellar mass estimates or an increase in the dark matter fraction within the effective half-light radius.

Numerical simulations find that minor merger-driven evolution alters the distribution of stars over time from a core to a core-envelope system by accretion of particles in the outskirts of the galaxy (Hopkins et al. 2009; Hilz et al. 2012, 2013; Frigo & Balcells 2017; Lagos et al. 2018). A

consequence of this is that the central dispersion remains constant while the half-light radius grows, encompassing a larger part of the dark matter halo and effectively increasing the dark matter fraction over time (Hilz et al. 2012).

A mass-size evolution similar to what we find is, according to Hilz et al. (2013), caused by a massive dark matter halo that drives the accretion of dry (collisionless) minor mergers at large radii through tidal stripping. This inside-out growth increases the effective half-mass radius to encompass dark matter dominated regions which might explain the increase of the dynamical-to-stellar mass fraction within the half-light radius that we observe. Care must be taken when interpreting the observations in terms of idealized numerical simulations. However, Remus et al. (2017) also find that the central dark matter fraction increases with decreasing redshift when comparing different cosmological simulations. Furthermore, observational evidence for inside-out growth in massive galaxies is presented in Szomoru et al. (2012).

In Figure 2.10, we find that our sample is consistent with the dynamical-to-stellar mass ratio of one suggesting low dark matter fractions at $z \sim 2$. For a stellar mass increase of 0.3 dex (similar to our median evolution), Hilz et al. (2012) predict a dark matter fraction increase of ~ 70 % within the effective radius. If we assume that the mass of the galaxy consists only of dark matter and stars, we can estimate the dark matter mass fractions ($M_{DM}/M_{\rm dyn} = 1 - M_*/M_{\rm dyn}$), from the dynamical-to-stellar median ratio at $z = 2$ and 0, to be 7^{+24}_{-7} % and 56 ± 8 %, respectively. This suggests an increase of the dark matter fraction within the effective radius of $17 - 64$ %. Note, however, that this increase cannot purely be associated with the dark matter from the minor mergers as the growing half-light radius similarly encompasses more of the central dark matter halo and also contributes to this increase.

According to Remus et al. (2017), the mass growth of massive galaxies can be explained by two stages: 1) High redshift in situ mass growth resulting in a dense stellar component in the center of the potential where the dark matter fraction is low, 2) dry merger events dominate the mass growth at lower redshift (with major mergers being rare) resulting in the build-up of a stellar envelope increasing the half-light radius and thus the dark matter fraction (similar to the interpretation above).

2.6.3 Dust heating in massive quiescent galaxies at $z > 2$

The 24 μm SFR limit, used to restrict the stellar population models, results in specific SFRs for our galaxies of $\log_{10}({\rm sSFR/yr}) < -10$. Nonetheless, stronger limits on the specific SFR can be obtained if the source of dust heating is not caused by recent star formation. In Section 2.4.4.3, the information from optical nebular emission and mid-IR is combined to set stringent limits on the SFR of our sample (see also Figure 2.5). This information reveals that our sample lies 1.5 dex below $z = 2$ the star formation - stellar mass relation of (Speagle et al. 2014) (extrapolated to $\log_{10}(M_\odot/M_*) \sim 11.5$).

Low-luminosity AGN is shown to be common in massive, $\log_{10}(M_*/M_\odot) > 11$, quiescent galaxies at $z < 1.5$, through excess radio emission in stacked samples (Man et al. 2016b; Gobat et al. 2018). Six galaxies, in our sample, have direct radio detections; three of them with matching mid-IR detections (see Table 2.2). This could be evidence in line with the results from Olsen et al. (2013) who find a high fraction of AGN in massive quiescent galaxies at $1.5 < z < 2.5$ using X-ray stacking. Low luminosity AGN activity has, in Schawinski et al. (2009); Best & Heckman (2012), been associated with the suppression of SF which is an important effect in maintaining galaxies quiescent. Low levels of dust heating have also been associated with evolved stellar populations as a significant source to emit at wavelengths beyond $> 160\ \mu m$ (Salim et al. 2009; Bendo et al. 2012; Fumagalli et al. 2014; Utomo et al. 2014). However, with no detections in the Herschel/PACS bands, we cannot rule this scenario out. In the case where AGN are indeed the dominant dust heating source in the galaxies, we can expect that the $24\ \mu m$ flux does not arise from residual SF. This is consistent with Whitaker et al. (2017) that find no strongly obscured SF in massive quiescent galaxies at $z > 2$. Assuming the $24\ \mu m$ emission is not due to obscured starformation, we find a specific SFR, $\log_{10}(\mathrm{sSFR/yr}) < -11$, based purely on the optical emission limits/detections. The MIR-to-radio emission of the sample will, in a future publication, be investigated in detail (Cortzen et al. in prep).

2.6.4 Caveats

The main limitations of the results are here presented in bullet points:

- Overestimated stellar masses would lead to a shallower mass-size evolution and dynamical-to-stellar mass ratio evolution. Nonetheless, substantially overestimated stellar masses are ruled out by our dynamical masses being in agreement with previous kinematic studies of massive quiescent galaxies at $z > 2$ (Toft et al. 2012; van de Sande et al. 2013; Bezanson et al. 2013; Belli et al. 2014b, 2017).

- If rotation is significant in massive quiescent galaxies at $z > 2$, the measured velocity dispersion, depending on the inclination, could have an unknown contribution from rotation resulting in heightened dispersion measurements. On the other hand, dispersion measurements from face-on rotation-dominated galaxies could result in low values. This would further drive the dynamical mass artificially down. Such issues should be addressed by spatially resolved spectroscopy where the V_{rot}/σ can be estimated.

- Previous studies (Mancini et al. 2010) have suggested that sizes might be underestimated due to non-detection of low luminosity profile wings. However, ultra-deep imaging out to many effective radii does not find that this is the case (Szomoru et al. 2010, 2011).

- Dynamical-to-stellar mass evolution is sensitive to the determination of $\beta(n)$. The prescription from Cappellari et al. (2006a) is used, yet, this relation is determined from local galaxies and is assumed to be representative for dynamical systems at $z \sim 2$. When comparing with the MASSIVE(n) sample, we assume a Sérsic index of $n = 4$, to be a fair representation of a spheroidal system. When changing the choice of $\beta = 2 - 6$ for the MASSIVE(n) sample, the conclusion that the ratio must evolve from $z = 2 - 0$ remains.

- The sample is 60 % mass complete for the massive ($\log_{10}(M_*/M_\odot) > 11$) and K-band brightest ($K < 20.5$) UVJ quiescent galaxies at $1.9 < z < 2.5$. This selection depends strongly on the performance of the photometric redshift estimate. In Figure 2.4, we show that this works well for our sample using the catalog from Muzzin et al. (2013a). This suggests that the sample studied in this paper is representative of the selection we presented in Section 2.2. However, the photometry is used to select red systems and, consequently, introduce a selection bias towards mergers between red galaxies. An unresolved merger of a quiescent galaxy with a star-forming galaxy would produce a resulting bluer system that might be excluded from the selection.

2.7 Summary and conclusion

We examined the largest sample of massive quiescent galaxies observed to date at $z > 2$ with deep X-Shooter spectroscopy and HST/WFC3 imaging. We extend previous searches for very massive quiescent galaxies at $z > 2$ to the K-band brightest *UVJ* quiescent galaxies in COSMOS (Muzzin et al. 2013a), constructing a sample of 15 MQGs. Full SED modeling of the photometry and spectroscopy confirms the sample to be ~ 1.5 Gyr old, massive, $\log_{10}(M_*/M_\odot) > 11$, quiescent galaxies. 3 out of 15 galaxies are confirmed as ongoing major merger using both imaging and spectroscopy. In total, 40 % of the sample show evidence of mergers (minor or major) or other disturbed morphologies in HST/WFC3 H_{F160W} imaging, suggestive of ongoing morphological transformation. The morphological information is used to correct the stellar masses prior to comparing the stellar populations, kinematics and structure/morphology of the galaxies to the MASSIVE(n) sample. We list below the main conclusions of the paper:

- We find that our galaxies lie $1 - 1.5$ dex below the extrapolation at the high stellar mass end of the SFR main-sequence (Speagle et al. 2014) at $z = 2$ and can be considered quiescent with low specific SFR, $\log_{10}(\mathrm{sSFR/yr}) < -10.5$. These limits are based on optical emission line and MIR emission limits and detections. $1/3$ of the galaxies are detected in the MIR which could be caused by residual SF. However, more than half of our sample (60 % of the MIR detections) have radio emission detected at 1.4 or 3 GHz. This radio emission is likely

associated with AGN activity, a proposed heating mechanism leading to quenching and/or the maintenance of quiescence in massive galaxies.

- We find indirect evidence pointing to our velocity dispersion measurements to be minimally contaminated by rotation. Our systems also have a Sérsic index $n > 2.5$ (see Section 2.5.2). A direct comparison between our study and the MASSIVE(n) sample, shows evidence for shallow or no velocity dispersion evolution from $z = 2 - 0$.

- Our sample is compact, in line with previous studies at $z \sim 2$ (van der Wel et al. 2014; Mowla et al. 2019). We find that the median mass-size evolution ($\Delta r \propto \Delta M_*^{\alpha}$) compared to the MASSIVE(n) sample is best described by $\alpha = 1.78^{+0.37}_{-0.29}$. This is consistent with both the simple kinematic predictions of minor merger driven size evolution from Bezanson et al. (2009) and the more extensive numerical treatment from Hilz et al. (2012).

- We find that our sample of $z > 2$ MQGs is consistent with a dynamical-to-stellar mass ratio $M_*/M_{\rm dyn} < 1$ but that the shallow dispersion and significant size increase lead to an increasing dynamical-to-stellar mass ratio, doubling from $z = 2$ to the present day. Such an effect is shown to be reproduced for an increasing dark matter fraction from $z = 2 - 0$, within the effective radius of the galaxy (Hilz et al. 2012).

In this paper the largest sample of MQGs at $z > 2$ with kinematic and structural observations, found via the mass-size and dynamical-stellar mass plane, is presented. A fixed CND-matching suggests that our sample of galaxies are the progenitors of the most massive and oldest elliptical galaxies in the local Universe, thus connecting 10 billion years of evolution. These galaxies show a broad range of disturbed morphologies, confirming that mergers play a significant role in their morphological transformation and evolution to $z = 0$. In a companion paper, the relationship between the size and dispersion will be explored by studying the Fundamental Plane at $z \sim 2$ and its consequent evolution to the present-day Universe (Stockmann+19b in prep).

Acknowledgements

We thank Martin Sparre for his useful discussions related to X-Shooter data. M.S. extend gratitude to Nina Voit for her ultimate support and patience in the becoming of this work. Based on data products from observations made with ESO Telescopes at the La Silla Paranal Observatories under ESO programmes ID 086.B-0955(A) and 093.B-0627(A) and on data products produced by TERAPIX and the Cambridge Astronomy survey Unit on behalf of the UltraVISTA consortium. M.S. and S.T. acknowledge support from the European Research Council (ERC) Consolidator Grant funding scheme (project ConTExt, grant number 648179). Based on observations made with the NASA/ESA Hubble Space Telescope, obtained from the data archive at the Space Telescope Science Institute. STScI is operated by the Association of Universities for Research in Astronomy, Inc. under NASA contract NAS 5-26555. Support for this work was provided by NASA through grant number HST-GO-14721.002 from the Space Telescope Science Institute, which is operated by AURA, Inc., under NASA contract NAS 5-26555. This research made use of Astropy (version 1.1.1),[9] a community-developed core Python package for Astronomy (Astropy Collaboration et al. 2013, 2018). This research made use of APLpy, an open-source plotting package for Python (Robitaille & Bressert 2012). I.J. is supported by the Gemini Observatory, which is operated by the Association of Universities for Research in Astronomy, Inc., on behalf of the international Gemini partnership of Argentina, Brazil, Canada, Chile, the Republic of Korea, and the United States of America. GEM acknowledges support from the Villum Fonden research grant 13160 "Gas to stars, stars to dust: tracing star formation across cosmic time", the Cosmic Dawn Center is funded by the Danish National Research Foundation. A.M. is supported by the Dunlap Fellowship through an endowment established by the David Dunlap family and the University of Toronto. R.D. gratefully acknowledges support from the Chilean Centro de Excelencia en Astrofísica y Tecnologías Afines (CATA) BASAL grant AFB-170002. M. H. acknowledges financial support from the Carlsberg Foundation via a Semper Ardens grant (CF15-0384). Y.P. acknowledges NSFC Grant No. 11773001 and National Key R&D Program of China Grant 2016YFA0400702.

[9] http://www.astropy.org

Appendices

A Further details on the reduction of the images

A.1 PSF & astrometry

The H_{F160W} images from our program and the ancillary COSMOS $F814W$ images employed in this work do not share the same World Coordinate System (WCS). We need to guarantee that the astrometry is common and accurate in both bands. Therefore, we chose to align the images to the COSMOS ACS $F814W$ image as the reference frame, which is registered to the fundamental astrometric frame of the COSMOS field, ensuring an absolute astrometric accuracy of 0.″05–0.″1 or better. Following Gómez-Guijarro et al. (2018), we use `TweakReg` along with SExtractor (Bertin & Arnouts 1996) catalogs of the two bands with the $F814W$ catalog and frame as references to register the images. After this, the images in both bands are resampled to a common grid and a pixel scale of 0.″06 pix^{-1} using SWarp (Bertin et al. 2002). In addition, the spatial resolution of the two *HST* bands is also different. Following Gómez-Guijarro et al. (2018), we degrade the $F814W$ to the resolution of the $F160W$ data (0.″18 FWHM). We calculate the kernel to match the ACS $F814W$ to the PSF in the $F160W$ images employing the task `PSFMATCH` in IRAF, including a cosine bell function tapered in frequency space to avoid introducing artifacts in the resulting kernel from the highest frequencies. Then, we convolve this kernel to the $F814W$ image to achieve a common spatial resolution.

A.2 Modeling of foreground and background sources

Based on the spatially offset emission in the 2-D X-Shooter spectra, we determine if candidate sources are within close proximity to the central galaxy. In Figure 2.7 the central sources along their spatially offset sources is shown. UV-171687 shows offset Hα and [NII] emission arising from a south-western source that we establish to be a foreground galaxy at $z = 1.51$. We find another foreground galaxy north-east of UV-171060 at $z = 1.37$ based on assuming that the single emission line detection is Hα. North-east of UV-155853 we find a background galaxy at $z = 2.36$ (best visible in the Galfit modeling residuals of Figure 2.7) determined from the [OIII] doublet at $4959, 5007$ Å. For UV-105842 we find two spatially offset source, 1) $\sim 3''$ north-east and 2) $\sim 1''$ north-east. Source 1) is a foreground galaxy at $z = 0.44$ based on the detected strong O[III] doublet at $4959, 5007$ Å and Hα emission. For source 2) we find the [OII] doublet at $3726.2, 3728.9$ Å, O[III] doublet at $4959, 5007$ Å, and Hα corresponding to a redshift $z = 2.0124$. The latter redshift corresponds to a velocity offset of 2130 ± 120 km/s (uncertainty is calculated based on the spread of the individual redshift measurements) suggesting that it is not gravitationally bound to the central galaxy. Another option could be an offset AGN with high peculiar velocity following a merger.

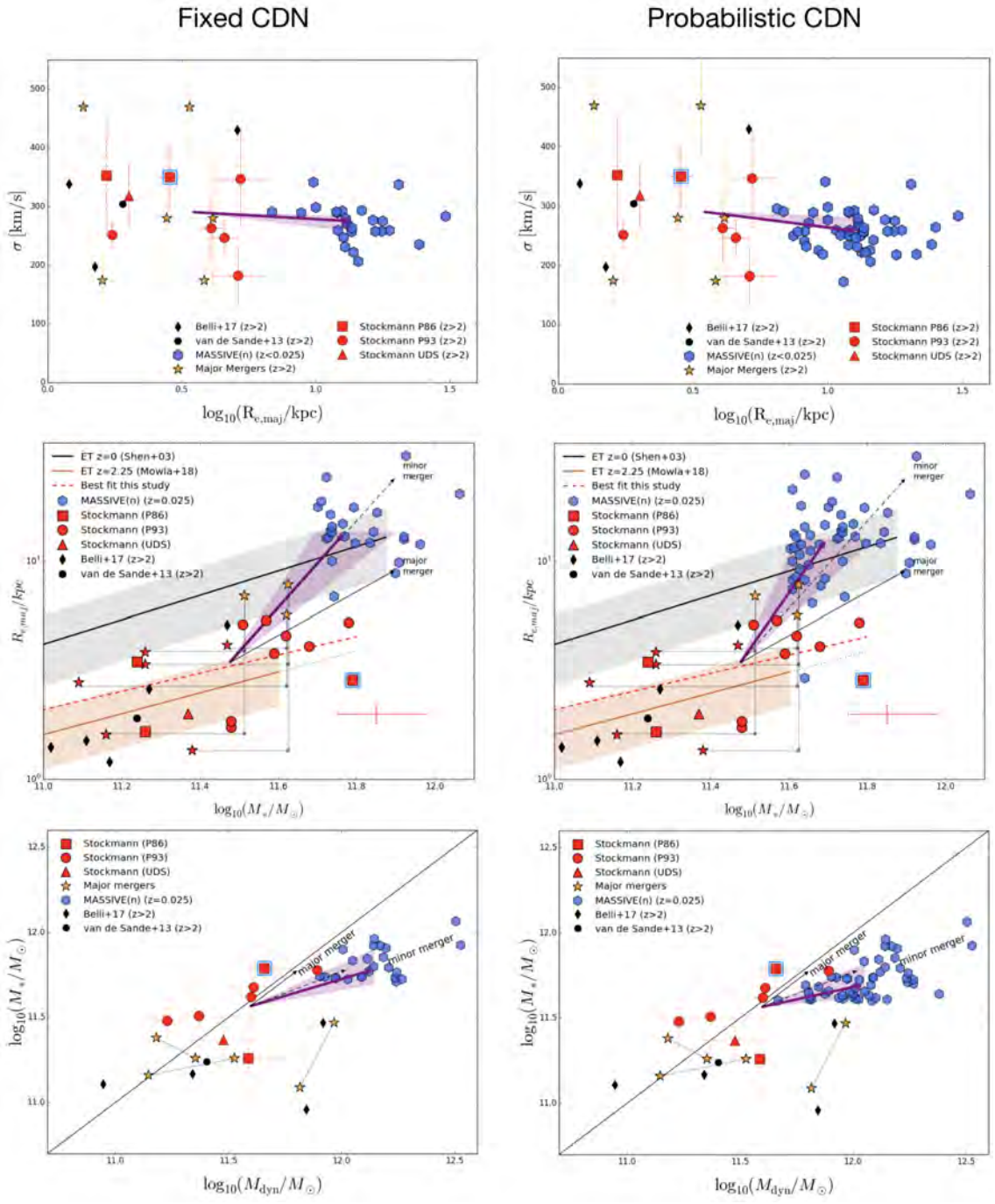

Figure 2.11: The figures from Section 3 are shown with the fixed and probabilistic (Wellons & Torrey 2017) CND-match to the MASSIVE Survey. For each of these methods our qualitative conclusions remain.

B Details on the emission line fitting

For UV-108899, we find that when fitting a double Gaussian profile to [OII] ($3726 + 3729$ Å) fixed to the redshift of the central galaxy, gives the most conservative (highest) flux estimate. We try fitting with a single profile while using a free redshift parameter but recover high χ^2 solutions. We list this conservative flux estimate, corresponding to a SFR $= 6 \pm 4$ $M_\odot$/yr (Kennicutt 1998), in Table. 2.2.

For UV-239220, we detect excess emission in the region of Hα and the [NII] ($6548 + 6583$ Å) doublet. With a fixed ratio between the [NII] doublet, we try three types of triple Gaussian profile models (free redshift+dispersion limit of 250 km/s, free redshift+dispersion limit of 1000 km/s, and fixed redshift+dispersion limit of 1000 km/s) that all result in $\chi^2 > 2.4$ with no preferred solution. If we assign all of the flux in the excess to Hα we obtain a conservative Kennicutt (1998) SFR upper limit of ~ 30 $M_\odot$/yr ($\log(sSFR) < -10$ [yr^{-1}]) consistent with the FIR and rest-frame optical upper limits from Section 2.4.4.1. This confirms that the galaxy has low specific star formation consistent with its selection.

C Details on modeling of the velocity dispersion

C.1 Statistical and systematic uncertainties

To estimate the statistical error we measure the spread of the velocity dispersion distribution obtained from running pPXF on a 1000 data realizations. The data realizations are made by perturbing the pPXF best fit model with the pipeline estimated error spectrum, by linearly drawing values from a Gaussian with a mean of zero and spread of the initial errors. The X-Shooter pipeline-estimated noise map is subjected to a wavelength dependent correlation of the pixels. We take this effect into account by scaling our noise spectrum to a reduced $\chi^2_{red} = 1$ (assuming the errors are Gaussian). We follow the method used in Toft et al. (2017) and fit a 2nd order polynomial to a 50 pixel running reduced χ^2 that we use to make a correction noise map, $\sigma_{\chi^2_{corr}} = \sigma_{\chi^2_{original}} \sqrt{\chi^2_{fit}}$.
We estimate the systematic error by testing how the dispersion is changing with the correction polynomial and implemented wavelength range. We construct a grid of correction polynomials up to 24th order of both additive and multiplicative polynomials, where we find an average of 20 % variation from the fiducial dispersion, except for UV-232920, UV-773654, UV-171060, and CP-1291751. When varying the start wavelength range ($[\lambda_{start}, \lambda_{end}]$) within the interval $[3750 - 4050, 5950]$ and the end wavelength within the interval $[3750, 4050 - 5950]$, we find that overall the dispersions are stable. In a few cases, the velocity dispersion increases well above the median dispersion (with varying wavelengths) with $50 - 100$ % when excluding the higher order Balmer and Ca H+K lines, highlighting their importance. When including the end wavelength

$\lambda > 4500$ we find more stable dispersion measurements, not surprising as otherwise only half of the spectrum is included. The low S/N cases have more unstable dispersion values when excluding wavelength areas, highlighting the importance of understanding the systematic uncertainties. We sum up the wavelength and polynomial test by confirming that our fiducial velocity dispersions are robust (except for UV-232920, UV-773654, UV-171060, and CP-1291751). The systematic error is primarily due to template mismatch and as a result, we estimate the systematic error from the minimum and maximum values of the dispersion when using the full wavelength range and varying the additive and multiplicative correction polynomials, $\sigma_{sys} = 2/3 \cdot (\sigma_{max} - \sigma_{min})/2$. This method is subjected to catastrophic outliers, and prior to the systematic error estimate, we exclude dispersion values more than 5σ outside of a Gaussian mean. We find that the systematic errors are on the order of the statistical uncertainties.

C.1.1 Additional tests

We measure the dispersion while excluding a window of 1600 km/s along the wavelength direction in steps of 5 Å, to test whether the measured dispersion is dominated by specific lines. We find that the fiducial dispersion is very stable against excluding individual lines, and did not find a consistent decrease in the velocity dispersion similar to previous studies when excluding the Hβ line (van de Sande et al. 2013; Toft et al. 2017). We allow pPXF to construct a linear combination of templates from the stellar library of BC03 with a Chabrier IMF and solar metallicity and find similar redshifts and velocity dispersions as our fiducial values which are reassuring.

3

Stellar and Dynamical Evolution of Massive Quiescent Galaxies

This chapter contains the following article:

"A Fundamental Plane Study of Massive Quiescent Galaxies at $z \sim 2$"

In preparation for submission to *The Astrophysical Journal*

M. Stockmann, I. Jørgensen, S. Toft, C. J. Conselice, A. Faisst, B. Margalef-Bentabol, A. Gallazzi, S. Zibetti, M. Hirschmann, C. D. Lagos, J. Zabl, G. B. Brammer, C. Gomez-Guijarro, & F. M. Valentino

We investigate the evolution of galaxy structure and kinematics by studying the Fundamental Plane (FP) and mass-to-light ratio (M/L) scaling relations for a sample of 8 massive, $\log_{10}(\mathrm{M}_*/\mathrm{M}_\odot) > 11$, quiescent galaxies at $z > 2$. We establish a FP (r_e, σ_e, I_e) using a larger sample of 19 quiescent galaxies at $1.5 < z < 2.5$ from the Cosmic Evolution Survey with H_{F160W} rest-frame optical sizes and velocity dispersions. Contrary to lower-z cluster studies, we show that our sample of galaxies cannot evolve passively to the local Coma cluster relation alone and must undergo significant structural evolution to mimic the sizes of local massive galaxies. The evolution of the FP and M/L scaling relations, from $z = 2$ to present-day, are consistent with passive aging of the stellar population and size growth by minor mergers into the most massive galaxies in the Coma cluster as well as a cumulative number density matched sample of massive elliptical galaxies from the MASSIVE Survey. In the case that the structural growth can be fully attributed to minor mergers, the evolution of the scaling relations favors minor merger with quiescent stellar populations.

1 Introduction

The most massive local elliptical galaxies, believed to be the latest stage of galaxy evolution, have been shown to form the majority of their stars rapidly, in the densest environments at $z > 2 - 3$ (e.g. Blakeslee et al. 2003; Thomas et al. 2005). Understanding the formation and evolution of these systems is a major question, and one way to address this is to look for progenitors in the early universe to see how their properties have evolved. Recently a population of massive, $\log(M_*/M_\odot) > 11$, quiescent galaxies have been located at $z > 2$ (Daddi et al. 2004; Kriek et al. 2009b; Toft et al. 2012; Belli et al. 2017), which allows us to observe the evolution of their properties. It is clear that these early massive galaxies contain extremely compact sizes (Daddi et al. 2005; Trujillo et al. 2006, 2007; Buitrago et al. 2008; van Dokkum et al. 2008; Conselice et al. 2011; Szomoru et al. 2012), 3-5 times smaller than present-day most massive elliptical galaxies, and are bluer and more recently formed (e.g., Stockmann et al. 2019).

Rapid size evolution has been inferred from the observed evolution of field early-type galaxies across time (Newman et al. 2012; van der Wel et al. 2014; Faisst et al. 2017; Mowla et al. 2019; Morishita et al. 2019). Toft et al. (2014) proposed an evolutionary sequence of massive galaxies where the most massive elliptical galaxies, from the present-day Universe, were formed in violent star-bursts, that later quench possibly via AGN to become the compact quiescent galaxies at $z > 2$ suggested to undergo rapid size evolution (see also Habouzit et al. 2019). Simulations have shown dry mergers to be an efficient process in making galaxies larger (e.g. Hopkins et al. 2009; Naab et al. 2009; Bezanson et al. 2009; Hilz et al. 2012, 2013; Remus et al. 2017; Lagos et al. 2018).

Scaling relations between different properties of galaxies and how these evolve through time can give us significant information about how galaxies are assembled over cosmic time. The massive elliptical galaxies were found to follow an empirical relation known as the Fundamental Plane (FP, Djorgovski & Davis 1987; Dressler et al. 1987). It is important to determine the FP of a sample of possible discovered progenitors at $z > 2$ and their connection with present-day massive elliptical galaxies. The FPs zero point evolution, complementary to the M/L ratio (Faber et al. 1987), has made this a preferred tool in studying the structural and luminosity evolution of early-type galaxies across time (e.g. Bender et al. 1992a; Jørgensen et al. 1996; Jørgensen 1999; Treu et al. 2005; van der Wel et al. 2005; Cappellari et al. 2006a; Jørgensen et al. 2006; van der Marel & van Dokkum 2007; Saglia et al. 2010; Jørgensen & Chiboucas 2013). At $z < 1$, the FP zero point offset have been explained by purely passive (without structural) evolution (e.g. Jørgensen et al. 2006; Jørgensen & Chiboucas 2013). However, this is not the case at $z > 2$ where the red and dead galaxies are compact and must undergo significant size evolution to mimic the sizes of present-day galaxies. The FP has been established in cluster and field galaxies out to a redshift of $z < 1.8$ in clusters (Prichard et al. 2017) and $z < 2$ in the field (Bezanson et al. 2013; van de Sande et al. 2014), respectively. Galaxies in clusters have been observed to be larger than field

galaxies at the same redshift (Lani et al. 2013; Strazzullo et al. 2013; Delaye et al. 2014) suggesting accelerated evolution in dense environments (for evidence against this see Newman et al. 2014).

Spectroscopic observations, required to measure the velocity dispersion, is time-expensive and only the most massive systems have been studied in large cosmological fields like CANDELS and COSMOS due to their rarity. We present in this paper the largest FP study at $z > 2$ using a sample of field massive quiescent galaxies (MQGs) introduced in Stockmann et al. (2019) (hereafter *S19a*). *S19a* shows shallow velocity dispersion evolution and significant size growth between $z = 2$ and 0. In this paper, we explore whether this size growth, alongside the passive evolution of the stellar population, can account for the observed evolution of massive galaxies in the scaling relations from $z = 2$ to present-day.

In Section 2, the $z > 2$ MQGs sample from *S19a* together with a complementary quiescent galaxy sample is presented alongside two local samples from the Coma cluster and the MASSIVE Survey. We present the M/L and FP scaling relations in Section 3.1 and 3.2, respectively. The predicted evolution of the size, velocity dispersion, passive aging, and luminosity increase due to minor merger driven growth are covered in Section 3.3. Finally, our results are interpreted and discussed in Section 4, following a summary of the main conclusions in Section 5.

Throughout the text, magnitudes are quoted in the AB system (Oke & Gunn 1983; Fukugita et al. 1996) and the following cosmological parameters, $\Omega_m = 0.3$, $\Omega_\Lambda = 0.7$, with $H_0 = 70$ km/s/Mpc are used. All stellar masses are presented using the Chabrier (2003) Initial Mass Function (IMF).

Table 3.1: Sample Summary

Target ID	RA	Dec	$z_{\rm spec}$	$\log{\rm Age/yr}$	$\log{\rm M_*/M_\odot}$	$\log{\rm M_{dyn}/M_\odot}$	$r_{e,circ}$ [kpc]	σ_e [km/s]	$\log\langle{\rm I}\rangle_{\rm e,B}$
UV-105842	150.26265	2.0177791	2.0195	$9.19^{+0.26}_{-0.33}$	$11.68^{+0.16}_{-0.17}$	11.47 ± 0.19	2.91 ± 0.29	263 ± 57	4.40
UV-171687	149.88702	2.3506956	2.1020	$9.13^{+0.28}_{-0.32}$	$11.51^{+0.18}_{-0.19}$	11.31 ± 0.24	4.49 ± 0.45	182 ± 50	3.99
UV-90676	150.48750	2.2700379	2.4781	$9.09^{+0.29}_{-0.29}$	$11.78^{+0.17}_{-0.18}$	11.78 ± 0.21	4.08 ± 0.41	347 ± 82	4.46
UV-155853	149.55630	2.1672480	1.9816	$9.23^{+0.24}_{-0.33}$	$11.62^{+0.18}_{-0.17}$	11.57 ± 0.11	4.20 ± 0.42	247 ± 30	3.96
UV-230929	150.20842	2.7721019	2.1679	$9.10^{+0.28}_{-0.28}$	$11.48^{+0.16}_{-0.16}$	11.16 ± 0.07	1.48 ± 0.15	252 ± 21	5.11
CP-1243752	150.07394	2.2979755	2.0903	$9.23^{+0.24}_{-0.32}$	$11.79^{+0.17}_{-0.17}$	11.61 ± 0.13	2.54 ± 0.25	350 ± 53	4.59
CP-540713	150.32512	1.8185385	2.0409	$9.16^{+0.27}_{-0.32}$	$11.26^{+0.22}_{-0.23}$	11.53 ± 0.24	1.46 ± 0.15	353 ± 97	4.66
UDS-19627[a]	34.57125	-5.3607778	2.0389	$9.08^{+0.11}_{-0.10}$	$11.37^{+0.13}_{-0.10}$	11.33 ± 0.14	1.43 ± 0.14	318 ± 53	5.20

Column 1: Target ID from *S19a*; Column 2: Right Ascension in degrees (J2000); Column 3: Declination in degrees (J2000); Column 4: Spectroscopic redshift; Column 5: Mass-weighted Age; Column 6: Stellar mass; Column 7: Circularised dynamical mass calculated using $\beta(n_{sersic})$ from Cappellari et al. (2006b); Column 8: Circularised effective radius; Column 9: Stellar velocity dispersion in km/s; Column 10: Average surface brightness within $r_{e,circ}$ in $L_{B,\odot}/pc^2$ (see Appendix D).

[a]The spectroscopic redshift, age, stellar mass, and velocity dispersion are from Toft et al. (2012) and the *HST*/WFC3 $H_{\rm F160W}$ size are from *S19a*.

2 Data

2.1 A sample of massive quiescent galaxies at $z > 2$

In *S19a*, we presented a sample of MQGs at $z > 2$ studied with X-Shooter (D'Odorico et al. 2006; Vernet et al. 2011) and *HST* H_{F160W} that are crucial to obtain both rest-frame optical stellar velocity dispersions and effective sizes. The sample is selected from the 2 square degree COSMOS field (Scoville et al. 2007), using multi-waveband photometric fits (Muzzin et al. 2013a). In summary, the sample is K-band bright massive ($\log_{10}(\mathrm{M}_*/\mathrm{M}_\odot) > 11$) UVJ quiescent galaxies at $z > 2$. We adopt, 8 of the total 15 galaxies from *S19a*, with robust velocity dispersion measurements essential to studying them in the scaling relations.

In Table 3.1, the mass-weighted age, stellar mass, velocity dispersions, and sizes for these 8 galaxies are listed. For details on these, we refer to *S19a*. Contrary to S19a, we compute the dynamical masses in this paper by using the circularized sizes ($r_{e,circ} = \sqrt{ba}$) to make them consistent with the circularized dynamical masses used in the study of scaling relations of local clusters (e.g. Jørgensen & Chiboucas 2013). We have verified that the qualitative results from *S19a* remain when using circularized dynamical masses and sizes. Following local studies (e.g. Jørgensen 1999), we adopt the Bessel B-band luminosity, estimated in our case from the rest-frame Bessel B-band fluxes obtained from the COSMOS photometry (Laigle et al. 2016) using the photometric redshift code EAZY (Brammer et al. 2008)[1]. The luminosity and average effective surface brightness are estimated using the method outlined in Appendix D. Hereafter, the dynamical mass-to-light ratio in the Bessel B-band is referred to as M/L.

The 8 galaxies have a mean age of $\sim$ 1.5 Gyr and similar stellar mass, size and velocity dispersion range to the full 15 galaxy parent sample from *S19a*.

2.2 Complementary sample of quiescent galaxies at $1.5 < z < 2.5$

In addition to the galaxies from *S19a*, we adopt a sample of $1.5 < z < 2.5$ quiescent galaxies from Belli et al. (2017). We choose 11 out of 24 galaxies with velocity dispersions, that have available COSMOS photometry in Laigle et al. (2016) to ensure consistent measurements to our sample. Out of the 11 galaxies, 7 are at $z < 2$ and 4 at $z > 2$.

Similar to *S19a*, the sizes were derived from Sérsic profile fits to the rest-frame optical *HST*/WFC3 H_{F160W} images using *GALFIT*. The effective circularized radius is adopted. The velocity dispersions are derived from rest-frame optical MOSFIRE spectra using pPXF to fit BC03 stellar population models qualitative similar to *S19a*. The dynamical masses are converted from the semi-major axis to the circularized radius using the axis ratio. As in *S19a*, the dynamical mass is estimated using the method from Cappellari et al. (2006a). The two $z \sim 2$ samples, presented in

[1] https://github.com/gbrammer/eazy-photoz

Table 3.2: Fundamental Plane and M/L Scaling Relations

Sample	Relation	N_{gal}	rms
Coma[a]	$\log r_e = (1.30 \pm 0.08)\ \log\sigma - (0.82 \pm 0.03)\ \log\langle I\rangle_{e,\mathrm{B}} - 0.443$	105	0.09
QGs at $z \sim 2$[b]	$\log r_e = (0.46 \pm 0.18)\ \log\sigma - (0.46 \pm 0.07)\ \log\langle I\rangle_{e,\mathrm{B}} + 1.275$	19	0.15
Coma[a]	$\log M/L = (0.24 \pm 0.03)\ \log M_{\mathrm{dyn}} - 1.754$	105	0.12
QGs at $z \sim 2$[b]	$\log M/L = (0.51 \pm 0.15)\ \log M_{\mathrm{dyn}} - 6.393$	19	0.26
Coma[a]	$\log M/L = (1.07 \pm 0.12)\ \log\sigma - 1.560$	105	0.11
QGs at $z \sim 2$[b]	$\log M/L = (1.09 \pm 0.41)\ \log\sigma - 3.236$	19	0.28

Column 1: Sample; Column 2: Fitting method; Column 3: Scaling relations; Column 4: Number of galaxies included in fit; Column 5: rms scatter along the y direction of the scaling relation.

[a]Fits are from Jørgensen et al. (2019) Table 4.

[b]Samples from *S19a* and *B17* in the range $1.5 < z < 2.5$ (see Section 2)

this study, satisfy the UVJ quiescent galaxy selection. Together they allow for a larger dynamical mass range, $10.5 < \log_{10}(\mathrm{M_{dyn}}/\mathrm{M_\odot}) < 11.9$, and redshift, $1.5 < z < 2.5$, corresponding to a cosmological timespan of ~ 1.7 Gyr. The galaxies introduced here will be referred to as *B17*.

2.3 The MASSIVE Survey

The original volume-limited MASSIVE Survey sample is selected as the most massive and K-band brightest early-type galaxies within 108 Mpc of the northern hemisphere (Ma et al. 2014). Here, we use the 25 most massive, $\log_{10}(\mathrm{M_*}/\mathrm{M_\odot}) > 11.7$, MASSIVE galaxies (hereafter MASSIVE(n) sample), selected at fixed cumulative number density (CND) as our massive $z \sim 2$ sample as described in S19a. The cumulative number density of the $z \sim 2$ sample is estimated from the massive, $\log_{10}(\mathrm{M_*}/\mathrm{M_\odot}) > 11.2$, UVJ quiescent galaxies at $1.9 < z < 2.5$ in the Muzzin et al. (2013a) catalog. The results in *S19a* are shown to be robust against the choice of CND method (fixed and probabilistic, Wellons & Torrey (2017)), as well as the mass-rank scatter. A thorough discussion of the assumptions and uncertainties are covered in *S19a* Section 5.1.

The luminosity and average effective surface brightness for 17/25 galaxies are obtained with the SDSS DR14 catalog photometry (Blanton et al. 2017) by cross-matching the MASSIVE(n) sample using the SDSS SkyServer[2]. The modelMag photometry in the *u, g, r, i, z* bands is extracted in line with Jørgensen & Chiboucas (2013) and converted to rest-frame Bessel B-band magnitude using the EAZY code, similar to the high redshift samples in this study. The effective surface brightness is calculated from the apparent magnitude using the methods covered in Appendix D from Equation 3.7 - 3.8. Instead of estimating the luminosity distance from the redshift, these galaxies are close enough that peculiar velocities have a significant impact on their distance measurement. We, therefore, use the distance measurement from Ma et al. (2014), who correct for this effect. The 17 galaxy subsample is referred to as MASSIVE($\mathrm{n_{17}}$).

[2]http://skyserver.sdss.org/dr14/en/tools/crossid/crossid.aspx

The optical NASA–Sloan Atlas effective sizes, derived from 2-dimensional Sérsic fits (Sersic 1968) ($n = 2 - 6$), are adopted from Ma et al. (2014). For galaxies where these are not available, we use the infrared sizes measured by single Sérsic $r^{1/4}$ profile fits to 2MASS images, which we then convert to optical effective radii using equation (4) in Ma et al. (2014). The sizes are circularized using the axis ratio recovered from a cross-match using Vizier[3]. The average luminosity weighted dispersion within the effective radius is adopted (Veale et al. 2018). The dynamical masses are estimated using the method in *S19a* (with the prescription from Cappellari et al. 2006b) using $n = 4$ and the circularized effective sizes. The stellar mass, size and velocity dispersion between the MASSIVE(n) and MASSIVE(n_{17}) samples are compared in Appendix Figure 3.3. The MASSIVE(n_{17}) are uniformly sampled in the structural and kinematic parameter space and, therefore, we do not expect a selection bias introduced for part of the sample with available photometry. MASSIVE(n_{17}) is representative of the parent sample and is 68 % complete.

2.4 Coma cluster

As local reference cluster we use Coma/Abell 1656 with 152 spectroscopically confirmed members (based on the catalog from Godwin et al. (1983)) with $g'_{rf} \leq 16.1$ mag from SDSS DR14 (Blanton et al. 2017) photometry published in Jørgensen et al. (2018). The velocity dispersion measurements from the same paper are derived from high S/N (~ 60 Å^{-1}) spectra using the recipe presented in Jørgensen et al. (2017). The SDSS DR14 photometry is used to derive circularized effective radii and mean surface brightnesses (Jørgensen et al. 2019). Both data sets are calibrated to the *Legacy data* (Jørgensen 1999; Jørgensen & Chiboucas 2013) to provide a trustworthy low redshift reference cluster.

3 Results

3.1 Dynamical mass-to-light ratio, $M_{\rm dyn}/L_B$

In Figure 3.1, the M/L ratio with dynamical mass and velocity dispersion are shown allowing us to study the relations between the stellar population and the dynamics of massive quiescent galaxies and their evolution from $z = 2$ to 0.

Compared to the local Coma and MASSIVE(n_{17}) galaxies, the high redshift samples (*S19a* and *B17*) have lower M/L as expected for brighter more recently quenched and less dynamically massive systems. The majority of the galaxies from *S19a* have, already at $z = 2$, dynamical masses similar to the $\sim 10\%$ most massive galaxies in the Coma cluster. The MASSIVE(n_{17}) sample has dynamical masses similar to the 2 % most dynamical massive Coma galaxies that also have amongst the highest velocity dispersion. The combined samples of *S19a* and *B17* are fit by

[3] http://vizier.cfa.harvard.edu/

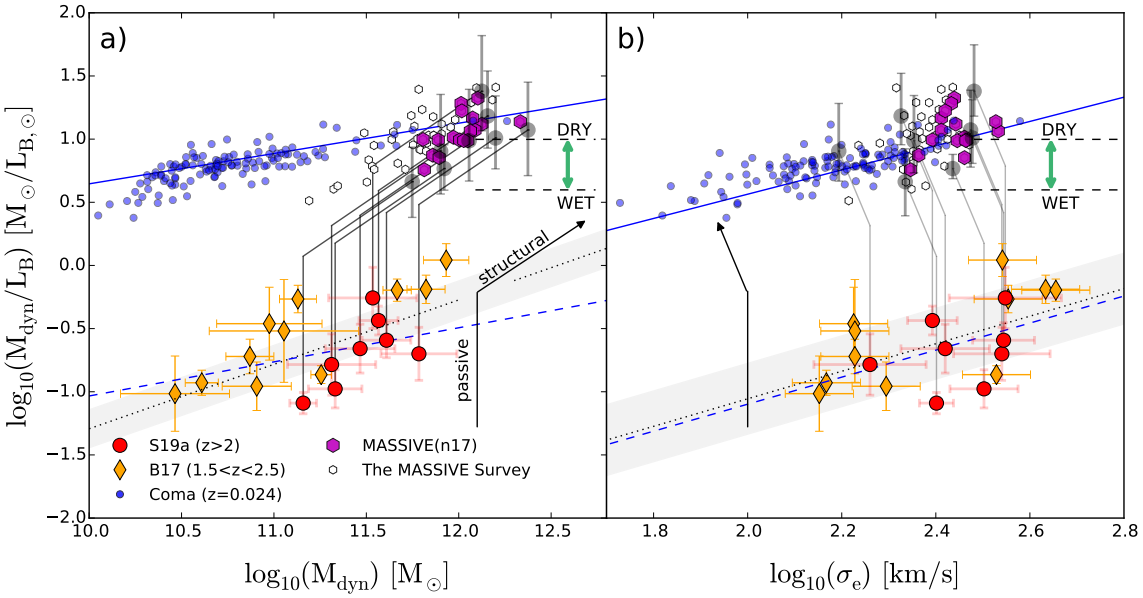

Figure 3.1: M/L ratio with dynamical mass (a) and velocity dispersion (b) are shown for the *S19a* MQGs $z > 2$ (red symbols) and 11 COSMOS quiescent galaxies at $1.5 < z < 2.5$ from *B17* (orange symbols). The Coma galaxies ($z = 0.0231$, blue symbols) are shown together with the best-fit relation (blue line) from Jørgensen et al. (2019). The MASSIVE Survey galaxies with available rest-frame B-band photometry (all hexagons) and the CND-matched MASSIVE(n_{17}) sample (purple hexagons) are shown. The best-fit (sloped black dotted line) and rms (gray shading) of the combined high redshift samples (*S19a* and *B17*) are shown together with the Coma best-fit relation offset to the median M/L at $z \sim 2$ (dashed blue). The predicted position at $z = 0$ following passive (vertical) and structural (sloped) evolution are shown by gray symbols. Their error bars are estimated from the combined uncertainty from observables (r_e, σ_e) and passive evolution modeling. The green arrow represents the M/L ratio change for dry or wet minor merger-driven structural evolution (see Section 3.3.2). The MQGs from *S19a* is consistent with evolving via both passive and dry minor merger structural evolution into the local most massive Coma galaxies and the CND-matched MASSIVE(n_{17}) sample.

minimizing the least-squares in the y-direction while the uncertainty on the slopes is estimated using a bootstrap method. A relation for the combined highest redshift sample is established, while this was not possible using *19a* alone. The fits are shown in Figure 3.1, together with the associated root mean square (rms) from the regression, and listed in Table 3.2. In both cases, we find best-fit slopes, for the combined high redshift sample, to be consistent with the local Coma relation. It is possible that the observed scatter, $2 - 3\times$ larger compared to the Coma relation is driven by the large velocity dispersion uncertainties. Larger samples, with improved velocity dispersion errors, can determine if the increasing slope observed at $z \sim 1$ is also present at $z > 2$ (van der Wel et al. 2005; Jørgensen et al. 2006; Jørgensen & Chiboucas 2013).

3.2 The Fundamental Plane

The FP is spanned by the effective size, r_e, stellar velocity dispersion, σ_e, and average effective surface brightness, $\langle I \rangle_{e,\mathrm{B}}$. Its edge-on and face-on orientations are defined as

$$\log_{10} r_e = \alpha \log_{10} \sigma_e + \beta \log_{10} \langle I \rangle_{e,\mathrm{B}} + \gamma \tag{3.1}$$

and

$$\begin{aligned}(2.22 \log_{10} r_e + \beta \log_{10} \langle I \rangle_{e,\mathrm{B}} + \alpha \log_{10} \sigma_e)/2.7 \\ = (\alpha \log_{10} \langle I \rangle_{e,\mathrm{B}} - \beta \log_{10} \sigma_e)/1.54,\end{aligned} \tag{3.2}$$

respectively. The best-fit Coma relation slopes ($\alpha = 1.30 \pm 0.08$, $\beta = -0.82 \pm 0.03$) and zero point ($\gamma = -0.443$) in the rest-frame B-band are adopted as our local reference orientation of the plane (Jørgensen et al. 2006, see also Table 3.2).

3.2.1 The Fundamental Plane at $z \sim 2$

In Figure 3.2, the FP edge-on and face-on projections, as described in Equation 3.1 and 3.2, are shown to examine how $z \sim 2$ massive quiescent galaxies populate and evolve in this plane. In the edge-on FP, the dominating errors from the velocity dispersion are shown on the y-axis (neglecting the magnitude uncertainty). For the face-on plane, the errors are calculated similarly to the approximation used in Jørgensen et al. (2006). The COSMOS quiescent galaxies from *S19a* and *B17* are both found below the Coma edge-on FP and above the face-on orientation. These galaxies have compact sizes and younger stellar populations (due to their high redshift and more recent quenching), effectively increasing their mean effective surface brightness.

An edge-on FP cannot be established using the *S19a* sample alone. However, when fitting the *S19a* and *B17* samples together a FP is in place at $1.5 < z < 2.5$ (hereafter referred to as $\mathrm{FP}_{z\sim2}$). The FP is fitted by using the least-squares method, minimizing the least-squares in the y-direction, with uncertainty from bootstrapping (see Table 3.2). In van de Sande et al. (2014), a FP was established for a similar redshift range ($1.5 < z < 2.5$), however, in our study, the sample of $z > 2$ galaxies are extended by a factor of three, robustly confirming the existence of a plane at $1.5 < z < 2.5$. For reference, the edge-on FP is shown using the $\mathrm{FP}_{z\sim2}$ best-fit coefficients in Figure 3.4. The scatter of the edge-on $\mathrm{FP}_{z\sim2}$ ($\mathrm{rms} = 0.15$) is $\sim 2\times$ larger than the intrinsic scatter of the Coma cluster FP. The FP coefficients are not well constrained at $z \sim 2$ and the scatter could again be driven by the large uncertainty of the velocity dispersion rather than the intrinsic properties. Despite this fact, our scatter at $z \sim 2$ matches the predicted evolution of the FP scatter based on a study of $0.2 < z < 1.2$ field early-type galaxies (Treu et al. 2005).

A $\mathrm{FP}_{z\sim2}$ is established with the massive quiescent galaxies suggesting that they were a relatively homogeneous population already in this epoch. They are found to be well below the local Coma relation and must undergo significant evolution from $z = 2$ to present-day.

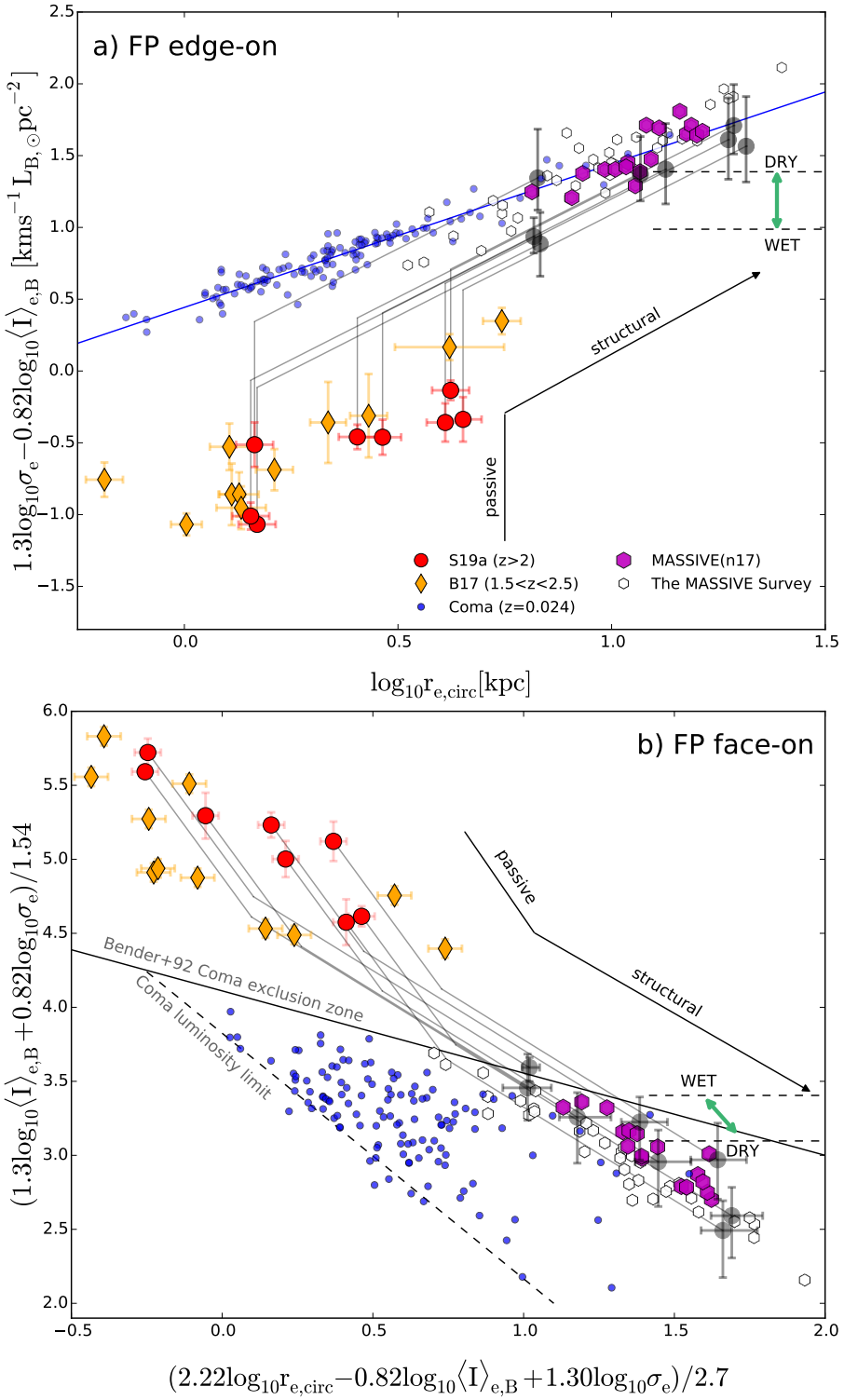

Figure 3.2: The FP edge-on (a) and face-on (b) with symbols as in Figure 3.1. The exclusion zone for local spheroidal galaxies from Bender et al. (1992b) and the Coma luminosity limit from Jørgensen et al. (2006) are shown in the face-on plane. A $FP_{z\sim2}$ is established when combining the COSMOS quiescent galaxies from *S19a* and *B17*. The size evolution via dry minor mergers together with passive evolution from $z = 2$ to 0 are consistent with the $z > 2$ *S19a* MQGs evolving into the most massive local Coma galaxies and the CND-matched MASSIVE(n_{17}) sample.

3.3 Evolution of the scaling relations

The evolution of the FP parameters can be formalised (Saglia et al. 2010, 2016) under the assumption of homology, where α, β are constant over time (Beifiori et al. 2017)

$$\Delta\log_{10} L = \frac{1+2\beta}{\beta}\,\Delta\log_{10} r_e - \frac{\alpha}{\beta}\,\Delta\log_{10}\sigma_e - \frac{\Delta\gamma}{\beta}. \tag{3.3}$$

The logarithmic difference is define by $\Delta\log_{10} X = \log_{10} X_{z=2} - \log_{10} X_{z=0}$ where X, in this case, is either the luminosity, size or dispersion. The zero point evolution is described by $\Delta\gamma = \gamma_z - \gamma_{z=0}$. Cluster studies at $z < 1$ (e.g. van der Marel & van Dokkum 2007) find that passive evolution of the stellar population is enough to bring the FP in agreement with local clusters. In this case ($\Delta\log_{10} r_e = \Delta\log_{10}\sigma_e = 0$), the equation gets reduced to $\Delta\log_{10} L = -\Delta\gamma/\beta$ where the zero point evolution directly arises from the luminosity decrease due to the passive evolving stellar population.

At higher redshift ($z > 1$), a significant size evolution is expected and observed (e.g. Bluck et al. 2012). In *S19a*, the median evolution of MQGs is such that the stellar mass doubles ($\Delta\log_{10} M_* \sim 0.3$ dex) and the size quadruples ($\Delta\log_{10} r_{e,circ} \sim 0.6$ dex), while no considerable velocity dispersion evolution ($\Delta\log_{10}\sigma_e \sim 0$) is observed. For massive quiescent galaxy evolution from $z = 2$ to present-day Equation 3.3 becomes

$$\Delta\log_{10} L = \frac{1+2\beta}{\beta}\,\Delta\log_{10} r_e - \frac{\Delta\gamma}{\beta}. \tag{3.4}$$

The zero point evolution of the FP and M/L ratio for the *S19a* MQGs are thus driven by both structural and passive evolution and described by

$$\frac{\Delta\gamma}{\beta} = \Delta\log_{10} M/L = \frac{1+2\beta}{\beta}\,\Delta\log_{10} r_e - \Delta\log_{10} L. \tag{3.5}$$

For this reason, the zero point evolution cannot be interpreted as passive evolution alone, and is estimated using the method below. The luminosity increase from added stellar population is modeled, assuming that the structural evolution is due to minor mergers, as shown in *S19a*.

The expected size, dynamical mass growth (from *S19a*) and luminosity decrease from passive evolution (Section 3.3.1) are shown in Figure 3.1 and 3.2. The predicted position of the massive quiescent galaxies following structural and passive evolution is, in both scaling relations, consistent with the most massive and largest Coma galaxies and the CND-matched MASSIVE(n_{17}) sample. The luminosity evolution from adding minor mergers (see Section 3.3.2), shown in Figure 3.1 and 3.2, favors quenched stellar populations with a insignificant rest-frame B-band luminosity contribution.

3.3.1 Passive evolution

The expected passive evolution of the stellar population, from the redshift of formation to present day, is based on the evolution in M_*/L of a BC03 (Bruzual & Charlot 2003) Simple Stellar Population (SSP) model with Chabrier IMF and solar metallicity. The formation redshift is estimated from the mass-weighted age and the redshift of observation. The passive evolution takes into account the mass-loss during stellar evolution, and the M_*/L is thus the mass locked into stars at a given age. The mass-weighted age represents the time of which the majority of the stellar mass is formed. The M_*/L uncertainties are dominated by the 1σ standard deviation of the age (~ 0.2 dex) when assuming solar metallicity.

The $M_{\rm dyn}/L$ ratio is estimated from the M_*/L ratio using the median evolution from $z = 2$ to 0 between the stellar and dynamical mass in *S19a* ($\Delta\log_{10}\mathrm{M_{dyn}} = 2\Delta\log_{10}\mathrm{M_*}$)

$$\begin{aligned}\Delta\log_{10}\frac{M_{\rm dyn}}{L} &= \Delta\log_{10}M_{\rm dyn} - \Delta\log_{10}L \\ &= 2\Delta\log_{10}M_* - \Delta\log_{10}L \\ &= \Delta\log_{10}\frac{M_*}{L} + \Delta\log_{10}M_*. \end{aligned} \tag{3.6}$$

The passive evolution for the individual galaxy age estimates are shown in Figure 3.1 and 3.2.

3.3.2 Luminosity increase from wet minor merger stellar populations

In addition to the decrease in B-band luminosity, due to the aging of the stellar population after the turn-off of star-formation ("passive evolution"), it is expected that merger events could add to the B-band luminosity if these are star-forming galaxies at the time of merging. From now on, this type of merger is referred to as "wet", contrary to the "dry" minor mergers that are passive before merging. The B-band luminosity increase from merging galaxies between $z = 2 - 0$ are modeled with composite stellar population models from the BC03 library with solar metallicity. The star-formation history follows the evolution of the main-sequence (Speagle et al. 2014). It is assumed that, after merging, the galaxies stop forming stars and follow a passive evolution.

The median stellar mass increase ($\Delta\log_{10}\mathrm{M_*} = 0.3$ dex) from minor mergers, predicted in *S19a*, are used assuming a 1:20 merger ratio. Note that in our simplistic model, the correct mass ratio does not play a significant role. We also investigate a more realistic scenario with mergers distributed across redshift (z=1.8-0.1) together with two extreme cases of all the mass added at $z = 1.8$ or 0.1. A similar B-band luminosity increase of $0.4 - 0.45$ dex is found in all cases (for more details see Appendix E and Figure 3.4). In Figure 3.1 and 3.2, the realistic scenario with a luminosity increase from wet minor mergers of 0.4 dex is shown.

4 Discussion

4.1 Passive evolution of massive quiescent galaxies from $z = 2$ to 0

Studies of passive galaxies in $0.8 < z < 1.8$ clusters (among others Jørgensen et al. 2006; van der Marel & van Dokkum 2007; Jørgensen & Chiboucas 2013; Beifiori et al. 2017; Jørgensen et al. 2019) find that the change in M/L ratio can be explained by passive evolution to $z = 0$. Below we explore if a similar analysis can account for the evolution of the scaling relations at $z \sim 2$.

Jørgensen & Chiboucas (2013) predicted the $M_{dyn}/L_{\rm B}$ ratio evolution, as a function of age and metallicity, to be $\log M_{dyn}/L_{\rm B} = 0.935 \log \text{age} + 0.337[\rm M/H] - 0.053$. Assuming passive evolution from $z = 2$ to the best-fit Coma relation, at $\log_{10}(\rm M_{dyn}/M_{\odot}) = 11.5$, we find a formation redshift of $z_{\rm form,Coma} = 2.01^{+0.1}_{-0.04}$ (for details see Appendix F). The formation redshift is similar to the redshift of observation which leaves too short time to form the *S19a* MQGs at this epoch. The formation redshift, derived from our stellar population mass-weighted ages (assuming the median age), is $z_{\rm form} = 3.41^{+4.92}_{-0.91}$. The uncertainties are estimated using the 1σ age uncertainties. Based on this, we cement that the *S19a* MQGs cannot evolve to the Coma relation by passive evolution alone, as expected.

4.2 Minor merger-driven structural evolution of massive quiescent galaxies

The fixed CND-matched MASSIVE($\rm n_{17}$) sample allows us to study the evolution of the scaling relations from $z = 2$ to 0 with minimal progenitor bias. Evidence against purely passive evolution to $z = 0$ is presented in both the scaling relations (Figure 3.1 and 3.2) and explicitly shown in the previous section. The *S19a* MQGs at $z > 2$ are consistent with evolving into the most massive Coma galaxies and the MASSIVE($\rm n_{17}$) sample through structural and passive evolution (see Figure 3.1 and 3.2).

The size increase of massive quiescent galaxies, in cosmological simulations (Dubois et al. 2013; Choi et al. 2018), can be explained by adiabatic expansion due to AGN, decreasing the central mass density and puffing up the galaxies. Major mergers, as the dominant mechanism for size growth, have gained less popularity as it makes the galaxies too massive to be consistent with massive nearby galaxies. In *S19a*, the structural evolution are interpreted to be of minor merger origin in line with the scenario presented in the idealised simulations from Hopkins et al. (2009); Naab et al. (2009); Hilz et al. (2012, 2013). Here, the effective half-light radius is suggested to grow by adding stars to the outskirts of the galaxy from tidally stripped minor mergers. This scenario is, in Hilz et al. (2013), shown to cause inside-out growth, starting from a compact elliptical galaxy (core) that becomes, through the minor merger build-up of the surface density profile wings, a present-day analog of a giant elliptical galaxy (core-envelope). A consequence of the inside-out minor merger growth scenario from Hilz et al. (2012) is an increasing dark matter fraction which

has been suggested to cause a tilt in the FP over time (Boylan-Kolchin et al. 2005; D'Onofrio et al. 2013). Larger sample size and better dispersion measurements might reveal if such a trend is present at this epoch.

4.3 Dry minor merger evolution

In Section 3.3.2, the predicted luminosity increase from wet minor mergers are modeled under the assumption that they are the primary drivers of the size growth. For the realistic scenario of adding wet minor mergers continuously from $z = 2$ to 0, we find that the luminosity increases by roughly 0.4 dex.

In Figure 3.1 and 3.2a, the predicted position of the *S19a* MQGs (following passive and structural evolution) are indicated alongside the effect of the luminosity from wet minor mergers. The green arrow indicates how the predictions would move compared to the local best-fit relation of Coma and the locus of the MASSIVE(n_{17}) sample, strongly favoring dry minor mergers. Improved measurements of the velocity dispersion could further constrain how dry the minor mergers are.

In the inside-out growth scenario, the rest-frame B-band luminosity increase takes place in the outer parts of the galaxy. The luminosity from the MASSIVE(n_{17}) sample is measured using SDSS modelMag which represent the luminosity of the galaxy out to $8r_e$. Thus, a underestimation of the luminosity, by only sampling the central part of the galaxy and missing the outskirts, is unlikely. The wet minor merger luminosity increase is $> 1\sigma$ offset from the local relation and the MASSIVE(n_{17}) sample, and thus not a favored way to grow the structures of the *S19a* MQGs. Another possibility is that the minor merger galaxies, before their merger, already have quenched stellar populations with low rest-frame B-band luminosity (Oogi & Habe 2013; Naab et al. 2014; Tapia et al. 2014). The evolution from $z = 2$ to 0 of the FP and M/L ratio scaling relations are consistent with such a scenario, caused primarily by dry minor mergers and passive evolution, for massive quiescent galaxies.

4.4 Caveats

Data from *S19a* and *B17* are combined to establish the $\mathrm{FP}_{z\sim2}$ at $1.5 < z < 2.5$ with more than half of the sources at $z > 2$. A large fraction of the quiescent galaxies from *B17* is found to be disk-like (based on Sérsic index, $n < 2.5$ Belli et al. 2017), which could mean that an unknown contribution from rotation is included in the measured velocity dispersion. For spherical dispersion-dominated systems, the circularized radius and semi-major axis are comparable methods of size measurement. However, for more disk-like systems the difference grows between the two size measuring methods, further causing a bias between dispersion and rotation dominated galaxies. We estimate, based on the axis ratios, that the circularised sizes differ by $7 - 30\%$ compared to the semi-major axes. This is well within the quoted uncertainties of the predicted position of the *S19a* MQGs at $z = 0$. This bias could potentially affect the zero point and coefficients of the best-fit in Figure 3.1 and

3.2. This issue could be solved by spatially resolved spectroscopy disentangling the contribution from rotation and dispersion.

The dominating uncertainty, mass-rank scatter, of the CND-matching of the local MASSIVE(n_{17}) sample does not affect the qualitative conclusions of this study. Furthermore, if using a probabilistic CND-matching approach (see Wellons & Torrey 2017), this would increase the number of galaxies in the MASSIVE(n_{17}) sample from 17 to 30. In Figure 3.1 and 3.2 this would correspond to a greater number of white hexagons becoming purple, which causes no noticeable effects on the trends in the figures. On the other hand, if not all massive quiescent galaxies at $z > 2$ have similar merger histories, descendants that e.g. become star-forming at late times would have been missed (see e.g. Naab et al. 2014).

5 Summary and conclusion

In this work, we present the highest redshift study of quiescent galaxy scaling relations which are $2\times$ larger than previous studies at this redshift. The M/L ratio of massive quiescent galaxies at $z > 2$ are observed to be $\sim 30 - 40\times$ smaller than the local Coma relation (at fixed dynamical mass) and require significant luminosity evolution to match the $z = 0$ relation. In *S19a*, the same galaxies are shown to undergo considerable structural evolution by quadrupling their sizes from $z = 2$ to 0, while their effective dispersion remains nearly unchanged. The FP and M/L ratio established scaling relations at $z \sim 2$, and the expected structural and passive evolution, are explored for the *S19a* MQGs from $z = 2$ to 0. The main conclusions of this study are listed below:

- The FP and M/L ratio relations are established using the combined quiescent galaxy sample from *S19a* and *B17*. Compared to the local Coma cluster and the CND-matched MASSIVE(n_{17}) sample, the quiescent galaxies at high redshift are found to be compact and rest-frame B-band brighter due to more recently quenched stellar populations.

- Interpreting the M/L ratio offset due to purely passive evolution of the stellar population leads to a formation redshift of $z \sim 2$, lower than the formation redshift inferred from the stellar population analysis of *S19a* MQGs, $z_{\rm form} = 3.41^{+4.92}_{-0.91}$ (Section 4.1). As a result, the *S19a* MQGs are not consistent with their evolution into the local Coma FP and M/L ratio scaling relations by passive evolution alone.

- The *S19a* MQGs are consistent with minor merger structural and passive evolution into the most massive local Coma galaxies and the CND-matched MASSIVE(n_{17}) sample.

- In the case that the observed size evolution can be attributed entirely to minor mergers, the FP and M/L ratio evolution are consistent with the accretion of dry minor merger

stellar populations. Wet, star-forming, minor mergers are found to increase the rest-frame B-band luminosity by 0.4 dex inconsistent with evolving into the local massive Coma and the CND-matched MASSIVE(n_{17}) galaxies.

Acknowledgements

M.S. and S.T. acknowledge support from the European Research Council (ERC) Consolidator Grant funding scheme (project ConTExt, grant number 648179). Based on observations made with the NASA/ESA Hubble Space Telescope, obtained from the data archive at the Space Telescope Science Institute. STScI is operated by the Association of Universities for Research in Astronomy, Inc. under NASA contract NAS 5-26555. Support for this work was provided by NASA through grant number HST-GO-14721.002 from the Space Telescope Science Institute, which is operated by AURA, Inc., under NASA contract NAS 5-26555. M.S. thank Nina Voit for her encouragement and unparalleled love, help, and support. This research made use of Astropy (version 1.1.1),[4] a community-developed core Python package for Astronomy (Astropy Collaboration et al. 2013, 2018). I.J. is supported by the Gemini Observatory, which is operated by the Association of Universities for Research in Astronomy, Inc., on behalf of the international Gemini partnership of Argentina, Brazil, Canada, Chile, the Republic of Korea, and the United States of America. M. H. acknowledges financial support from the Carlsberg Foundation via a Semper Ardens grant (CF15-0384).

[4] http://www.astropy.org

Appendices

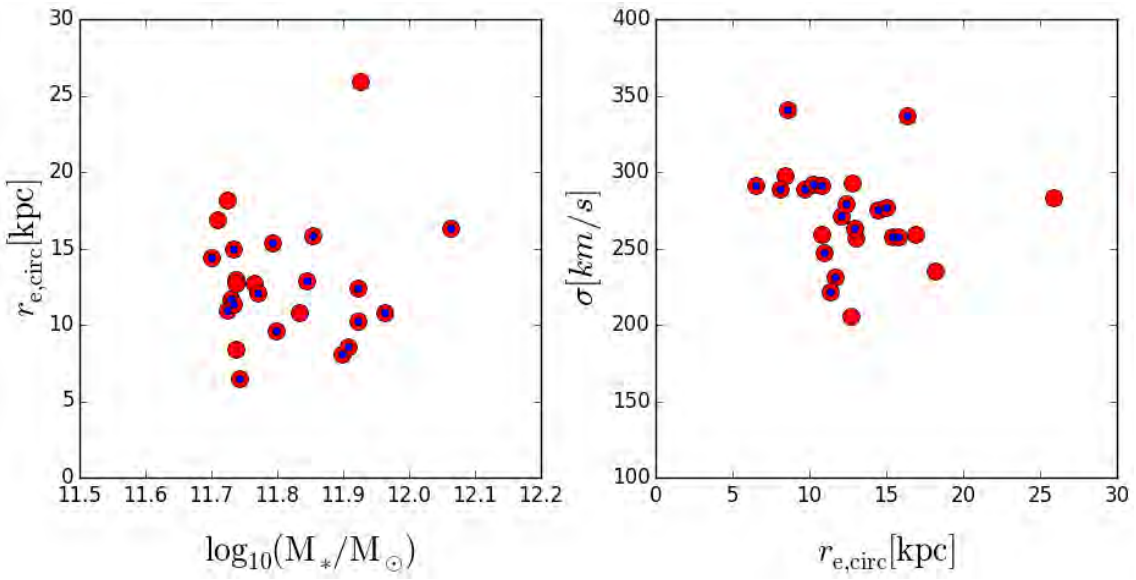

Figure 3.3: The distribution of MASSIVE(n) (red) and MASSIVE(n_{17}) (blue) for the stellar mass-size and size-dispersion plane. The MASSIVE(n_{17}) sample, with available SDSS photometry, is selected uniformly from the parent MASSIVE(n) sample and can be considered representative for the CND-matched parent sample.

D The derivation of the effective surface brightness, $\langle I \rangle_{e,\mathrm{B}}$

The luminosity and average effective surface brightness are estimated by converting the EAZY (Brammer et al. 2008) calculated rest-frame B-band fluxes to apparent AB magnitudes (assuming no extinction correction) and calculating the absolute Vega magnitudes and luminosity

$$M_{Vega,\mathrm{B}} = m_{Vega,\mathrm{B}} - 5 * (log10(D_L/pc) - 1) \quad \frac{L_{B,gal}}{L_{B,\odot}} = 10^{-0.4(M_{Vega,\mathrm{B}} - M_{\odot,\mathrm{B}})}. \tag{3.7}$$

Here the luminosity distance (D_L) and $M_{\mathrm{B},\odot} = 5.45$[5] are used. The effective surface brightness in Bessel B-band is calculated as

$$\langle I \rangle_{e,\mathrm{B}} = \frac{L_{\mathrm{B},gal}/L_{\mathrm{B},\odot}}{2\pi r_e^2}. \tag{3.8}$$

Note that cosmological redshift dimming is included when converting the radius from arcsec to parsec.

[5] http://mips.as.arizona.edu/~cnaw/sun.html

E Details on the modelling of the B-band luminosity increase due to minor merger added stellar populations

The amount of B-band luminosity increase due to minor merger added stellar populations are constrained between redshifts $z = 2$ to 0, based on simple assumptions. Figure 3.4 shows the B-band luminosity increase due to minor mergers (on top of the luminosity decrease due to passive evolution) as a function of redshift for three scenarios. In scenario A, it is assumed that all the merging happens about 300 Myrs after the galaxies are observed at $z = 1.8$. In scenario B, the galaxies merge at z=0.1. Note that, since the merging galaxies follow the global star-forming main-sequence, and hence have lower SFRs at lower redshifts on average, the increase in luminosity is less at $z = 0.1$ than at $z = 1.8$. Finally, scenario C shows a more realistic merger history for which $10\ \%, 20\ \%, 30\ \%$, and $40\ \%$ of the merging happens at $z = 0.1, 0.5, 1.5$, and 1.8, respectively. These follow roughly the measured trends of merger fraction in the literature (e.g. Man et al. 2012; Newman et al. 2012; Man et al. 2016a). Although the merger history in the different scenarios is very different, the final increase in rest-frame B-band luminosity is very similar between 0.4 and 0.45 dex.

F Formation redshift from M/L relation

Jørgensen & Chiboucas (2013) predicted the $M/L_{\rm B}$ ratio evolution as a function of age and metallicity (Jørgensen & Chiboucas 2013, Table 9) using Maraston (2005) models

$$\log M/L_{\rm B} = 0.935 \log \text{age} + 0.337[\text{M/H}] - 0.053. \tag{3.9}$$

For passive evolution with constant metallicity, the difference in $\log_{10} M/L_{\rm B}$ can be related to the age of the stellar population

$$\Delta \log M/L_{\rm B} = 0.935\ \Delta \log \text{age} \tag{3.10}$$

If the MQGs at $z > 2$ are the progenitors of the local Coma relation, the change in $M/L_{\rm B}$ (at fixed dynamical mass) can be used to estimate a corresponding formation time. The age difference can be written in terms of look-back times and expressed as the formation time

$$\begin{aligned}
\Delta \log \text{age} &= \log \text{age}_{z=0} - \log \text{age}_{z\sim 2} && (3.11)\\
&= \log(t_{\rm form} - t_{{\rm obs},z=0}) - \log(t_{\rm form} - t_{{\rm obs},z\sim 2}) && (3.12)\\
&= \log\left(\frac{1 - t_{\rm form}/t_{{\rm obs},z=0}}{1 - t_{\rm form}/t_{{\rm obs},z\sim 2}}\right) && (3.13)\\
\Leftrightarrow t_{\rm form} &= \frac{10^{\Delta \log \text{ age}} \cdot t_{{\rm obs},z\sim 2} - t_{{\rm obs},z=0}}{10^{\Delta \log \text{ age}} - 1} && (3.14)\\
&= \frac{10^{(\Delta \log M/L_{\rm B})/0.935} \cdot t_{{\rm obs},z\sim 2} - t_{{\rm obs},z=0}}{10^{(\Delta \log M/L_{\rm B})/0.935} - 1} && (3.15)
\end{aligned}$$

The uncertainty on the formation redshift is estimated by varying the M/L ratio uncertainties (~ 0.25 dex).

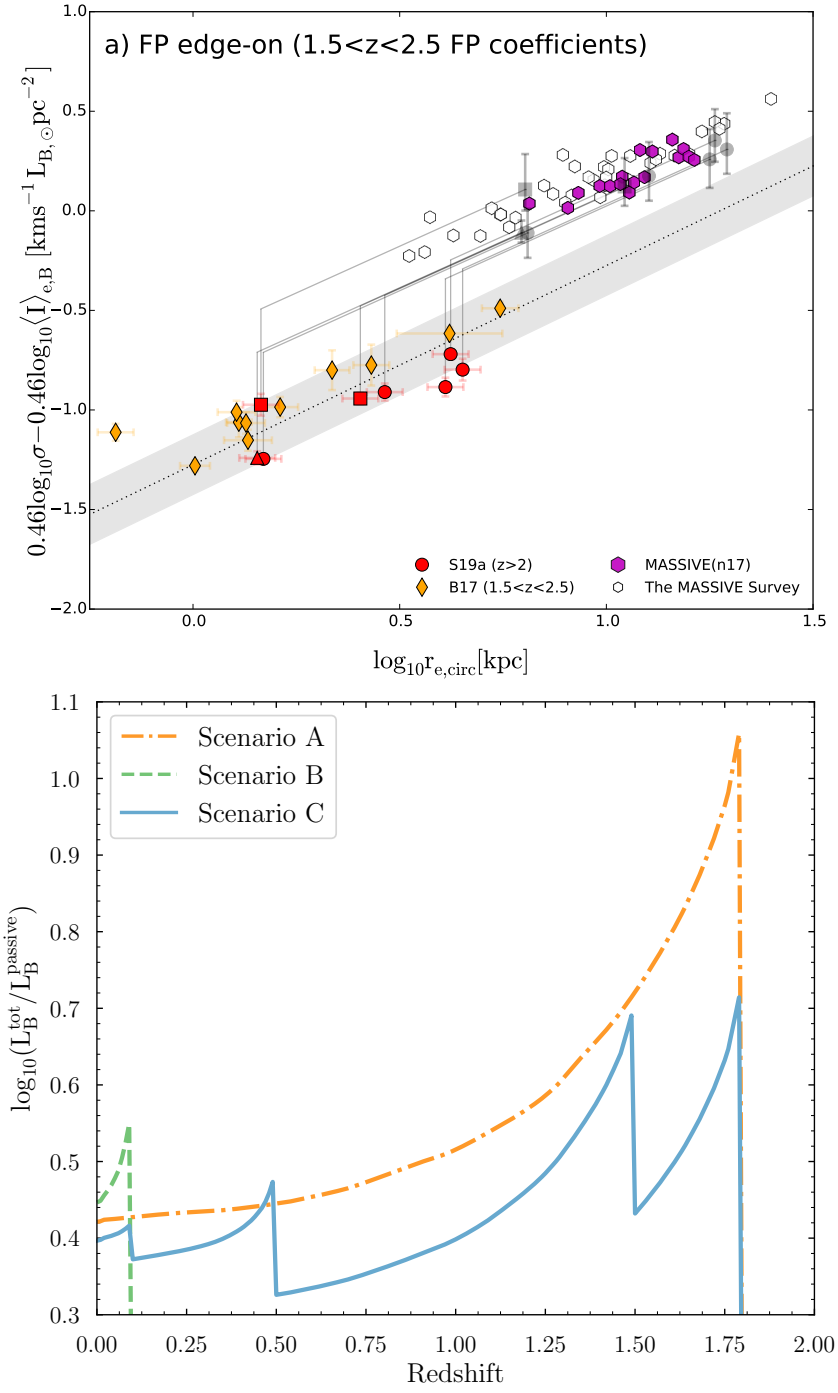

Figure 3.4: Top: The $FP_{z\sim2}$ edge-on in its best-fit projection (see Table 3.2). The residuals for the high redshift samples in this study are minimized, compared to the best-fit Coma edge-on orientation, when showing them in their optical orientation. Bottom: Luminosity evolution of minor merger added quenched stellar populations (SFR main sequence SFH) at different redshifts compared to an underlying passive evolving SED. The minor mergers added are match to the predicted stellar mass increase. Model C, the most realistic one adds relative fractions $0.1/0.2/0.3/0.4$ of minor mergers at a redshift of $z = 0.1/0.5/1.5/1.8$, where as model A and B assumes the extremes of adding all the stellar populations at either 1.8 and $z = 0.1$, respectively. The luminosity increase is scaling directly with the added stellar mass and is independent of the mass ratio. The final relative luminosity increase due to minor merger-driven structural evolution is not strongly affected by adding stellar mass at different epochs and give values of $\log_{10}(L_B^{tot}/L_B^{passive}) \sim 0.4$.

4

Conclusion and Outlook

Astronomy is the oldest science dedicated to understanding the origin of fundamental properties such as time, space and life. Through centuries of paradigms, it has widened our understanding and absurdly taught us that we know very little about the Universe and its constituents. The study of galaxies have, in the meantime, prospered significantly and, within the last 20 years, observations and simulations have uncovered billions of years of evolution. My research has used the observatories to study the compact quiescent galaxies at the edge of the Universe and to explore their connection to the massive elliptical galaxies in the nearby Universe. The main conclusions of this dissertation are summarized below together with my ongoing and future research objectives.

In Chapter 2, the structural and dynamical measurements of 15 massive quiescent galaxies at $z > 2$ were presented. These were obtained through a total of $\sim$ 85 hours of X-Shooter spectroscopic and $\sim$ 15 hours of *HST* imaging observations. Multi-wavelength photometry and UV-to-NIR spectroscopy allowed for detailed modeling of the SED, revealing massive quiescent galaxies observed just 1.5 Gyrs after their stars were formed. This was corroborated by the lack of optical emission lines and low mid-IR emission that confirmed their quiescent nature, when they were compared to star-forming galaxies at the same epoch. The images revealed disturbed morphology in 40% of the galaxies, including three ongoing quiescent-to-quiescent galaxy major mergers indicating the importance of mergers in their evolution. It was found that high-velocity dispersions are common among massive quiescent galaxies. The galaxies are compact in the stellar mass-size relation at a similar epoch, however, they span a higher stellar mass range and could be among the most massive quiescent galaxies at $z > 2$. The progenitor bias is minimized by comparing the sample of this thesis to a number density matched local sample of massive galaxies. This confirmed the suspicion of merger induced growth, preferring minor merger-driven size evolution. It is not possible to rule out other size growth mechanisms, e.g. AGN feedback. However, I find that progenitor bias does not play a pivotal role in the evolution of the most massive galaxies. This is further corroborated by indications of shallow velocity dispersion evolution, which has also been suggested as a tracer of progenitor free comparisons. Finally, the dynamical-to-stellar mass ratio is found to increase, which is interpreted as a growing dark matter fraction within the effective radius over time. This result strengthens the evidence for minor merger-driven size growth as a way to connect the structures of compact quiescent

galaxies at $z > 2$ with nearby massive elliptical galaxies.

In Chapter 3, the Fundamental Plane and M/L ratio scaling relations were established in the epoch at $1.5 < z < 2.5$, combining the COSMOS galaxies from Belli et al. (2017) and Stockmann et al. (2019). The establishment of the scaling relations reveal that they have been in place for more than 10 billion years and must have formed when the Universe was in its infant state of galaxy formation. Stellar population ages suggest a formation redshift at $z_{\rm form} \gtrsim 3.5$, only 1-2 Gyrs after the Big Bang. The compact quiescent galaxies are, orders of magnitude, offset from the local Coma best-fit relation and must undergo both significant luminosity decrease and dynamical mass growth to evolve into present-day massive elliptical galaxies. In summary, the results of this study show that the evolution of the FP and M/L ratio scaling relations of massive quiescent galaxies at $z \sim 2$ into nearby massive elliptical galaxies are consistent with passive evolution of the stellar population and dry minor merger-driven size growth.

My future research objectives include further analysis of the data-rich sample, presented in Chapter 2. Detailed stellar population analysis of the composite massive quiescent galaxy spectrum will allow estimation of accurate mean age, metallicity and element abundance ratios (see Figure 1.5) essential for understanding their formation and evolution to lower redshifts. The relation between AGN and quenching of massive galaxies will be explored in the analysis of the 6 out of 15 galaxies with radio emission from Chapter 2. Photometric clustering can be used to ascertain if their massive nature can be connected to high-density environments, already at $z > 2$.

The objectives include the study of massive quiescent galaxies at higher redshift closer to their epoch of formation. One such example of a massive quiescent galaxy at the record-breaking redshift of $z = 4$ has been spectroscopically confirmed and can be used to measure the star formation history and possibly the quenching time-scale. The search for quiescent galaxies at even earlier times requires large cosmological fields like COSMOS with both multi-wavelength photometry including deep IR imaging to sample the SED and Balmer break at $z > 4$.

Gravitational lensing is a powerful tool that can be used to spatially resolve the internal structure, kinematics and stellar populations of quiescent galaxies. Examples of well-studied lensing clusters with highly lensed quiescent galaxies are rare. I have located two examples of such and have, as principal investigator, used X-Shooter to observe these galaxies (see Figure 1.8), providing spectra with unprecedented S/N. REQUIEM, an *HST* grism spectroscopy campaign of a larger sample of gravitationally lensed quiescent galaxies, at $1.6 < z < 2.9$, can be used to study their internal structure, kinematics and stellar populations. This effort addresses among others the concern that if rotation is common in massive quiescent galaxies, the line of sight velocity dispersion measurements could be overestimated due to a combination of both dispersion and rotation. Furthermore, improving the uncertain velocity dispersion measurements increases the predictive power of the dynamical mass and FP scaling relations at high redshift. ALMA follow-up studies to characterize the amount of gas in massive quiescent galaxies can constrain the possible

mechanisms of how their star-formation is quenched.

This dissertation sheds light on the evolution of massive elliptical galaxies over 10 billion years. The presented sample of massive quiescent galaxies at $z > 2$ contains exceptional candidates for detailed spectroscopic follow-up using the upcoming *James Webb Space Telescope (JWST)*. Over the coming decade, the next-generation facilities like JWST, Euclid and the large ground-based observatories (TMT, E-ELT) will, together with current facilities like ALMA, VLA, *HST*, revolutionize the understanding of the cosmic dark ages by shedding light on how, when and where the seeds of the first galaxies formed.

List of Publications

1. **Stockmann, M.**; Jørgensen, I.; Toft, S.; Conselice, C. J.; Faisst, A.; Margalef-Bentabol, B.; Gallazzi, A.; Zibetti, S.; Hirschmann, M.; Lagos, C. D.; Zabl, J.; Brammer, G. B.; Gomez-Guijarro, C.; & Valentino, F. M.,
A Fundamental Plane Study of Massive Quiescent Galaxies at $z \sim 2$,
In preparation for submission to ApJ, 2019

2. **Stockmann, M.**; Toft, S.; Gallazzi, A.; Zibetti, S.; Conselice, C. J.; Margalef-Bentabol, B.; Zabl, J.; Jørgensen, I.; Magdis, G. E.; Gomez-Guijarro, C.; Valentino, F. M.; Brammer, G. B.; Ceverino, D.; Cortzen, I.; Davidzon, I.; Demarco, R.; Faisst, A.; Hirschmann, M.; Krogager, J.-K.; Lagos, C. D.; Man, A. W. S.; Mundy, C. J.; Peng, Y.; Selsing, J.; Steinhardt, C. L.; & Whitaker, K. E.,
X-Shooter Spectroscopy and HST Imaging of 15 Ultra Massive Quiescent Galaxies at $z \gtrsim 2$,
Submitted to ApJ, 30 July 2019

3. Cortzen, I.; Garrett, J.; Magdis, G.; Rigopoulou, D.; Valentino, F.; Pereira-Santaella, M.; Combes, F.; Alonso-Herrero, A.; Toft, S.; Daddi, E.; Elbaz, D.; Gómez-Guijarro, C.; **Stockmann, M.**; Huang, J.; & Kramer, C,
PAHs as tracers of the molecular gas in star-forming galaxies,
MNRAS, 482, 1618, 2019 (arXiv:1810.05178)

4. Kubo, M.; Tanaka, M.; Yabe, K.; Toft, S.; **Stockmann, M.**; & Gómez-Guijarro, C.,
The Rest-frame Optical Sizes of Massive Galaxies with Suppressed Star Formation at $z \sim 4$,
ApJ, 867, 1, 2018 (arXiv:1810.00543)

5. Gómez-Guijarro, C.; Toft, S.; Karim, A.; Magnelli, B.; Magdis, G. E.; Jiménez-Andrade, E. F.; Capak, P. L.; Fraternali, F.; Fujimoto, S.; Riechers, D. A.; Schinnerer, E.; Smolčić, V.; Aravena, M.; Bertoldi, F.; Cortzen, I.; Hasinger, G.; Hu, E. M.; Jones, G. C.; Koekemoer, A. M.; Lee, N.; McCracken, H. J.; Michałowski, M. J.; Navarrete, F.; Pović, M.; Puglisi, A.; Romano-Díaz, E.; Sheth, K.; Silverman, J. D.; Staguhn, J.; Steinhardt, C. L.; **Stockmann, M.**; Tanaka, M.; Valentino, F.; van Kampen, E.; & Zirm, A.,
Starburst to Quiescent from HST/ALMA: Stars and Dust Unveil Minor Mergers in Submillimeter Galaxies at $z \sim 4.5$,
ApJ, 856, 121, 2018 (arXiv:1802.07751)

6. Ebeling, H.; **Stockmann, M.**; Richard, J.; Zabl, J.; Brammer, G.; Toft, S.; Man, A.,
Thirty-fold: Extreme Gravitational Lensing of a Quiescent Galaxy at z = 1.6,
ApJ, 852, L7, 2018 (arXiv:1802.00133)

7. Toft, S.; Zabl, J.; Richard, J.; Gallazzi, A.; Zibetti, S.; Prescott, M.; Grillo, C.; Man, A. W. S.; Lee, N. Y.; Gómez-Guijarro, C.; **Stockmann, M.**; Magdis, G.; & Steinhardt, C. L.,
A massive, dead disk galaxy in the early Universe,
Nature, 546, 510, 2017 (arXiv:1706.07030)

8. Laigle, C.; McCracken, H. J.; Ilbert, O.; Hsieh, B. C.; Davidzon, I.; Capak, P.; Hasinger, G.; Silverman, J. D.; Pichon, C.; Coupon, J.; Aussel, H.; Le Borgne, D.; Caputi, K.; Cassata, P.; Chang, Y. -Y.; Civano, F.; Dunlop, J.; Fynbo, J.; Kartaltepe, J. S.; Koekemoer, A.; Le Fèvre, O.; Le Floc'h, E.; Leauthaud, A.; Lilly, S.; Lin, L.; Marchesi, S.; Milvang-Jensen, B.; Salvato, M.; Sanders, D. B.; Scoville, N.; Smolcic, V.; **Stockmann, M.**; Taniguchi, Y.; Tasca, L.; Toft, S.; Vaccari, Mattia; & Zabl, J.,
The COSMOS2015 Catalog: Exploring the 1 < z < 6 Universe with Half a Million Galaxies,
ApJS, 224, 24, 2016 (arXiv:1604.02350)

Bibliography

Albrecht, A., & Steinhardt, P. J. 1982, Phys. Rev. Lett., 48, 1220, doi: 10.1103/PhysRevLett.48.1220

Allen, R. J., Kacprzak, G. G., Spitler, L. R., et al. 2015, ApJ, 806, 3, doi: 10.1088/0004-637X/806/1/3

Alpher, R. A., Bethe, H., & Gamow, G. 1948, Physical Review, 73, 803, doi: 10.1103/PhysRev.73.803

Arcila-Osejo, L., Sawicki, M., Arnouts, S., et al. 2019, MNRAS, 1124, doi: 10.1093/mnras/stz1169

Arnouts, S., Le Floc'h, E., Chevallard, J., et al. 2013, A&A, 558, A67, doi: 10.1051/0004-6361/201321768

Astropy Collaboration, Robitaille, T. P., Tollerud, E. J., et al. 2013, A&A, 558, A33, doi: 10.1051/0004-6361/201322068

Astropy Collaboration, Price-Whelan, A. M., Sipőcz, B. M., et al. 2018, AJ, 156, 123, doi: 10.3847/1538-3881/aabc4f

Barden, M., Häußler, B., Peng, C. Y., McIntosh, D. H., & Guo, Y. 2012, MNRAS, 422, 449, doi: 10.1111/j.1365-2966.2012.20619.x

Barro, G., Faber, S. M., Pérez-González, P. G., et al. 2013, ApJ, 765, 104, doi: 10.1088/0004-637X/765/2/104

Barro, G., Faber, S. M., Koo, D. C., et al. 2017, ApJ, 840, 47, doi: 10.3847/1538-4357/aa6b05

Bédorf, J., & Portegies Zwart, S. 2013, MNRAS, 431, 767, doi: 10.1093/mnras/stt208

Behroozi, P. S., Marchesini, D., Wechsler, R. H., et al. 2013, ApJ, 777, L10, doi: 10.1088/2041-8205/777/1/L10

Beifiori, A., Mendel, J. T., Chan, J. C. C., et al. 2017, ApJ, 846, 120, doi: 10.3847/1538-4357/aa8368

Bell, E. F., van der Wel, A., Papovich, C., et al. 2012, ApJ, 753, 167, doi: 10.1088/0004-637X/753/2/167

Belli, S., Newman, A. B., & Ellis, R. S. 2014a, ApJ, 783, 117, doi: 10.1088/0004-637X/783/2/117

—. 2017, ApJ, 834, 18, doi: 10.3847/1538-4357/834/1/18

—. 2019, ApJ, 874, 17, doi: 10.3847/1538-4357/ab07af

Belli, S., Newman, A. B., Ellis, R. S., & Konidaris, N. P. 2014b, ApJ, 788, L29, doi: 10.1088/2041-8205/788/2/L29

Bender, R., Burstein, D., & Faber, S. M. 1992a, ApJ, 399, 462, doi: 10.1086/171940

—. 1992b, ApJ, 399, 462, doi: 10.1086/171940

Bendo, G. J., Boselli, A., Dariush, A., et al. 2012, MNRAS, 419, 1833, doi: 10.1111/j.1365-2966.2011.19735.x

Bernardi, M., Sheth, R. K., Annis, J., et al. 2003, AJ, 125, 1866, doi: 10.1086/367794

Bertin, E., & Arnouts, S. 1996, A&AS, 117, 393, doi: 10.1051/aas:1996164

Bertin, E., Mellier, Y., Radovich, M., et al. 2002, in Astronomical Society of the Pacific Conference Series, Vol. 281, Astronomical Data Analysis Software and Systems XI, ed. D. A. Bohlender, D. Durand, & T. H. Handley, 228

Best, P. N., & Heckman, T. M. 2012, MNRAS, 421, 1569, doi: 10.1111/j.1365-2966.2012.20414.x

Bezanson, R., Franx, M., & van Dokkum, P. G. 2015, ApJ, 799, 148, doi: 10.1088/0004-637X/799/2/148

Bezanson, R., Spilker, J., Williams, C. C., et al. 2019, ApJ, 873, L19, doi: 10.3847/2041-8213/ab0c9c

Bezanson, R., van Dokkum, P., & Franx, M. 2012, ApJ, 760, 62, doi: 10.1088/0004-637X/760/1/62

Bezanson, R., van Dokkum, P. G., Tal, T., et al. 2009, ApJ, 697, 1290, doi: 10.1088/0004-637X/697/2/1290

Bezanson, R., van Dokkum, P. G., van de Sande, J., et al. 2013, ApJ, 779, L21, doi: 10.1088/2041-8205/779/2/L21

Bezanson, R., van der Wel, A., Pacifici, C., et al. 2018, ApJ, 858, 60, doi: 10.3847/1538-4357/aabc55

Blakeslee, J. P., Franx, M., Postman, M., et al. 2003, ApJ, 596, L143, doi: 10.1086/379234

Blanton, M. R., Bershady, M. A., Abolfathi, B., et al. 2017, AJ, 154, 28, doi: 10.3847/1538-3881/aa7567

Bluck, A. F. L., Conselice, C. J., Buitrago, F., et al. 2012, ApJ, 747, 34, doi: 10.1088/0004-637X/747/1/34

Boylan-Kolchin, M., Ma, C.-P., & Quataert, E. 2005, MNRAS, 362, 184, doi: 10.1111/j.1365-2966.2005.09278.x

Brammer, G. B., van Dokkum, P. G., & Coppi, P. 2008, ApJ, 686, 1503, doi: 10.1086/591786

Brammer, G. B., Whitaker, K. E., van Dokkum, P. G., et al. 2011, ApJ, 739, 24, doi: 10.1088/0004-637X/739/1/24

Brinchmann, J., Charlot, S., White, S. D. M., et al. 2004, MNRAS, 351, 1151, doi: 10.1111/j.1365-2966.2004.07881.x

Bruzual, G., & Charlot, S. 2003, MNRAS, 344, 1000, doi: 10.1046/j.1365-8711.2003.06897.x

Buitrago, F., Trujillo, I., Conselice, C. J., et al. 2008, ApJ, 687, L61, doi: 10.1086/592836

Buitrago, F., Trujillo, I., Conselice, C. J., & Häußler, B. 2013, MNRAS, 428, 1460, doi: 10.1093/mnras/sts124

Capak, P., Aussel, H., Ajiki, M., et al. 2007, ApJS, 172, 99, doi: 10.1086/519081

Cappellari, M., & Emsellem, E. 2004, PASP, 116, 138, doi: 10.1086/381875

Cappellari, M., Bacon, R., Bureau, M., et al. 2006a, MNRAS, 366, 1126, doi: 10.1111/j.1365-2966.2005.09981.x

—. 2006b, MNRAS, 366, 1126, doi: 10.1111/j.1365-2966.2005.09981.x

Cappellari, M., McDermid, R. M., Alatalo, K., et al. 2012, Nature, 484, 485, doi: 10.1038/nature10972

Cappellari, M., Scott, N., Alatalo, K., et al. 2013, MNRAS, 432, 1709, doi: 10.1093/mnras/stt562

Carollo, C. M., Bschorr, T. J., Renzini, A., et al. 2013, ApJ, 773, 112, doi: 10.1088/0004-637X/773/2/112

Chabrier, G. 2003, PASP, 115, 763, doi: 10.1086/376392

Chang, Y.-Y., van der Wel, A., Rix, H.-W., et al. 2013, ApJ, 762, 83, doi: 10.1088/0004-637X/762/2/83

Charlot, S., & Fall, S. M. 2000, ApJ, 539, 718, doi: 10.1086/309250

Choi, E., Somerville, R. S., Ostriker, J. P., Naab, T., & Hirschmann, M. 2018, ApJ, 866, 91, doi: 10.3847/1538-4357/aae076

Cimatti, A., Nipoti, C., & Cassata, P. 2012, MNRAS, 422, L62, doi: 10.1111/j.1745-3933.2012.01237.x

Cimatti, A., Daddi, E., Renzini, A., et al. 2004, Nature, 430, 184, doi: 10.1038/nature02668

Cimatti, A., Cassata, P., Pozzetti, L., et al. 2008, A&A, 482, 21, doi: 10.1051/0004-6361:20078739

Comerford, J. M., & Greene, J. E. 2014, ApJ, 789, 112, doi: 10.1088/0004-637X/789/2/112

Conselice, C. J., Blackburne, J. A., & Papovich, C. 2005, ApJ, 620, 564, doi: 10.1086/426102

Conselice, C. J., Bluck, A. F. L., Buitrago, F., et al. 2011, MNRAS, 413, 80, doi: 10.1111/j.1365-2966.2010.18113.x

Daddi, E., Cimatti, A., Renzini, A., et al. 2004, ApJ, 600, L127, doi: 10.1086/381020

Daddi, E., Renzini, A., Pirzkal, N., et al. 2005, ApJ, 626, 680, doi: 10.1086/430104

Damjanov, I., Abraham, R. G., Glazebrook, K., et al. 2011, ApJ, 739, L44, doi: 10.1088/2041-8205/739/2/L44

De Lucia, G., & Blaizot, J. 2007, MNRAS, 375, 2, doi: 10.1111/j.1365-2966.2006.11287.x

De Lucia, G., Springel, V., White, S. D. M., Croton, D., & Kauffmann, G. 2006, MNRAS, 366, 499, doi: 10.1111/j.1365-2966.2005.09879.x

Dekel, A., Birnboim, Y., Engel, G., et al. 2009, Nature, 457, 451, doi: 10.1038/nature07648

Delaye, L., Huertas-Company, M., Mei, S., et al. 2014, MNRAS, 441, 203, doi: 10.1093/mnras/stu496

Dicke, R. H., Peebles, P. J. E., Roll, P. G., & Wilkinson, D. T. 1965, ApJ, 142, 414, doi: 10.1086/148306

Djorgovski, S., & Davis, M. 1987, ApJ, 313, 59, doi: 10.1086/164948

D'Odorico, S., Dekker, H., Mazzoleni, R., et al. 2006, in Proc. SPIE, Vol. 6269, Society of Photo-Optical Instrumentation Engineers (SPIE) Conference Series, 626933

D'Onofrio, M., Fasano, G., Moretti, A., et al. 2013, MNRAS, 435, 45, doi: 10.1093/mnras/stt1278

Dressler, A. 1980, ApJ, 236, 351, doi: 10.1086/157753

Dressler, A., Lynden-Bell, D., Burstein, D., et al. 1987, ApJ, 313, 42, doi: 10.1086/164947

Dubois, Y., Gavazzi, R., Peirani, S., & Silk, J. 2013, MNRAS, 433, 3297, doi: 10.1093/mnras/stt997

Ebeling, H., Stockmann, M., Richard, J., et al. 2018, ApJ, 852, L7, doi: 10.3847/2041-8213/aa9fee

Einstein, A. 1916, Annalen der Physik, 354, 769, doi: 10.1002/andp.19163540702

Elbaz, D., Daddi, E., Le Borgne, D., et al. 2007, A&A, 468, 33, doi: 10.1051/0004-6361:20077525

Faber, S. M., Dressler, A., Davies, R. L., et al. 1987, in Nearly Normal Galaxies. From the Planck Time to the Present, ed. S. M. Faber, 175

Faber, S. M., & Jackson, R. E. 1976, ApJ, 204, 668, doi: 10.1086/154215

Fagioli, M., Carollo, C. M., Renzini, A., et al. 2016, ApJ, 831, 173, doi: 10.3847/0004-637X/831/2/173

Faisst, A. L., Carollo, C. M., Capak, P. L., et al. 2017, ApJ, 839, 71, doi: 10.3847/1538-4357/aa697a

Falcón-Barroso, J., Sánchez-Blázquez, P., Vazdekis, A., et al. 2011, A&A, 532, A95, doi: 10.1051/0004-6361/201116842

Fan, L., Lapi, A., Bressan, A., et al. 2010, ApJ, 718, 1460, doi: 10.1088/0004-637X/718/2/1460

Fan, L., Lapi, A., De Zotti, G., & Danese, L. 2008, ApJ, 689, L101, doi: 10.1086/595784

Ferré-Mateu, A., Vazdekis, A., Trujillo, I., et al. 2012, MNRAS, 423, 632, doi: 10.1111/j.1365-2966.2012.20897.x

Franx, M., van Dokkum, P. G., Förster Schreiber, N. M., et al. 2008, ApJ, 688, 770, doi: 10.1086/592431

Franx, M., Moorwood, A., Rix, H. W., et al. 2000, The Messenger, 99, 20

Franx, M., Labbé, I., Rudnick, G., et al. 2003, ApJ, 587, L79, doi: 10.1086/375155

Friedmann, A. 1922, Zeitschrift fur Physik, 10, 377, doi: 10.1007/BF01332580

Frigo, M., & Balcells, M. 2017, MNRAS, 469, 2184, doi: 10.1093/mnras/stx875

Fukugita, M., Ichikawa, T., Gunn, J. E., et al. 1996, AJ, 111, 1748, doi: 10.1086/117915

Fumagalli, M., Labbé, I., Patel, S. G., et al. 2014, ApJ, 796, 35, doi: 10.1088/0004-637X/796/1/35

Gabor, J. M., & Davé, R. 2012, MNRAS, 427, 1816, doi: 10.1111/j.1365-2966.2012.21640.x

Gallazzi, A., Charlot, S., Brinchmann, J., White, S. D. M., & Tremonti, C. A. 2005, MNRAS, 362, 41, doi: 10.1111/j.1365-2966.2005.09321.x

Gamow, G., & Teller, E. 1939, Physical Review, 55, 654, doi: 10.1103/PhysRev.55.654

Genel, S., Vogelsberger, M., Springel, V., et al. 2014, MNRAS, 445, 175, doi: 10.1093/mnras/stu1654

Glazebrook, K., Schreiber, C., Labbé, I., et al. 2017, Nature, 544, 71, doi: 10.1038/nature21680

Gobat, R., Daddi, E., Magdis, G., et al. 2018, Nature Astronomy, 2, 239, doi: 10.1038/s41550-017-0352-5

Godwin, J. G., Metcalfe, N., & Peach, J. V. 1983, MNRAS, 202, 113, doi: 10.1093/mnras/202.1.113

Gómez-Guijarro, C., Toft, S., Karim, A., et al. 2018, ApJ, 856, 121, doi: 10.3847/1538-4357/aab206

Graves, G. J., Faber, S. M., & Schiavon, R. P. 2009, ApJ, 698, 1590, doi: 10.1088/0004-637X/698/2/1590

Greene, J. E., Janish, R., Ma, C.-P., et al. 2015, ApJ, 807, 11, doi: 10.1088/0004-637X/807/1/11

Guth, A. H. 1981, Phys. Rev. D, 23, 347, doi: 10.1103/PhysRevD.23.347

Guth, A. H., & Pi, S.-Y. 1982, Physical Review Letters, 49, 1110, doi: 10.1103/PhysRevLett.49.1110

Habouzit, M., Genel, S., Somerville, R. S., et al. 2019, MNRAS, 484, 4413, doi: 10.1093/mnras/stz102

Hafez, I. 2010, PhD thesis, James Cook University

Hawking, S. W. 1982, Physics Letters B, 115, 295, doi: 10.1016/0370-2693(82)90373-2

Herschel, W. 1789, Philosophical Transactions of the Royal Society of London Series I, 79, 212

Hill, A. R., Muzzin, A., Franx, M., et al. 2017, ApJ, 837, 147, doi: 10.3847/1538-4357/aa61fe

Hilz, M., Naab, T., & Ostriker, J. P. 2013, MNRAS, 429, 2924, doi: 10.1093/mnras/sts501

Hilz, M., Naab, T., Ostriker, J. P., et al. 2012, MNRAS, 425, 3119, doi: 10.1111/j.1365-2966.2012.21541.x

Hirschmann, M., Naab, T., Somerville, R. S., Burkert, A., & Oser, L. 2012, MNRAS, 419, 3200, doi: 10.1111/j.1365-2966.2011.19961.x

Hirschmann, M., Naab, T., Davé, R., et al. 2013, MNRAS, 436, 2929, doi: 10.1093/mnras/stt1770

Hopkins, P. F., Bundy, K., Murray, N., et al. 2009, MNRAS, 398, 898, doi: 10.1111/j.1365-2966.2009.15062.x

Hopkins, P. F., Richards, G. T., & Hernquist, L. 2007, ApJ, 654, 731, doi: 10.1086/509629

Horne, K. 1986, PASP, 98, 609, doi: 10.1086/131801

Hubble, E. 1929, Proceedings of the National Academy of Science, 15, 168, doi: 10.1073/pnas.15.3.168

Hubble, E. P. 1926, ApJ, 64, doi: 10.1086/143018

Husser, T.-O., Wende-von Berg, S., Dreizler, S., et al. 2013, A&A, 553, A6, doi: 10.1051/0004-6361/201219058

Ilbert, O., Capak, P., Salvato, M., et al. 2009, ApJ, 690, 1236, doi: 10.1088/0004-637X/690/2/1236

Jeans, J. H. 1902, Philosophical Transactions of the Royal Society of London Series A, 199, 1, doi: 10.1098/rsta.1902.0012

Jin, S., Daddi, E., Liu, D., et al. 2018, ApJ, 864, 56, doi: 10.3847/1538-4357/aad4af

Jørgensen, I. 1999, MNRAS, 306, 607, doi: 10.1046/j.1365-8711.1999.02555.x

Jørgensen, I., & Chiboucas, K. 2013, AJ, 145, 77, doi: 10.1088/0004-6256/145/3/77

Jørgensen, I., Chiboucas, K., Berkson, E., et al. 2017, AJ, 154, 251, doi: 10.3847/1538-3881/aa96a3

Jørgensen, I., Chiboucas, K., Flint, K., et al. 2006, ApJ, 639, L9, doi: 10.1086/501348

Jørgensen, I., Chiboucas, K., Webb, K., & Woodrum, C. 2018, AJ, 156, 224, doi: 10.3847/1538-3881/aae522

Jørgensen, I., Franx, M., & Kjaergaard, P. 1996, MNRAS, 280, 167, doi: 10.1093/mnras/280.1.167

Jørgensen, I., Hunter, L. C., O'Neill, C. R., et al. 2019, arXiv e-prints, arXiv:1907.00121. https://arxiv.org/abs/1907.00121

Kado-Fong, E., Marchesini, D., Marsan, Z. C., et al. 2017, ApJ, 838, 57, doi: 10.3847/1538-4357/aa6037

Kauffmann, G., Heckman, T. M., Tremonti, C., et al. 2003, MNRAS, 346, 1055, doi: 10.1111/j.1365-2966.2003.07154.x

Kennicutt, Jr., R. C. 1998, ARA&A, 36, 189, doi: 10.1146/annurev.astro.36.1.189

Kennicutt, Jr., R. C., Hao, C.-N., Calzetti, D., et al. 2009, ApJ, 703, 1672, doi: 10.1088/0004-637X/703/2/1672

Khochfar, S., & Silk, J. 2006, ApJ, 648, L21, doi: 10.1086/507768

Koekemoer, A. M., Aussel, H., Calzetti, D., et al. 2007, ApJS, 172, 196, doi: 10.1086/520086

Kriek, M., van der Wel, A., van Dokkum, P. G., Franx, M., & Illingworth, G. D. 2008, ApJ, 682, 896, doi: 10.1086/589677

Kriek, M., van Dokkum, P. G., Franx, M., Illingworth, G. D., & Magee, D. K. 2009a, ApJ, 705, L71, doi: 10.1088/0004-637X/705/1/L71

Kriek, M., van Dokkum, P. G., Labbé, I., et al. 2009b, ApJ, 700, 221, doi: 10.1088/0004-637X/700/1/221

Kriek, M., van Dokkum, P. G., Franx, M., et al. 2006a, ApJ, 645, 44, doi: 10.1086/504103

—. 2006b, ApJ, 649, L71, doi: 10.1086/508371

Kriek, M., Conroy, C., van Dokkum, P. G., et al. 2016, Nature, 540, 248, doi: 10.1038/nature20570

Krogager, J.-K., Zirm, A. W., Toft, S., Man, A., & Brammer, G. 2014, ApJ, 797, 17, doi: 10.1088/0004-637X/797/1/17

Kubo, M., Tanaka, M., Yabe, K., et al. 2018, ApJ, 867, 1, doi: 10.3847/1538-4357/aae3e8

Labbé, I., Huang, J., Franx, M., et al. 2005, ApJ, 624, L81, doi: 10.1086/430700

Lackner, C. N., Cen, R., Ostriker, J. P., & Joung, M. R. 2012, MNRAS, 425, 641, doi: 10.1111/j.1365-2966.2012.21525.x

Lagos, C. d. P., Stevens, A. R. H., Bower, R. G., et al. 2018, MNRAS, 473, 4956, doi: 10.1093/mnras/stx2667

Laigle, C., McCracken, H. J., Ilbert, O., et al. 2016, ApJS, 224, 24, doi: 10.3847/0067-0049/224/2/24

Lani, C., Almaini, O., Hartley, W. G., et al. 2013, MNRAS, 435, 207, doi: 10.1093/mnras/stt1275

Le Floc'h, E., Aussel, H., Ilbert, O., et al. 2009, ApJ, 703, 222, doi: 10.1088/0004-637X/703/1/222

Leja, J., van Dokkum, P., & Franx, M. 2013, ApJ, 766, 33, doi: 10.1088/0004-637X/766/1/33

Lemaître, G. 1927, Annales de la Société Scientifique de Bruxelles, 47, 49

Lifshitz, E. M. 1946, Zhurnal Eksperimentalnoi i Teoreticheskoi Fiziki, 16, 587

Linde, A. D. 1982, Physics Letters B, 116, 335, doi: 10.1016/0370-2693(82)90293-3

Ma, C.-P., Greene, J. E., McConnell, N., et al. 2014, ApJ, 795, 158, doi: 10.1088/0004-637X/795/2/158

Madau, P., & Dickinson, M. 2014, ARA&A, 52, 415, doi: 10.1146/annurev-astro-081811-125615

Magdis, G. E., Daddi, E., Béthermin, M., et al. 2012, ApJ, 760, 6, doi: 10.1088/0004-637X/760/1/6

Man, A., & Belli, S. 2018, Nature Astronomy, 2, 695, doi: 10.1038/s41550-018-0558-1

Man, A. W. S., Toft, S., Zirm, A. W., Wuyts, S., & van der Wel, A. 2012, ApJ, 744, 85, doi: 10.1088/0004-637X/744/2/85

Man, A. W. S., Zirm, A. W., & Toft, S. 2016a, ApJ, 830, 89, doi: 10.3847/0004-637X/830/2/89

Man, A. W. S., Greve, T. R., Toft, S., et al. 2016b, ApJ, 820, 11, doi: 10.3847/0004-637X/820/1/11

Mancini, C., Daddi, E., Renzini, A., et al. 2010, MNRAS, 401, 933, doi: 10.1111/j.1365-2966.2009.15728.x

Maraston, C. 2005, MNRAS, 362, 799, doi: 10.1111/j.1365-2966.2005.09270.x

Marchesi, S., Civano, F., Elvis, M., et al. 2016, ApJ, 817, 34, doi: 10.3847/0004-637X/817/1/34

Marchesini, D., Muzzin, A., Stefanon, M., et al. 2014, ApJ, 794, 65, doi: 10.1088/0004-637X/794/1/65

Marsan, Z. C., Marchesini, D., Muzzin, A., et al. 2019, ApJ, 871, 201, doi: 10.3847/1538-4357/aaf808

Matharu, J., Muzzin, A., Brammer, G. B., et al. 2019, MNRAS, 484, 595, doi: 10.1093/mnras/sty3465

McCracken, H. J., Capak, P., Salvato, M., et al. 2010, ApJ, 708, 202, doi: 10.1088/0004-637X/708/1/202

McLure, R. J., Pearce, H. J., Dunlop, J. S., et al. 2013, MNRAS, 428, 1088, doi: 10.1093/mnras/sts092

Messier, C. 1781, Catalogue des Nébuleuses et des Amas d'Étoiles (Catalog of Nebulae and Star Clusters), Tech. rep.

Modigliani, A., Goldoni, P., Royer, F., et al. 2010, in Proc. SPIE, Vol. 7737, Observatory Operations: Strategies, Processes, and Systems III, 773728

Morishita, T., Abramson, L. E., Treu, T., et al. 2019, ApJ, 877, 141, doi: 10.3847/1538-4357/ab1d53

Mowla, L. A., van Dokkum, P., Brammer, G. B., et al. 2019, ApJ, 880, 57, doi: 10.3847/1538-4357/ab290a

Mundy, C. J., Conselice, C. J., & Ownsworth, J. R. 2015, MNRAS, 450, 3696, doi: 10.1093/mnras/stv860

Muzzin, A., Marchesini, D., Stefanon, M., et al. 2013a, ApJ, 777, 18, doi: 10.1088/0004-637X/777/1/18

—. 2013b, ApJ, 777, 18, doi: 10.1088/0004-637X/777/1/18

Naab, T. 2013, in IAU Symposium, Vol. 295, The Intriguing Life of Massive Galaxies, ed. D. Thomas, A. Pasquali, & I. Ferreras, 340–349

Naab, T., Johansson, P. H., & Ostriker, J. P. 2009, ApJ, 699, L178, doi: 10.1088/0004-637X/699/2/L178

Naab, T., Johansson, P. H., Ostriker, J. P., & Efstathiou, G. 2007, ApJ, 658, 710, doi: 10.1086/510841

Naab, T., Khochfar, S., & Burkert, A. 2006, ApJ, 636, L81, doi: 10.1086/500205

Naab, T., Oser, L., Emsellem, E., et al. 2014, MNRAS, 444, 3357, doi: 10.1093/mnras/stt1919

Nelson, D., Pillepich, A., Genel, S., et al. 2015, Astronomy and Computing, 13, 12, doi: 10.1016/j.ascom.2015.09.003

Newman, A. B., Belli, S., & Ellis, R. S. 2015, ApJ, 813, L7, doi: 10.1088/2041-8205/813/1/L7

Newman, A. B., Belli, S., Ellis, R. S., & Patel, S. G. 2018, ApJ, 862, 126, doi: 10.3847/1538-4357/aacd4f

Newman, A. B., Ellis, R. S., Andreon, S., et al. 2014, ApJ, 788, 51, doi: 10.1088/0004-637X/788/1/51

Newman, A. B., Ellis, R. S., Bundy, K., & Treu, T. 2012, ApJ, 746, 162, doi: 10.1088/0004-637X/746/2/162

Nipoti, C., Treu, T., Auger, M. W., & Bolton, A. S. 2009, ApJ, 706, L86, doi: 10.1088/0004-637X/706/1/L86

Noeske, K. G., Weiner, B. J., Faber, S. M., et al. 2007, ApJ, 660, L43, doi: 10.1086/517926

Oke, J. B., & Gunn, J. E. 1983, ApJ, 266, 713, doi: 10.1086/160817

Olsen, K. P., Rasmussen, J., Toft, S., & Zirm, A. W. 2013, ApJ, 764, 4, doi: 10.1088/0004-637X/764/1/4

Oogi, T., & Habe, A. 2013, MNRAS, 428, 641, doi: 10.1093/mnras/sts047

Oser, L., Naab, T., Ostriker, J. P., & Johansson, P. H. 2012, ApJ, 744, 63, doi: 10.1088/0004-637X/744/1/63

Oser, L., Ostriker, J. P., Naab, T., Johansson, P. H., & Burkert, A. 2010, ApJ, 725, 2312, doi: 10.1088/0004-637X/725/2/2312

Papovich, C., Dickinson, M., Giavalisco, M., Conselice, C. J., & Ferguson, H. C. 2005, ApJ, 631, 101, doi: 10.1086/429120

Peng, C. Y., Ho, L. C., Impey, C. D., & Rix, H.-W. 2002, AJ, 124, 266, doi: 10.1086/340952

Penzias, A. A., & Wilson, R. W. 1965, ApJ, 142, 419, doi: 10.1086/148307

Perlmutter, S., Aldering, G., Goldhaber, G., et al. 1999, ApJ, 517, 565, doi: 10.1086/307221

Planck Collaboration, Aghanim, N., Akrami, Y., et al. 2018, arXiv e-prints. https://arxiv.org/abs/1807.06209

Prichard, L. J., Davies, R. L., Beifiori, A., et al. 2017, ApJ, 850, 203, doi: 10.3847/1538-4357/aa96a6

Ragone-Figueroa, C., & Granato, G. L. 2011, MNRAS, 414, 3690, doi: 10.1111/j.1365-2966.2011.18670.x

Remus, R.-S., Dolag, K., Naab, T., et al. 2017, MNRAS, 464, 3742, doi: 10.1093/mnras/stw2594

Ricciardelli, E., Trujillo, I., Buitrago, F., & Conselice, C. J. 2010, MNRAS, 406, 230, doi: 10.1111/j.1365-2966.2010.16693.x

Rieke, G. H., Alonso-Herrero, A., Weiner, B. J., et al. 2009, ApJ, 692, 556, doi: 10.1088/0004-637X/692/1/556

Riess, A. G., Filippenko, A. V., Challis, P., et al. 1998, AJ, 116, 1009, doi: 10.1086/300499

Robitaille, T., & Bressert, E. 2012, APLpy: Astronomical Plotting Library in Python, Astrophysics Source Code Library. http://ascl.net/1208.017

Rodighiero, G., Daddi, E., Baronchelli, I., et al. 2011, ApJ, 739, L40, doi: 10.1088/2041-8205/739/2/L40

Rosse, E. O. 1844, Philosophical Transactions of the Royal Society of London Series I, 134, 321

Saglia, R. P., Sánchez-Blázquez, P., Bender, R., et al. 2010, A&A, 524, A6, doi: 10.1051/0004-6361/201014703

—. 2016, A&A, 596, C1, doi: 10.1051/0004-6361/201014703e

Salim, S., Dickinson, M., Michael Rich, R., et al. 2009, ApJ, 700, 161, doi: 10.1088/0004-637X/700/1/161

Sánchez-Blázquez, P., Peletier, R. F., Jiménez-Vicente, J., et al. 2006, MNRAS, 371, 703, doi: 10.1111/j.1365-2966.2006.10699.x

Sandage, A. 1986, A&A, 161, 89

Schawinski, K., Lintott, C. J., Thomas, D., et al. 2009, ApJ, 690, 1672, doi: 10.1088/0004-637X/690/2/1672

Schawinski, K., Urry, C. M., Simmons, B. D., et al. 2014, MNRAS, 440, 889, doi: 10.1093/mnras/stu327

Scholz, F. W., & Stephens, M. A. 1987, Journal of the American Statistical Association, 82, 918

Schreiber, C., Pannella, M., Elbaz, D., et al. 2015, A&A, 575, A74, doi: 10.1051/0004-6361/201425017

Schreiber, C., Glazebrook, K., Nanayakkara, T., et al. 2018, A&A, 618, A85, doi: 10.1051/0004-6361/201833070

Scoville, N., Abraham, R. G., Aussel, H., et al. 2007, ApJS, 172, 38, doi: 10.1086/516580

Selsing, J., Fynbo, J. P. U., Christensen, L., & Krogager, J.-K. 2016, A&A, 585, A87, doi: 10.1051/0004-6361/201527096

Sersic, J. L. 1968, Atlas de Galaxias Australes

Shen, S., Mo, H. J., White, S. D. M., et al. 2003, MNRAS, 343, 978, doi: 10.1046/j.1365-8711.2003.06740.x

Shih, H.-Y., & Stockton, A. 2011, ApJ, 733, 45, doi: 10.1088/0004-637X/733/1/45

Simpson, J. M., Smail, I., Wang, W.-H., et al. 2017, ApJ, 844, L10, doi: 10.3847/2041-8213/aa7cf2

Sparre, M. 2015, XSHPipelineManager: Wrapper for the VLT/X-shooter Data Reduction Pipeline, Astrophysics Source Code Library. http://ascl.net/1509.001

Speagle, J. S., Steinhardt, C. L., Capak, P. L., & Silverman, J. D. 2014, ApJS, 214, 15, doi: 10.1088/0067-0049/214/2/15

Springel, V., White, S. D. M., Jenkins, A., et al. 2005, Nature, 435, 629, doi: 10.1038/nature03597

Starobinsky, A. A. 1982, Physics Letters B, 117, 175, doi: 10.1016/0370-2693(82)90541-X

Stockmann, S., Toft, S., Gallazzi, A., et al. 2019, Submitted to ApJ

Straatman, C. M. S., Labbé, I., Spitler, L. R., et al. 2015, ApJ, 808, L29, doi: 10.1088/2041-8205/808/1/L29

Strazzullo, V., Gobat, R., Daddi, E., et al. 2013, ApJ, 772, 118, doi: 10.1088/0004-637X/772/2/118

Szomoru, D., Franx, M., Bouwens, R. J., et al. 2011, ApJ, 735, L22, doi: 10.1088/2041-8205/735/1/L22

Szomoru, D., Franx, M., & van Dokkum, P. G. 2012, ApJ, 749, 121, doi: 10.1088/0004-637X/749/2/121

Szomoru, D., Franx, M., van Dokkum, P. G., et al. 2010, ApJ, 714, L244, doi: 10.1088/2041-8205/714/2/L244

Tanaka, M., Kodama, T., Arimoto, N., et al. 2005, MNRAS, 362, 268, doi: 10.1111/j.1365-2966.2005.09300.x

Tapia, T., Eliche-Moral, M. C., Querejeta, M., et al. 2014, A&A, 565, A31, doi: 10.1051/0004-6361/201321386

Taylor, E. N., Franx, M., Brinchmann, J., van der Wel, A., & van Dokkum, P. G. 2010a, ApJ, 722, 1, doi: 10.1088/0004-637X/722/1/1

Taylor, E. N., Franx, M., Glazebrook, K., et al. 2010b, ApJ, 720, 723, doi: 10.1088/0004-637X/720/1/723

Thomas, D., Maraston, C., Bender, R., & Mendes de Oliveira, C. 2005, ApJ, 621, 673, doi: 10.1086/426932

Toft, S., Franx, M., van Dokkum, P., et al. 2009, ApJ, 705, 255, doi: 10.1088/0004-637X/705/1/255

Toft, S., Gallazzi, A., Zirm, A., et al. 2012, ApJ, 754, 3, doi: 10.1088/0004-637X/754/1/3

Toft, S., van Dokkum, P., Franx, M., et al. 2005, ApJ, 624, L9, doi: 10.1086/430346

—. 2007, ApJ, 671, 285, doi: 10.1086/521810

Toft, S., Smolčić, V., Magnelli, B., et al. 2014, ApJ, 782, 68, doi: 10.1088/0004-637X/782/2/68

Toft, S., Zabl, J., Richard, J., et al. 2017, Nature, 546, 510, doi: 10.1038/nature22388

Toomre, A., & Toomre, J. 1972, ApJ, 178, 623, doi: 10.1086/151823

Torrey, P., Wellons, S., Ma, C.-P., Hopkins, P. F., & Vogelsberger, M. 2017, MNRAS, 467, 4872, doi: 10.1093/mnras/stx370

Treu, T., Ellis, R. S., Liao, T. X., et al. 2005, ApJ, 633, 174, doi: 10.1086/444585

Trujillo, I., Cenarro, A. J., de Lorenzo-Cáceres, A., et al. 2009, ApJ, 692, L118, doi: 10.1088/0004-637X/692/2/L118

Trujillo, I., Conselice, C. J., Bundy, K., et al. 2007, MNRAS, 382, 109, doi: 10.1111/j.1365-2966.2007.12388.x

Trujillo, I., Förster Schreiber, N. M., Rudnick, G., et al. 2006, ApJ, 650, 18, doi: 10.1086/506464

Utomo, D., Kriek, M., Labbé, I., Conroy, C., & Fumagalli, M. 2014, ApJ, 783, L30, doi: 10.1088/2041-8205/783/2/L30

van de Sande, J., Kriek, M., Franx, M., Bezanson, R., & van Dokkum, P. G. 2014, ApJ, 793, L31, doi: 10.1088/2041-8205/793/2/L31

van de Sande, J., Kriek, M., Franx, M., et al. 2013, ApJ, 771, 85, doi: 10.1088/0004-637X/771/2/85

van de Sande, J., Lagos, C. D. P., Welker, C., et al. 2019, MNRAS, 484, 869, doi: 10.1093/mnras/sty3506

van der Marel, R. P., & van Dokkum, P. G. 2007, ApJ, 668, 756, doi: 10.1086/521211

van der Wel, A., Bell, E. F., van den Bosch, F. C., Gallazzi, A., & Rix, H.-W. 2009, ApJ, 698, 1232, doi: 10.1088/0004-637X/698/2/1232

van der Wel, A., Franx, M., van Dokkum, P. G., et al. 2005, ApJ, 631, 145, doi: 10.1086/430464

van der Wel, A., Holden, B. P., Zirm, A. W., et al. 2008, ApJ, 688, 48, doi: 10.1086/592267

van der Wel, A., Rix, H.-W., Wuyts, S., et al. 2011, ApJ, 730, 38, doi: 10.1088/0004-637X/730/1/38

van der Wel, A., Franx, M., van Dokkum, P. G., et al. 2014, ApJ, 788, 28, doi: 10.1088/0004-637X/788/1/28

van Dokkum, P. G., & Franx, M. 1996, MNRAS, 281, 985, doi: 10.1093/mnras/281.3.985

van Dokkum, P. G., Kriek, M., & Franx, M. 2009, Nature, 460, 717, doi: 10.1038/nature08220

van Dokkum, P. G., Quadri, R., Marchesini, D., et al. 2006, ApJ, 638, L59, doi: 10.1086/501045

van Dokkum, P. G., Franx, M., Kriek, M., et al. 2008, ApJ, 677, L5, doi: 10.1086/587874

van Dokkum, P. G., Whitaker, K. E., Brammer, G., et al. 2010, ApJ, 709, 1018, doi: 10.1088/0004-637X/709/2/1018

Veale, M., Ma, C.-P., Greene, J. E., et al. 2018, MNRAS, 473, 5446, doi: 10.1093/mnras/stx2717

Vernet, J., Dekker, H., D'Odorico, S., et al. 2011, A&A, 536, A105, doi: 10.1051/0004-6361/201117752

Wellons, S., & Torrey, P. 2017, MNRAS, 467, 3887, doi: 10.1093/mnras/stx358

Wellons, S., Torrey, P., Ma, C.-P., et al. 2015, MNRAS, 449, 361, doi: 10.1093/mnras/stv303

Whitaker, K. E., van Dokkum, P. G., Brammer, G., & Franx, M. 2012, ApJ, 754, L29, doi: 10.1088/2041-8205/754/2/L29

Whitaker, K. E., Labbé, I., van Dokkum, P. G., et al. 2011, ApJ, 735, 86, doi: 10.1088/0004-637X/735/2/86

Whitaker, K. E., Bezanson, R., van Dokkum, P. G., et al. 2017, ApJ, 838, 19, doi: 10.3847/1538-4357/aa6258

White, S. D. M., & Rees, M. J. 1978, MNRAS, 183, 341, doi: 10.1093/mnras/183.3.341

Williams, R. J., Quadri, R. F., Franx, M., van Dokkum, P., & Labbé, I. 2009, ApJ, 691, 1879, doi: 10.1088/0004-637X/691/2/1879

Williams, R. J., Quadri, R. F., Franx, M., et al. 2010, ApJ, 713, 738, doi: 10.1088/0004-637X/713/2/738

Wu, H., Cao, C., Hao, C.-N., et al. 2005, ApJ, 632, L79, doi: 10.1086/497961

Wuyts, S., Labbé, I., Franx, M., et al. 2007, ApJ, 655, 51, doi: 10.1086/509708

Wuyts, S., Förster Schreiber, N. M., van der Wel, A., et al. 2011, ApJ, 742, 96, doi: 10.1088/0004-637X/742/2/96

York, D. G., Adelman, J., Anderson, John E., J., et al. 2000, AJ, 120, 1579, doi: 10.1086/301513

Zabl, J., Nørgaard-Nielsen, H. U., Fynbo, J. P. U., et al. 2015, MNRAS, 451, 2050, doi: 10.1093/mnras/stv1019

Zahid, H. J., Geller, M. J., Damjanov, I., & Sohn, J. 2019, ApJ, 878, 158, doi: 10.3847/1538-4357/ab21b9

Zamojski, M. A., Schiminovich, D., Rich, R. M., et al. 2007, ApJS, 172, 468, doi: 10.1086/516593

Zhu, Y.-N., Wu, H., Cao, C., & Li, H.-N. 2008, ApJ, 686, 155, doi: 10.1086/591121

Zibetti, S., Gallazzi, A. R., Hirschmann, M., et al. 2019, arXiv e-prints, arXiv:1906.02209. https://arxiv.org/abs/1906.02209

Zibetti, S., Gallazzi, A. R., Ascasibar, Y., et al. 2017, MNRAS, 468, 1902, doi: 10.1093/mnras/stx251

Zirm, A. W., van der Wel, A., Franx, M., et al. 2007, ApJ, 656, 66, doi: 10.1086/510713

Zwicky, F. 1933, Helvetica Physica Acta, 6, 110